



Modelling and parameter identification for energy beam footprints

Kateryna Bashtova

► To cite this version:

Kateryna Bashtova. Modelling and parameter identification for energy beam footprints. Other. Université Côte d'Azur, 2016. English. NNT : 2016AZUR4112 . tel-01485913

HAL Id: tel-01485913

<https://theses.hal.science/tel-01485913>

Submitted on 9 Mar 2017

HAL is a multi-disciplinary open access archive for the deposit and dissemination of scientific research documents, whether they are published or not. The documents may come from teaching and research institutions in France or abroad, or from public or private research centers.

L'archive ouverte pluridisciplinaire **HAL**, est destinée au dépôt et à la diffusion de documents scientifiques de niveau recherche, publiés ou non, émanant des établissements d'enseignement et de recherche français ou étrangers, des laboratoires publics ou privés.

Université Nice Sophia Antipolis - UFR Sciences
École Doctorale de Sciences Fondamentales et Appliquées

Thèse

pour obtenir le titre de
Docteur en Sciences
de l'Université Nice Sophia Antipolis

Discipline : Mathématiques

présentée et soutenue par
Kateryna BASHTOVA

Modélisation et identification de paramètres
pour les empreintes des faisceaux de haute énergie

Modelling and parameter identification for energy beam footprints

Thèse dirigée par **Didier AUROUX**

soutenue le 5 décembre 2016

Jury:

M. Mark ASCH	<i>Rapporteur</i>	Professeur des Universités
M. Didier AUROUX	<i>Directeur de thèse</i>	Professeur des Universités
M. Patrick DE CAUSMAECKER	<i>Rapporteur</i>	Professeur des Universités
M. Mohamed MASMOUDI	<i>Examinateur</i>	Professeur des Universités
M. Oliver PANTZ	<i>Examinateur</i>	Professeur des Universités
M. Mathias ROMMEL	<i>Examinateur</i>	Docteur-Ingénieur

Abstract. The technological progress demands more and more sophisticated and precise techniques of the treatment of materials. We study the machining of the material with the high energy beams: the abrasive waterjet, the focused ion beam and the laser. Although the physics governing the energy beam interaction with material is very different for different application, we can use the same approach to the mathematical modeling of these processes.

The evolution of the material surface under the energy beam impact is modeled by PDE equation. This equation contains a set of unknown parameters - the calibration parameters of the model. The unknown parameters can be identified by minimization of the cost function, i.e., function that describes the difference between the result of modeling and the corresponding experimental data. As the modeled surface is a solution of the PDE problem, this minimization is an example of PDE-constrained optimization problem. The identification problem was regularized using Tikhonov regularization. The gradient of the cost function was obtained both by using the variational approach and by means of the automatic differentiation. Once the cost function and its gradient calculated, the minimization was performed using L-BFGS minimizer.

For the abrasive waterjet application the problem of non-uniqueness of numerical solution is solved. The impact of the secondary effects non included into the model is avoided as well. The calibration procedure is validated on both synthetic and experimental data.

For the laser application, we presented a simple criterion that allows to distinguish between the thermal and non-thermal laser ablation regimes.

Key words: PDE constrained optimization; parameters calibration; variational approach; continuous adjoint problem; discrete adjoint problem; automatic differentiation; TAPENADE A.D. engine; Tikhonov regularization; L-curve; abrasive waterjet; focused ion beam; laser ablation.

Résumé. Le progrès technologique nécessite des techniques de plus en plus sophistiquées et précises de traitement de matériaux. Nous étudions le traitement de matériaux par faisceaux de haute énergie : un jet d'eau abrasif, une sonde ionique focalisée, un laser. Bien que la physique régissant l'interaction entre des faisceaux de haute énergie et un matériau varie grandement d'une application à une autre, on peut utiliser la même approche mathématique pour modéliser ces processus.

L'évolution de la surface du matériau sous l'action du faisceau de haute énergie est modélisée par une EDP. Cette équation contient l'ensemble des coefficients inconnus - les paramètres de calibration de modèle. Les paramètres inconnus peuvent être calibrés par minimisation de la fonction coût, c'est-à-dire, la fonction qui décrit la différence entre le résultat de la modélisation et les données expérimentales. Comme la surface modélisée est une solution du problème d'EDP, cela rentre dans le cadre de l'optimisation sous contrainte d'EDP. L'identification a été rendue bien posée par la régularisation du type Tikhonov. Le gradient de la fonction coût a été obtenu en utilisant les deux méthodes : l'approche adjointe et la différentiation automatique. Une fois la fonction coût et son gradient obtenus, nous avons utilisé un minimiseur L-BFGS pour réaliser la minimisation.

Le problème de la non-unicité de la solution a été résolu pour le problème de traitement par le jet d'eau abrasif. Des effets secondaires ne sont pas inclus dans le modèle. Leur impact sur le procédé de calibration a été évité. Ensuite, le procédé de calibration a été validé pour les données synthétiques et expérimentales. Enfin, nous avons proposé un critère pour distinguer facilement entre le régime thermique et non-thermique d'ablation par laser.



This work was performed within the EU Marie Curie
Initial Training Network STEEP (Grant no. 316560).

This thesis was prepared in the Laboratory J.A. Dieudonné
of the University of Nice Sophia Antipolis



Remerciements

C'est avec plaisir et reconnaissance que je profite de ces quelques lignes pour remercier les nombreuses personnes qui ont contribué, de différentes manières, à la réalisation de cette thèse.

Tout d'abord, je tiens à remercier mon directeur de thèse, Didier Auroux. Merci pour la confiance que vous m'avez toujours accordée, pour votre soutien et vos conseils tout au long de ces trois années.

I would like to thank my reading committee members, Mark Asch and Patrick De Causmaecker, and the members of my oral defense, Mohamed Masmoudi, Oliver Pantz, Mathias Rommel for their time, interest and helpful comments. I am honored to have you in my thesis committee.

This thesis has benefited from fruitful collaboration within the STEEP. I am happy to have been part of the project. I am especially grateful for the support that I've received during my secondments. A very big and special thanks go to all PhD of STEEP, I can only hope to work in such a team again.

I do not have enough words to express my gratitude to Victor Zadorozhnii and Nataliya Mayko, who guided me into research and who have always been an inspiration for me and continue to be so.

Je suis reconnaissante à Erwan Aubry, Stefane Descombe et Nicole Simson qui ont guidé mes premiers pas dans l'enseignement.

Merci aussi à toute l'équipe administrative du LJAD.

Je remercie ma professeur de français, Maurice De Micheli, pour ses cours géniaux.

Merci aux doctorants du LJAD pour les bons moments passés en votre compagnie, aux cinéphiles, aux pâtissiers, aux randonneurs, aux adeptes de jeux de société, aux mélomanes, aux grands bosseurs et aux stylés. J'ai une pensée toute particulière et chaleureuse pour mes profs de vélo et pour les participantes aux soirées de filles.

Особливі спасибі моїм батькам за вашу люблячу підтримку і дві половини, що однаково напрацювали на цей стосик!

Merci à Maksym pour m'avoir épaulée sur le chemin (parfois schisteux) durant ces années. Дякую тобі, за те, що ти завжди зі мною...

We become what we behold.

We shape our tools

and then our tools shape us.

Marshall McLuhan

Contents

Introduction (English)	7
Introduction (Français)	11
1 Tools. Introduction to optimization with PDE constraints	15
1.1 Numerical minimization of a function	15
1.2 Adjoint approach to optimization with PDE constraints	21
1.2.1 Variational formulation	21
1.2.2 A Lagrangian formulation	22
1.3 Automatic differentiation approach	26
1.3.1 Different modes of the Automatic Differentiation	27
1.3.2 Automatic Differentiation Engine TAPENADE	32
2 Abrasive Waterjet Machining	37
2.1 Origins of the geometrical model	38
2.2 General approach to the calibration problem	41
3 Stationary Abrasive Waterjet	45
3.1 Application of the continuous adjoint approach	47
3.2 Application of the discrete adjoint approach	50
3.2.1 Derivation of the adjoint problem	50
3.2.2 Calibration of the etching rate function	56
4 Moving Abrasive Waterjet	59
4.1 Geometrical model for moving abrasive waterjet	60
4.2 Moving abrasive waterjet. Adjoint approach	62
4.3 Moving abrasive waterjet: parameters calibration	67
5 Focus Ion Beam milling	77
5.1 Introduction to the FIB milling technique	77
5.2 Crater sputtering	79
5.3 Trench sputtering	84

6	Laser ablation	91
6.1	Introduction	91
6.2	Motivation for the introduction of the criterion	93
6.3	Experimental study of the ablated crater	97
	Conclusions and Perspectives (English)	99
	Conclusions et Perspectives (Français)	103
	Développement (Français)	107
	Bibliography	115

Introduction (English)

The technological progress demands more and more sophisticated and precise techniques of the treatment of materials. In present work we study the machining of the material with the energy beams (EB). We consider the following energy beam: the abrasive waterjet (AWJ), the focused ion beam (FIB) and the laser. In all applications, the EB brings to the target material enough energy to cause its local erosion in the spot of impact. The main challenge consists in prediction and control of the created shape. Although the physics governing the energy beam interaction with material is very different for different application, we can use the same approach to the mathematical modeling of these processes.

We consider a surface treated by the energy beam. This surface is described by a function $Z(\vec{r}, t)$. Z depends on a space coordinate \vec{r} and time t . We assume that the evolution of the target surface is described by an empirically introduced model in a form of a PDE:

$$F(u, Z) = 0. \quad (1)$$

This model (1) contains a set of unknown parameters $\{u\}$ - the calibration parameters of the model. They can be scalars or functions. These parameters cannot be measured directly from the experiments or they are hard and costly to measure.

When the parameters $\{u\}$ are known, the output of any given experimental setup can be predicted by solving (1). We call (1) the direct problem. The inverse problem consists in finding $\{u\}$ from the geometry of the treated surface $Z(\vec{r}, T)$ at the final time of treatment $t = T$.

Any chosen values of $\{u\}$ determine the output of the direct problem. The idea is to compare this output $Z(\vec{r}, T)$ with the measured in experiment surface Z_{exp} , a footprint of the energy beam. A probability to guess $\{u\}$ so that the experiment is described by the model perfectly is negligible. We introduce a cost function J :

$$J(u) = \|Z(\vec{r}, T) - Z_{exp}\|^2. \quad (2)$$

This function describes a discrepancy between the experimental data and the output of the solution of the direct problem for a given choice of $\{u\}$. The inverse problem consists in finding $\{u^*\}$ that minimizes the cost function, that is in solving the following PDE constrained problem:

Problem. *Find the set of parameters $\{u^*\}$ such that*

$$J(u^*) = \inf_u J(u),$$

under the constraint that Z is the output of the model (1) with the input $\{u\}$.

When this optimization problem is ill-posed, it is necessary to add a Tikhonov regularization term ([Tikhonov and Arsenin, 1977]) in the cost function (2). Moreover, (2) represents the most straightforward form of the cost function, and it should be further modified for some cases (see Chapter 4, Section 5.3). The main challenge of this optimization problem comes from the fact that some of the calibration parameters are functions. This case leads to the optimization in the infinite dimensional space.

This manuscript is organized as follows.

Chapter 1 gives a brief overview of the approaches to the solution of the PDE constrained optimization problem. At first we remind the quasi-Newton methods for the minimization of the function. Then we consider the adjoint approach to the PDE constrained optimization problem (Section 1.2). The direct PDE problem can be solved only numerically, as a consequence, the cost function is represented as an output of the computer program. This program takes the numerical values of the calibration parameters of the problem as its inputs. Section 1.3 explains the automatic differentiation (AD) approach to the differentiation of a function represented by a computer program. Then a brief overview of the AD software TAPENADE ([Hascoet and Pascual, 2013]) is considered.

Chapter 3 considers the milling of a crater by the abrasive waterjet. An example of application of the adjoint approach to the calibration of the etching rate function is given.

Chapter 4 studies the milling of a trench by the abrasive waterjet. We present the application of the adjoint approach and the automatic differentiation approach to the calibration of the geometrical AWJ model. The developed calibration procedure is applied to the real experimental data. Further, the obtained values of parameters are validated.

In Chapter 5, the developed approach is applied to the parameters identification for Focused Ion Beam milling technique. Ion intensity distribution was considered as a calibration parameter of the direct PDE model. We considered two cases of sputtering: sputtering of a crater (Section 5.2) and sputtering of a trench (Section 5.3). For both cases we developed a calibration procedure based on the automatic differentiation approach. This procedure was validated for the numerically generated experimental data.

Chapter 6 considers a crater created by the laser ablation. The involved physical processes are very complex. This complicates the choice of the direct model

in form (1). We suggested a very simple for experimental application criterion to distinguish between thermal and non-thermal regimes of laser ablation.

Introduction (Français)

Le progrès technologique nécessite des techniques de plus en plus sophistiquées et précises de traitement de matériaux. Dans cette thèse nous étudions le traitement de matériaux par faisceaux de haute énergie. Nous considérons les faisceaux de haute énergie suivants : un jet d'eau abrasif, une sonde ionique focalisée, un laser. Dans toutes les applications, le faisceau de haute énergie apporte au matériau cible assez d'énergie pour causer son érosion locale dans le point d'impact. Le défi principal consiste à prédire et contrôler la forme de la surface obtenue. Bien que la physique régissant l'interaction entre des faisceaux de haute énergie et un matériau varie grandement d'une application à une autre, on peut utiliser la même approche mathématique pour modéliser ces processus.

Nous considérons une surface traitée par le faisceau de haute énergie. Cette surface est décrite par une fonction $Z(\vec{r}, t)$. Nous supposons que l'évolution de la surface du matériau sous l'action du faisceau de haute énergie est modélisée par une EDP :

$$F(u, Z) = 0. \quad (3)$$

Cette équation (1) contient l'ensemble des coefficients inconnus $\{u\}$ - les paramètres de calibration de modèle. Ils peuvent être des scalaires ou des fonctions. Il n'est pas possible de mesurer ces paramètres directement de l'expérience ou ils sont très difficiles et coûteux à mesurer. Quand les paramètres $\{u\}$ sont connus, on peut prédire le résultat de l'expérience donnée en résolvant (1). (1) s'appelle le problème direct. Le problème inverse consiste à trouver $\{u\}$ à partir de la géométrie de la surface cible $Z(\vec{r}, T)$ au moment final du traitement $t = T$. Les valeurs de paramètres $\{u\}$ déterminent la solution du problème direct. L'idée consiste à comparer ce résultat $Z(\vec{r}, T)$ avec la surface Z_{exp} mesurée expérimentalement - une empreinte de faisceau. Nous introduisons la fonction coût J de la manière suivante :

$$J(u) = \|Z(\vec{r}, T) - Z_{exp}\|^2. \quad (4)$$

Cette fonction décrit la différence entre les données expérimentales et la solution du problème direct avec le choix donné de paramètres $\{u\}$. Le problème inverse consiste à trouver $\{u^*\}$ minimisant la fonction coût, c'est-à-dire résoudre le problème d'optimisation sous contrainte d'EDP suivant :

Problème. Trouver l'ensemble des paramètres $\{u^*\}$ tel que

$$J(u^*) = \inf_u J(u),$$

sous la contrainte que Z soit la solution du modèle direct (1) avec le choix de paramètres $\{u\}$.

Il est nécessaire d'ajouter un terme de régularisation de Tikhonov ([Tikhonov and Arsenin, 1977]) dans la fonction coût (2), quand ce problème d'optimisation est mal posé. De plus, (2) donne la forme la plus simple de la fonction coût, et cette expression doit être modifiée dans certains cas (voir Chapitre 4, Section 5.3). Le défi principal de ce problème d'optimisation vient du fait que certains paramètres sont des fonctions. Cela conduit à l'optimisation dans un espace de dimension infinie.

Ce manuscrit est organisé de la façon suivante.

Le chapitre 1 donne un bref aperçu des approches pour la résolution du problème d'optimisation sous contrainte d'EDP. D'abord, nous rappelons les méthodes de type quasi Newton pour la minimisation de la fonction. Ensuite, la section 1.2 est dédiée à l'approche adjointe pour la résolution du problème d'optimisation sous contrainte d'EDP. Le problème direct peut être résolu seulement numériquement. En conséquence, la fonction coût est représentée comme le résultat du programme informatique. Ce programme reçoit comme des données d'entrée les valeurs des paramètres de calibration. La section 1.3 explique l'application de différenciation automatique (DA) pour la différenciation de fonction représentée par un programme informatique. Ensuite, le bref aperçu du logiciel TAPENADE ([Hascoet and Pascual, 2013]) est donné.

Le chapitre 3 étudie le processus d'usinage de matériau par le jet d'eau abrasif. La surface traitée représente un cratère. Un exemple d'application de l'approche adjointe à la calibration de la fonction de la vitesse de gravure est donné.

Le chapitre 4 étudie le processus de fabrication d'une rainure par le jet d'eau abrasif. Le modèle est calibré en utilisant les deux méthodes : l'approche adjointe et la différenciation automatique. Le procédé de calibration est appliqué à la calibration des données expérimentales. Ensuite, les paramètres calibrés sont validés.

Dans le chapitre 5, l'approche de calibration est appliquée à l'identification des paramètres pour la technique d'usinage par une sonde ionique focalisée. Nous avons considéré la distribution d'énergie comme un paramètre de calibration. Deux expériences sont illustrées : la fabrication d'un cratère et d'une rainure. Pour ces deux cas le procédé de calibration est développé en utilisant la différenciation automatique. Ce procédé est validé pour les données expérimentales obtenues comme la solution numérique du problème direct.

Le chapitre 6 est dédié à l'étude d'ablation par laser. La surface traitée représente un cratère. Les processus impliqués dans l'évolution d'empreinte sont

très compliqués. Cela complique le choix du problème direct sous la forme (1). Nous avons suggéré un critère pour distinguer entre le régime thermique et non-thermique d’ablation. Ce critère est très simple pour l’application expérimentale.

Chapter 1

Tools. Introduction to optimization with PDE constraints

1.1 Numerical minimization of a function

Let $J: \mathbb{R}^n \rightarrow \mathbb{R}$ be a continuous and differentiable function. In this section we consider a problem of numerical minimization of J :

Problem. Find $u^* \in \mathbb{R}^n$ such that

$$J(u^*) = \min_u J(u).$$

Newton's Method

In the case of Newton's method, the consecutive iteration u_{k+1} minimize a quadratic approximation (1.1) of J in the neighborhood of the iteration point u_k .

$$J(u) \approx J(u_k) + (u - u_k)^T \nabla J(u) + \frac{1}{2}(u - u_k)^T (\nabla^2 J(u_k)) (u - u_k) \quad (1.1)$$

Here $\nabla^2 J(u_k) = H_k$ a Hessian of J in the point u_k . Minimization of $J(u)$ in (1.1) leads to the following choice of the descend direction $d_k = u_{k+1} - u_k$:

$$d_k = -H_k^{-1} \nabla J(u_k).$$

In practice d_k is found by solving the linear system $H_k d_k = -\nabla J(u_k)$ instead of using the former formula. This allows to avoid the costly inversion of the hessian H_k .

The robustness of the Newton's method can be increased by performing an additional line search along the descend direction d_k , the resulting algorithm is sometimes called the dump Newton's method. The update of the u_k is still searched

in the direction of d_k , but length of the step is modified: $u_{k+1} = u_k + \rho_k d_k$. A scalar steplength parameter ρ_k satisfies the Wolfe conditions ([Nocedal and Wright, 2006], [Wolfe, 1969]):

$$J(u_k + \rho_k d_k) \leq J(u_k) + \alpha \rho_k d_k^T \nabla J(u_k)$$

and

$$|d_k^T \nabla J(u_k + \rho_k d_k)| \leq \beta |d_k^T \nabla J(u_k)|$$

with $0 < \alpha < \beta < 1$.

In sum, the algorithm takes the form:

1. Initialization: choose a point u_0 - an initial guess.
2. Iterations: compute u_{k+1}
Check the stopping criterion
 - If the stopping criterion is satisfied: terminate optimization with the solution $u^* = u_k$.
 - If not:
 - Calculate the descent direction: d_k
 - Perform the linear search: ρ_k
 - Update the iteration point: $u_{k+1} = u_k + \rho_k d_k$
 - Go to the step 2.

Quasi-Newton methods

The Newton's method requires a computation of the Hessian matrix on each step of the optimization procedure. This operation is very costly numerically. In Quasi-Newton method the inverse hessian on the k iteration H_k^{-1} is substituted by its approximation B_k , which can be obtained in relatively low cost. For each update of B_{k+1} requires only the current value B_k , the iteration points u_k and u_{k+1} , the gradients $\nabla J(u_k)$ and $\nabla J(u_{k+1})$. Schematically the algorithm is as follows:

1. Initialization: choose a point u_0 - an initial guess; $g_0 = \nabla J(u_0)$; B_0 .
2. Iterations: compute u_{k+1}
Check the stopping criterion
 - If the stopping criterion is satisfied: terminate optimization with the solution $u^* = u_k$.
 - If not:
 - Calculate the descent direction: $d_k = B_k g_k$
 - Perform the linear search: ρ_k
 - Update the iteration point: $u_{k+1} = u_k - \rho_k d_k$
 - $g_{k+1} = \nabla J(u_{k+1})$
 - $s_k = u_{k+1} - u_k$
 - $y_k = g_{k+1} - g_k$
 - Update the inverse hessian approximation B_{k+1} :
 - $B_{k+1} = B_{k+1}(B_k, s_k, y_k)$
 - Go to the step 2.

A good choice of the inverse hessian approximation is the main challenge of this algorithm. For example, if the update is just an identity matrix, the quasi-Newton method becomes the steepest descent method with an optimal step.

Quasi-Newton methods: Secant condition, BFGS algorithm

Coming back to the quadratic approximation $Q(u)$ of $J(u)$ (1.1):

$$Q_k(u) = J(u_k) + (u - u_k)^T \nabla J(u) + \frac{1}{2} (u - u_k)^T B_k^{-1} (u - u_k) \quad (1.2)$$

The secant methods ask that the gradient of this quadratic approximation agrees with the gradient of the function in the iteration points. That is:

$$\begin{aligned} \nabla Q_k(x_k) &= \nabla J(u_k) \\ \nabla Q_k(x_{k-1}) &= \nabla J(u_{k-1}) \end{aligned} \quad (1.3)$$

Using (1.2) this leads to the secant condition (1.4).

$$B_{k+1} (\nabla J(u_{k+1}) - \nabla J(u_k)) = u_{k+1} - u_k \quad (1.4)$$

As B_{k+1} is an approximation of the hessian matrix, a natural additional condition imposed on it is its symmetry. The BFGS (Broyden-Fletcher-Goldfarb-Shanno), [Fletcher and Powell, 1963], [Broyden, 1969], update B_{k+1} chooses among

all updates satisfying the secant condition (1.4) the closest to the current approximation B_k .

In sum, the BFGS update is given by solution of the following problem:

$$B_{k+1} = \min_B \|B - B_k\|_W^2 \quad (1.5)$$

with B satisfying symmetry and secant conditions.

In (1.5), $\|\cdot\|_W$ is a weighted Frobenius norm:

$$\|B\|_W = \|W^{1/2}BW^{1/2}\|_F, \quad \|B\|_F^2 = \sum_{i,j} b_{i,j}^2$$

with the weight chosen as the inverse of the average Hessian:

$$\tilde{H}_k = \int_0^1 \nabla^2 J(u_k + \tau(u - u_k)) d\tau, \quad W_k = [\tilde{H}_k]^{-1}.$$

The solution of (1.5) gives a BFGS update formula:

$$B_{k+1} = U(B_k, s_k, y_k) = \left(I - \frac{s_k \otimes y_k}{y_k \cdot s_k} \right) B_k \left(I - \frac{y_k \otimes s_k}{y_k \cdot s_k} \right) + \frac{s_k \otimes s_k}{y_k \cdot s_k} \quad (1.6)$$

with " \otimes " an outer product, " \cdot " a scalar product and, as before, $s_k = u_{k+1} - u_k$, $y_k = \nabla J(u_{k+1}) - \nabla J(u_k)$.

Storage efficient implementation of BFGS algorithm

In the quasi-Newton method the approximations of the inverse hessian matrices B_k do not have to be calculated explicitly. In fact, they are needed only for the computation of the descent direction $d_k = B_k g_k$. This means that every B_k is used only multiplied by vector $g_k = \nabla J(u_k)$. Using the BFGS update formula (1.6), the quasi-Newton algorithm can be rewritten as follows.

1. Initialization: choose a point u_0 - an initial guess; $g_0 = \nabla J(u_0)$; B_0 .

2. Iterations: compute u_{k+1}
 Check the stopping criterion

- If the stopping criterion is satisfied: terminate optimization with the solution $u^* = u_k$.
- If not:
 Calculate the descent direction: $d_k = B_k g_k$

$$d_k = g_k \text{ // initialization}$$

$$\text{for } i = k-1, \dots, 1$$

$$\alpha_i = \frac{s_i^T d_k}{y_i^T s_i}$$

$$d_k = d_k - \alpha_i y_i$$

$$d_k = B_0 d_k$$

$$\text{for } i = 1, \dots, k-1$$

$$\beta_i = \frac{y_i^T d}{y_i^T s_i}$$

$$d_k = d_k + s_i (\alpha_i - \beta_i)$$

Perform the linear search: ρ_k
 Update the iteration point: $u_{k+1} = u_k - \rho_k d_k$
 $g_{k+1} = \nabla J(u_{k+1})$
 $s_k = u_{k+1} - u_k$
 $y_k = g_{k+1} - g_k$
 Go to the step 2.

In the presented algorithm all vectors $\{s_k\}$, $\{y_k\}$ are stored, but it allows to avoid a storage of the matrix B_k .

Limited-memory BFGS

Limiter-memory BFGS (L-BFGS) allows to push the idea of the storage efficiency even further. With increase of the number of iterations the storage requirements grows, as the vectors $\{s_k\}$, $\{y_k\}$ should be stored for each iteration. The core of the L-BFGS is not to go down till B_0 in previous algorithm, but to use only last M iterations. This means that only M pairs of vectors s_k , y_k have to be stored.

For the first M iterations of minimization the update formula (1.6) stays unchanged on every step:

$$B_{k+1} = U(B_k, s_k, y_k), \quad \text{for } 0 \leq k \leq M-1.$$

When the number of iterations is greater than M , last M matrices are updated according to (1.6), and B_{k-M} is approximated by a diagonal matrix D_{k-M} . That is, for $k > M$ the update B_k is found from the iterations:

$$\begin{cases} B_k^0 = D_k \\ \text{for } i = 0, \dots, M-1 \\ \quad B_k^{i+1} = U(B_k^i, s_{k-M+i}, y_{k-M+i}) \\ B_k = B_k^M \end{cases}$$

This means, the descent direction d_k for $k > M$ is found as follows:

$$\begin{cases} d_k = g_k // \text{initialization} \\ \text{for } i = k-1, \dots, k-M+1 \\ \quad \alpha_i = \frac{s_i^T d_k}{y_i^T s_i} \\ \quad d_k = d_k - \alpha_i y_i \\ d_k = D_k d_k \\ \text{for } i = k-M+1, \dots, k-1 \\ \quad \beta_i = \frac{y_i^T d}{y_i^T s_i} \\ \quad d_k = d_k + s_i (\alpha_i - \beta_i) \end{cases} \quad (1.7)$$

There exist many variants of the choice of matrix D_k in (1.7), [Zhu et al., 1999], [Gilbert and Lemaréchal, 1989]).

The L-BFGS algorithm cannot be used for the minimization of the non-differentiable functions. The non-differentiability of the cost function appears, for example, in problems with L_1 regularization. An Orthant-Wise Limited-memory Quasi-Newton (OWL-QN) algorithm, based on L-BFGS, was proposed for these cases in [Andrew and Gao, 2007].

1.2 Adjoint approach to optimization with PDE constraints

The adjoint state method ([Chavent, 1974],[Lions, 1971]) allows to compute the gradient of a function in an efficient way. It is widely used for different fields. A non-exhaustive list of applications includes: data assimilation in geophysics ([Plessix, 2006],[Tromp et al., 2005],[Sei et al., 1994]), meteorology ([Dimet and Talagrand, 1986],[Auroux and Blum, 2002],[Auroux, 2003]), oceanology ([Di Lorenzo et al., 2007],[Luong et al., 1998]); shape optimization ([Reuther et al., 1999],[Giles and Pierce, 2000],[Nadarajah, 2003], [Brandenburg et al., 2009]).

1.2.1 Variational formulation

Let us consider a problem of minimization of the cost function $J(u)$:

$$J(u) = C(z(u), u). \quad (1.8)$$

$u \in \mathbf{U}$ represents the model parameters, \mathbf{U} - space of the model parameters. $z \in \mathbf{Z}$ is a state variable, that satisfies a direct problem (1.9), \mathbf{Z} - space of the state variable.

For a fixed choice of the model parameters the state variable z is found as a solution of the following direct problem:

$$D(z(u), u) = 0. \quad (1.9)$$

C and D above are continuously differentiable.

An arbitrary admissible variation δu of the model parameters leads to the variation δz of the state variable z and the variation δJ of the cost function. The variation δz is such that $z + \delta z$ is a solution of the direct problem (1.9) corresponding to a choice of parameters $u + \delta u$. In first approximation the direct problem gives:

$$D(z + \delta z, u + \delta u) = D(z, u) + \left\langle \frac{\partial D}{\partial z}, \delta z \right\rangle_{\mathbf{Z}} + \left\langle \frac{\partial D}{\partial u}, \delta u \right\rangle_{\mathbf{U}}.$$

Both $D(z, u)$ and $D(z + \delta z, u + \delta u)$ satisfy (1.9), so the previous approximation implies:

$$\left\langle \frac{\partial D}{\partial z}, \delta z \right\rangle_{\mathbf{Z}} = - \left\langle \frac{\partial D}{\partial u}, \delta u \right\rangle_{\mathbf{U}} \quad (1.10)$$

$$\delta J = \left\langle \frac{\partial C(z, u)}{\partial z}, \delta z \right\rangle_{\mathbf{Z}} + \left\langle \frac{\partial C(z, u)}{\partial u}, \delta u \right\rangle_{\mathbf{U}} \quad (1.11)$$

Substitution of (1.10) into (1.11) gives:

$$\delta J = - \left\langle \left(\left(\frac{\partial D(z, u)}{\partial z} \right)^{-1} \right)^* \frac{\partial C(z, u)}{\partial z}, \frac{\partial D(z, u)}{\partial u} \delta u \right\rangle_{\mathbf{z}} + \left\langle \frac{\partial C(z, u)}{\partial u}, \delta u \right\rangle_{\mathbf{u}} \quad (1.12)$$

Here $*$ indicates the adjoint operator. Using a property $(A^*)^{-1} = (A^{-1})^*$, an adjoint state p is introduced as a solution of the following adjoint problem:

$$\left(\frac{\partial D(z, u)}{\partial z} \right)^* p = - \frac{\partial C(z, u)}{\partial z}. \quad (1.13)$$

Thus, the derivative of the cost function:

$$J'(u) = \left(\frac{\partial D}{\partial u}(z, u) \right)^* p + \frac{\partial C}{\partial u} \quad (1.14)$$

So, the gradient of the cost function is obtained from the following algorithm:

$\left[\begin{array}{l} \text{Solve the direct problem (1.9): } z(u) \\ \text{Solve the adjoint problem (1.13): } p(u) \\ \text{Compute the gradient of the cost function via (1.14): } J'(u) \end{array} \right]$

The advantage of the adjoint approach rests on the fact that the adjoint problem (1.13) does not depend on the variation of the parameters δu in contrast with (1.10). As a result, when the adjoint approach is used, the computation of the gradient of the cost function requires one run of the adjoint problem. When gradient is calculated via Fréchet derivatives, (1.10) should be considered separately for independent variation of each model parameter. That means that (1.10) is solved a number of times equal to the number of model parameters.

1.2.2 A Lagrangian formulation

The problem of minimization of the cost function can be considered as a minimization problem with an equality constraint: find u^* minimizing $C(z, u)$ under the constraint $D(z, u) = 0$. A Lagrangian associated to this problem is:

$$L(z, u, p) = C(z, u) + \langle p, D(z, u) \rangle_{\mathbf{z}}. \quad (1.15)$$

According to optimization theory, [Ciarlet et al., 1989], the minimum of the cost function corresponds to a saddle point of the Lagrangian: the point of maximum with respect to p and minimum with respect to z . The Lagrange multiplier p

in (1.15) is exactly the previously introduced adjoint state. Indeed, when z is a solution of direct problem (1.9), the cost function becomes:

$$J(u) = C(z(u), u) = C(z(u), u) + \langle p, D(z(u), u) \rangle_{\mathbf{Z}} = L(u, z(u), p).$$

Differentiation of this expression gives:

$$\langle J', \delta u \rangle_{\mathbf{U}} = \langle L_u(z(u), u, p), \delta u \rangle_{\mathbf{U}} + \langle L_z(z(u), u, p), z'(u) \delta u \rangle_{\mathbf{Z}}.$$

A choice of $p = p(u)$ such that $L_z(z(u), u, p) = 0$ implies that p should be a solution of the adjoint problem (1.13). In fact:

$$\langle L_z(z, u, p), \delta z \rangle_{\mathbf{Z}} = \langle C_z(z, u), \delta z \rangle_{\mathbf{Z}} + \langle p, D_z(z, u) \delta z \rangle_{\mathbf{Z}} = \langle C_z + D_z^*(z, u)p, \delta z \rangle_{\mathbf{Z}},$$

and a right-hand side of this expression becomes zero for any δz only when $C_z + D_z^*(z, u)p = 0$, what is exactly (1.13). That means that the adjoint state can be viewed as a Lagrange multiplier.

In practice, the direct and adjoint problems can often be solved only numerically. It implies discretization of the variables. But the operations of discretization and of taking the adjoint are not commutative ([Nadarajah and Jameson, 2001]). It means that the gradient of the cost function should be computed via the adjoint to the discrete direct problem ([Giles et al., 2003]), and not via the discretization of the continuous adjoint problem. This situation is described schematically on Figure 1.1. The following section gives simple illustration of this problem on the example of transport equation.

Example of the transport equation

Let us take an example of the transport equation:

$$\frac{\partial u}{\partial t} + v \frac{\partial u}{\partial x} = 0. \quad (1.16)$$

The cost function at the final time $t = T$

$$J = \frac{1}{2} \int_{\Omega} (Z(x, T) - Z_{exp}(x))^2 dx \quad (1.17)$$

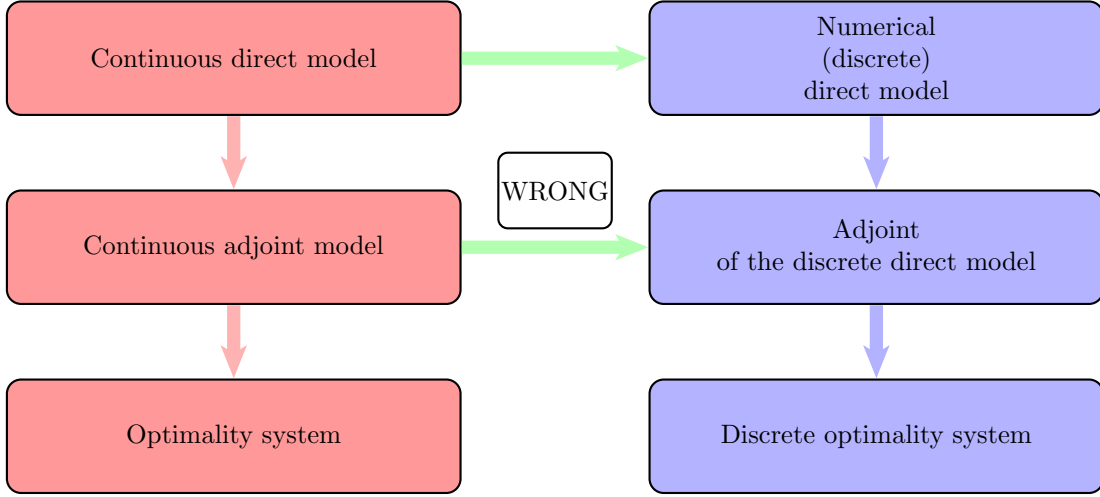


Figure 1.1 – General framework of the adjoint approach.

We consider the variation y of the solution u : $u \rightarrow u + \epsilon y$.

$$\frac{\partial y}{\partial t} = -v \frac{\partial y}{\partial x} = Ay.$$

The adjoint to the operator $A = -v \frac{\partial \cdot}{\partial x}$ is $A^* = +v \frac{\partial \cdot}{\partial x}$. This implies the following equation for the adjoint state:

$$-\frac{\partial P}{\partial t} = v \frac{\partial P}{\partial x} \quad (1.18)$$

For the positive speed $v > 0$ we use backward differences discretization of the transport equation (1.16):

$$\frac{Z_{m,n+1} - Z_{m,n}}{\Delta t} + v \frac{Z_{m,n} - Z_{m-1,n}}{\Delta x} = 0. \quad (1.19)$$

The discrete Lagrangian becomes:

$$L = \frac{1}{2} \sum_{m=1}^M (Z_{m,N} - Z_{exp}^m)^2 + \sum_{m=1}^M \sum_{n=1}^N P_{m,n} \left(\frac{Z_{m,n+1} - Z_{m,n}}{\Delta t} + v \frac{Z_{m,n} - Z_{m-1,n}}{\Delta x} \right) \quad (1.20)$$

Variation of $Z_{m,n} \rightarrow Z_{m,n} + \epsilon Y_{m,n}$ leads to:

$$\begin{aligned} & \frac{L(\{Z_{m,n} + \epsilon Y_{m,n}\}, \{P_{m,n}\}) - L(\{Z_{m,n}\}, \{P_{m,n}\})}{\epsilon} = \\ & = \sum_{m=1}^N Y_{m,N} (Z_{m,N} - Z_{exp}^m) + \sum_{m=1}^M \sum_{n=1}^N P_{m,n} \left(\frac{Y_{m,n+1} - Y_{m,n}}{\Delta t} + v \frac{Y_{m,n} - Y_{m-1,n}}{\Delta x} \right) \end{aligned} \quad (1.21)$$

Change of summation leads to the following adjoint problem:

$$\frac{P_{m,n} - P_{m,n-1}}{\Delta t} + v \frac{P_{m+1,n} - P_{m,n}}{\Delta x} = 0 \quad (1.22)$$

with a condition for the final time $t = T$: $P_{m,N-1} + (Z_{m,N} - Z_{exp}^N) = 0$.

We obtained a forward difference scheme for the solution of the adjoint problem (1.18), and not a backward difference scheme used for modeling of the direct problem (1.16). This result is somehow expected, cause the adjoint problem equation is also a transport equation with positive speed, but it should be solved backward in time: from $t = T$ to $t = 0$. Once a particular discretization of the direct problem is chosen, the discrete adjoint problem should be derived taking into account this choice.

1.3 Automatic differentiation approach

In this section we consider a situation when the cost function J is represented by a computer program \mathcal{P} . For each set of n input scalar parameters $\{u_i, i = \overline{1, n}\}$ program \mathcal{P} returns the value $J(u)$. This program is obtained as follows. First, the direct problem (1.9) is solved numerically to obtain the state variable z corresponding to $\{u_i, i = \overline{1, n}\}$. Then, the cost function J (1.8) is computed numerically.

In many cases the application of the Lagrangian approach to the minimization problem with a complicated direct problem is impossible. But one still has to calculate the gradient of the cost function for the optimization procedure. The most straightforward solution is utilization of the finite differences. For example, for the cost function J that depends on a set of n parameters $\{u_i, i = \overline{1, n}\}$, the i -component of the gradient can be computed as follows:

$$\frac{\partial J}{\partial u_i} = \frac{J(u_1, \dots, u_i + h, \dots, u_n) - J(u_1, \dots, u_i, \dots, u_n)}{h} + \mathcal{O}(h)$$

This approach is expensive when number of calibration parameters n is large, because for computation of each component of the gradient the value of the cost function must be recalculated in an additional point, which involves additional run of the direct problem. What is more the final differences approach results in introduction of the discretization error of order h in the computed gradient.

Automatic differentiation (AD) allows to overcome these issues. It permits to find the numerical value of the derivative of any algebraic function ([Wengert, 1964], [Griewank and Walther, 2008]). This approach avoids the analytical finding of the derivative and, at the same time, does not introduce the error of discretization inherent for the finite differences.

The direct problem can be solved only numerically. So, in the end of the day, the cost function is represented by a sequence of operations in the computer program \mathcal{P} . This program takes on its entry n values of the parameters $\{u_i, i = \overline{1, n}\}$ and returns the corresponding value of the cost function J . \mathcal{P} consists of the sequence of elementary operations: operations of control (loops, tests), algebraic operations (addition, subtraction, multiplication,...) and the application of the intrinsic functions of the programming language (trigonometric function, logarithm, exponent,...). Automatic differentiation approach exploits the fact that each separated operation, except for a conditional test, inside the computer program \mathcal{P} is differentiable. A presence of a conditional test leads to only piecewise differentiable functions. This is an open research problem in the field of AD. The differentiability of the separate operations allows to trace the derivatives of the output of \mathcal{P} corresponding to changes in the input. Roughly speaking, the automatic differentiation is founded on the application of the chain rule to the sequence of elementary operations of the computer program \mathcal{P} . It is important to emphasize that the automatic

differentiation is not equivalent to the analytic differentiation routine of some software (MATLAB, Maple, etc.). We will consider some illustrative examples later in this section.

In the first part of this section we will consider the tangent and the adjoint modes of the automatic differentiation. In the last section we will give a short introduction to a particular automatic differentiation software TAPENADE [Hascoet and Pascual, 2013], developed at INRIA Sophia - Antipolis by the Tropics and later on by Ecuador teams.

Everywhere in this section the considered function is scalar one, because it is the case for the introduced later on cost functions.

1.3.1 Different modes of the Automatic Differentiation

We consider a program \mathcal{P} defined by a sequence of N instructions I_1, I_2, \dots, I_N . Each of these instructions I_k acts on the current program variables W_{k-1} in a differentiable way and can be represented by a function f_k as follows:

$$I_k : \quad W_k = f_k(W_{k-1}).$$

Program variables W_0 correspond to the program input X . The number of the variable W_k stays the same after each instruction.

The output of the program can be regarded as an output of a composite function (1.23).

$$f = f_N \circ f_{N-1} \circ f_{N-2} \circ \dots \circ f_1. \quad (1.23)$$

Application of the chain rule to the function (1.23), gives the following derivative of the program output $f'(X)$ for the given input X :

$$\begin{aligned} f'(X) &= (f'_N \circ f_{N-1} \circ f_{N-2} \circ \dots \circ f_1(X)) \\ &\quad \cdot (f'_{N-1} \circ f_{N-2} \circ \dots \circ f_1(X)) \\ &\quad \cdot \dots \\ &\quad \cdot f'_1(X) \\ &= f'_N(W_{N-1}) \cdot f'_{N-1}(W_{N-2}) \cdot \dots \cdot f'_1(W_0) \end{aligned} \quad (1.24)$$

Let us consider an example of application of (1.24) to a very simple program computing $f(x_1, x_2) = x_1 \sin^2(x_2)$. Given an input $X = W_0 = \begin{pmatrix} x_1 \\ x_2 \end{pmatrix}$, the program

performs the following sequence of instruction:

$$\begin{aligned} I_1 : \quad f_1(W_0) &= W_1 = \begin{pmatrix} W_{0,1} \\ \sin(W_{0,2}) \end{pmatrix} \\ I_2 : \quad f_2(W_1) &= W_2 = \begin{pmatrix} W_{1,1} \\ W_{1,2}^2 \end{pmatrix} \\ I_3 : \quad f_3(W_2) &= W_3 = W_{2,1}W_{2,2} \end{aligned}$$

Here $W_{i,j}$ denotes j^{th} variable after run of i instructions.

The corresponding Jacobian matrices are:

$$\begin{aligned} f'_1(W_0) &= \begin{pmatrix} 1 & 0 \\ 0 & \cos(W_{0,2}) \end{pmatrix} & f'_2(W_1) &= \begin{pmatrix} 1 & 0 \\ 0 & 2W_{1,2} \end{pmatrix} & (1.25) \\ f'_3(W_2) &= (W_{2,2} \quad W_{2,1}) \end{aligned}$$

Substitution of matrices (1.25) into (1.24) with further multiplication from right to left leads to the required derivative f' :

$$f'(X) = f'_3(W_2) \cdot f'_2(W_1) \cdot f'_1(W_0) = (\sin^2(x_2) \quad 2x_1 \sin(x_2) \cos(x_2)).$$

So, computation of f' requires computation of the Jacobian matrix corresponding to each instruction of the program \mathcal{P} with further multiplication of these matrices. When the number of input variables X grows, the direct application of this method becomes too expensive, because of the cost of the large matrices storage and multiplication.

Tangent mode of the Automatic Differentiation

The task is much simpler when only directional derivative (sensitivity) of the output is required. In this case, given a variation of the input variables \dot{X} , one is looking for the corresponding variation \dot{Y} of the output. It follows from (1.24) that this sensitivity is given by (1.26).

$$\dot{Y} = f'_N(W_{N-1}) \cdot f'_{N-1}(W_{N-2}) \cdot \dots \cdot f'_1(W_0) \dot{X} \quad (1.26)$$

In (1.26) the multiplication is performed from the right to the left, as before. But now the task is simplified because the matrix-matrix product is substituted by the matrix-vector product. Moreover, the Jacobian matrices do not have to be calculated explicitly. f'_i appears in multiplication (1.26) from f'_1 to f'_N , that is in the same order as the instructions of the program \mathcal{P} . So, the calculation of the sensitivities for each step of the program (the consecutive matrix-vector multiplications in (1.26)) can be carried out along with the run of the program \mathcal{P} .

Table 1.1 – List of tangent operations

ϕ	$\left[\phi, \dot{\phi} \right]$
$v = c$	$v = c; \quad \dot{v} = 0$
$v = u \pm w$	$v = u \pm w; \quad \dot{v} = \dot{u} \pm \dot{w}$
$v = u * w$	$v = u * w; \quad \dot{v} = \dot{u} * w + u * \dot{w}$
$v = \frac{1}{u}$	$v = \frac{1}{u}; \quad \dot{v} = -v^2 * \dot{u}$
$v = \sqrt{u}$	$v = \sqrt{u}; \quad \dot{v} = 0.5 * \dot{u}/v$
$v = \exp(u)$	$v = \exp(u); \quad \dot{v} = v * \dot{u}$
$v = \sin(u)$	$v = \sin(u); \quad \dot{v} = \cos(u) * \dot{u}$

Table 1.2 – Example of the tangent mode of AD

Original program: $x_1, x_2 \rightarrow y$	Tangent mode $x_1, \dot{x}_1, x_2, \dot{x}_2 \rightarrow y, \dot{y}$
$v_{-1} = x_1$	$v_{-1} = x_1$
$v_0 = x_2$	$\dot{v}_{-1} = \dot{x}_1$ $v_0 = x_2$ $\dot{v}_0 = \dot{x}_2$
$v_1 = \sin(v_0)$	$v_1 = \sin(v_0)$ $\dot{v}_1 = \cos(v_0) * \dot{v}_0$
$v_2 = v_1^2$	$v_2 = v_1^2$ $\dot{v}_2 = 2v_1 \dot{v}_1$
$v_3 = v_{-1}v_2$	$v_3 = v_{-1}v_2$ $\dot{v}_3 = v_{-1}\dot{v}_2 + \dot{v}_{-1}v_2$
$y = v_3$	$y = v_3$ $\dot{y} = \dot{v}_3$

In practice it implies that for each elementary operation ϕ of the original program \mathcal{P} an additional operation $\dot{\phi}$ is added. Each $\dot{\phi}$ traces the tangent derivative of ϕ , corresponding to the variation of its inputs.

Table 1.1 gives some frequent examples of the computation of ϕ and $\dot{\phi}$

Table 1.2 presents a simple example of the application of the tangent mode of AD to the program computing $y = x_1 \sin^2(x_2)$. A differentiated program \mathcal{P}' returns the sensitivity \dot{y} corresponding to the variation $\dot{X} = \begin{pmatrix} \dot{x}_1 \\ \dot{x}_2 \end{pmatrix}$

Adjoint mode of the Automatic Differentiation

Let us consider f'^T in (1.24):

$$f'^T = f_1'^T(W_0) \cdot \dots \cdot f_{N-1}'^T(W_{N-2}) \cdot f_N'^T(W_{N-1}) \quad (1.27)$$

Table 1.3 – Example of the adjoint mode of AD.

$v_{-1} = x_1$
$v_0 = x_2$
$v_1 = \sin(v_0)$
$v_2 = v_1^2$
$v_3 = v_{-1} * v_2$
$y = v_3$
$\bar{v}_3 = \bar{y}$
$\bar{v}_{-1} = \bar{v}_3 * v_2$
$\bar{v}_2 = \bar{v}_3 * v_{-1}$
$\bar{v}_1 = \bar{v}_2 * 2v_1$
$\bar{v}_0 = \bar{v}_1 * \cos(v_0)$
$\bar{x}_2 = \bar{v}_0$
$\bar{x}_1 = \bar{v}_{-1}$

An application of (1.27) to the considered above function $f(x_1, x_2) = x_1 \sin^2(x_2)$ gives:

$$\begin{aligned} f'^T(X) &= f'_1(W_0) \cdot f'_2(W_1) \cdot f'_3(W_3) \\ &= \begin{pmatrix} 1 & 0 \\ 0 & \cos(W_{0,2}) \end{pmatrix} \begin{pmatrix} 1 & 0 \\ 0 & 2W_{1,2} \end{pmatrix} \begin{pmatrix} W_{2,2} \\ W_{2,1} \end{pmatrix} = \begin{pmatrix} \sin^2(x_2) \\ 2x_1 \sin(x_2) \cos(x_2) \end{pmatrix} \end{aligned}$$

The advantage of (1.27) comes from the order of multiplication. When moving from right to left, all multiplications are matrix by vector. But, in contrast with the tangent mode, the values W_i appears in (1.27) from W_{N-1} to W_0 , that is in order reversed to the order of instructions in \mathcal{P} . That means the program \mathcal{P} should be executed before the beginning of gradient computation. Moreover, all intermediate values W_i are needed in (1.27), so they should be either stored during the run of \mathcal{P} or recalculated.

Table 1.3 presents a simple example of the application of the adjoint mode of AD to the program computing $y = x_1 \sin^2(x_2)$. An adjoint variable $\bar{v}_i = \frac{\partial y}{\partial v_i}$ is associated with every intermediate variable v_i . Then the differentiation is carried out in the reverse mode from the last variable (the output of the program y) down to the first variable (the input of the program). This process is initiated with $\bar{y} = 1$, by definition of the adjoint variable. A differentiated program \mathcal{P}' returns the gradient of the function $\nabla f(x_1, x_2) = \begin{pmatrix} \bar{x}_1 \\ \bar{x}_2 \end{pmatrix}$.

There is a connection between the adjoint variables \bar{v}_i in the adjoint mode of AD and the discrete version of adjoint state variables p_i from the Section 1.2.2

([Griewank and Walther, 2008]). In fact, \bar{v}_i can be viewed as a Lagrange multiplier for the equality constraint $\left(v_i - \phi_i(v_j)_{j \prec i} = 0\right)$ during the minimization of the objective function y . Each such equality constraint corresponds to one of the program instruction $v_i = \phi_i(v_j)_{j \prec i}$, where ϕ_i is an elementary operation (for example, one from the Table 1.1). The relation $j \prec i$ means that v_i depends on v_j directly. For example, in Table 1.3 $2 \prec 3$, but $1 \not\prec 3$.

1.3.2 Automatic Differentiation Engine TAPENADE

There are two approaches to the implementation of the AD: by program transformation and by operator overloading. The site www.autodiff.org can serve as a reference point for existing AD software. In this thesis the automatic differentiation software TAPENADE [Hoccoet and Pascual, 2013] was used. TAPENADE stands for "Tangent and Adjoint PENultimate Automatic Differentiation Engine". It was developed at INRIA Sophia - Antipolis by the Tropics and later on by Ecuador teams. TAPENADE is based on the AD by program transformation.

TAPENADE can be used as a web server:

<http://www-tapenade.inria.fr:8080/tapenade/index.jsp>.

Figure 1.2 presents the on-line interface of the TAPENADE. The variable y , that user wants to differentiate, is calculated by program \mathcal{P} . This program is passed as an input to TAPENADE. \mathcal{P} can be written in C, Fortran95 or Fortran77. A parser reads the code line by line. Then an additional variable is added for each active variable v of the code: the derivative \dot{v} in tangent mode, which is denoted automatically vd by TAPENADE; the adjoint variable \bar{v} in adjoint mode, which is denoted vb . The additional lines of instructions for calculation of derivatives are added to the source code.

Figure 1.3 gives an example of the differentiation in the tangent mode of the simple program **MAIN**. **MAIN** calculates the value of the function

$y(x_1, x_2) = x_1 \sin^2(x_2)$. y was passed in TAPENADE as a dependent variable, x_1 and x_2 as independent. The differentiated program **MAIN_D** is on the right-hand side column. **MAIN_D** requires two additional inputs $x1d$ and $x2d$ that correspond to \dot{x}_1 and \dot{x}_2 in the notations of Section 1.3.1. **MAIN_D** returns additional variable yd that contains the value of the derivative of y in the direction $\begin{pmatrix} x1d \\ x2d \end{pmatrix}$. If one wants to compute the gradient of f using the tangent mode, the differentiated program **MAIN_D** should be run twice: with the inputs $\begin{pmatrix} x1d \\ x2d \end{pmatrix} = \begin{pmatrix} 1.0 \\ 0.0 \end{pmatrix}$ for the first entry of the gradient and $\begin{pmatrix} x1d \\ x2d \end{pmatrix} = \begin{pmatrix} 0.0 \\ 1.0 \end{pmatrix}$ for the second. As was discussed in the Section 1.3.1 this approach to the gradient calculation becomes too expensive with grows of the number of independent variables.

Figure 1.4 gives an example of the differentiation in the adjoint mode of the simple program calculating $y(x_1, x_2) = x_1 \sin^2(x_2)$. The original program is **MAIN** in the left column. y was passed in TAPENADE as a dependent variable, x_1 and x_2 as the independent ones. The differentiated program **MAIN_B** requires one additional input $yb = \bar{y}$. In the exit program provides the gradient of the cost function with respect to the set of independent variables: $\begin{pmatrix} x1b \\ x2b \end{pmatrix}$, that correspond to $\begin{pmatrix} \bar{x}_1 \\ \bar{x}_2 \end{pmatrix}$

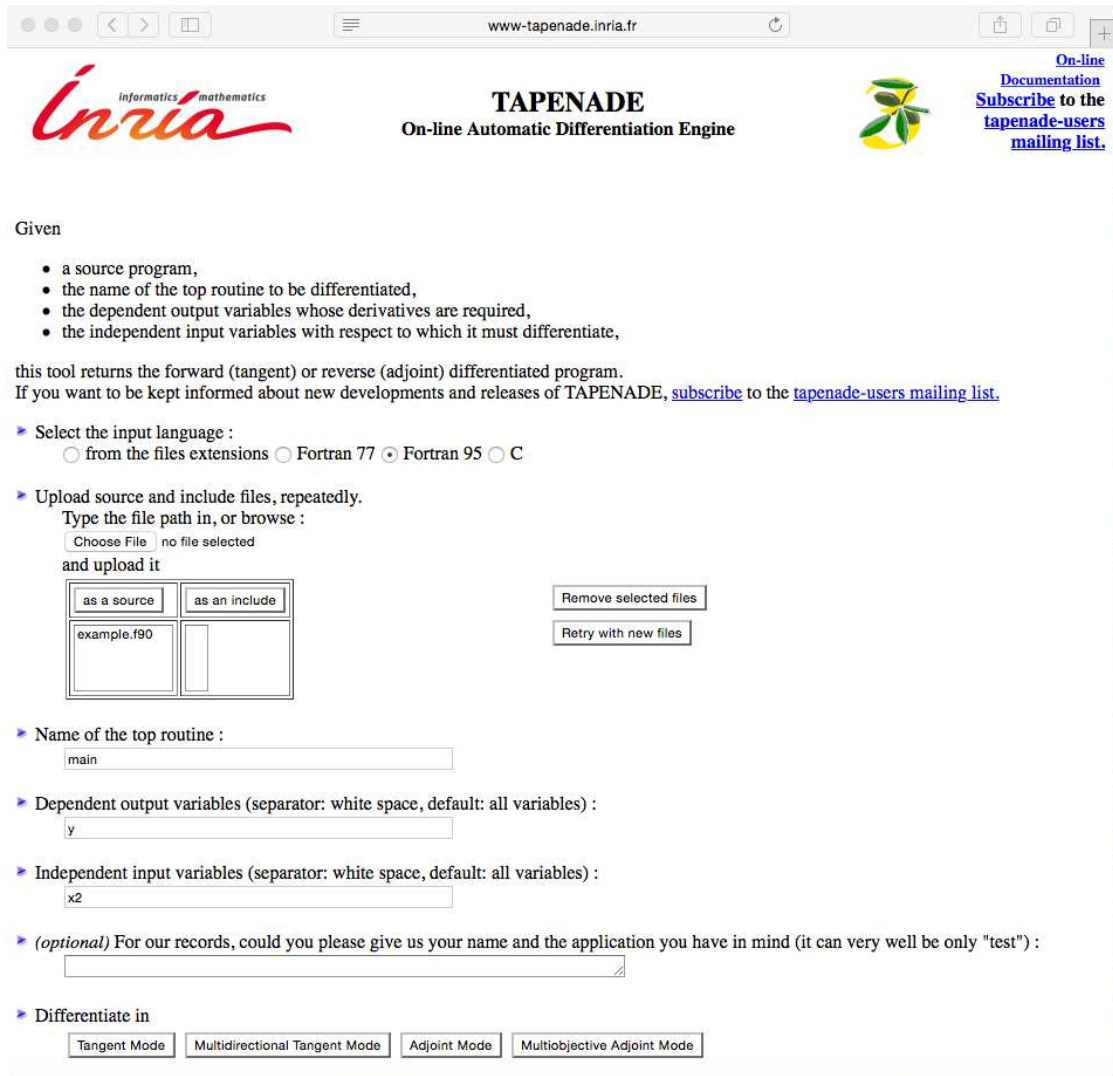


Figure 1.2 – Interface of the online differentiation engine.

TAPENADE Differentiation result
tapenade.inria.fr:8080/tapenade/result.html

Original call graph	Differentiated call graph
<p>subroutine EXAMPLE Calls subroutine MAIN</p> <pre> ! Generated by TAPENADE (INRIA, Ecuador team) ! Tapenade 3.11 (r6148) - 16 Aug 2016 14:18 ! SUBROUTINE MAIN(x1, x2, y) IMPLICIT NONE REAL(kind=8), INTENT(IN) :: x1, x2 REAL(kind=8), INTENT(OUT) :: y INTRINSIC SIN y = x1*SIN(x2)**2 END SUBROUTINE MAIN </pre>	<p>subroutine MAIN_D</p> <pre> ! Generated by TAPENADE (INRIA, Ecuador team) ! Tapenade 3.11 (r6148) - 16 Aug 2016 14:18 ! ! Differentiation of main in forward (tangent) mode: ! variations of useful results: y ! with respect to varying inputs: x1 x2 ! RW status of diff variables: y:out x1:in x2:in SUBROUTINE MAIN_D(x1, x1d, x2, x2d, y, yd) IMPLICIT NONE REAL(kind=8), INTENT(IN) :: x1, x2 REAL(kind=8), INTENT(IN) :: x1d, x2d REAL(kind=8), INTENT(OUT) :: y REAL(kind=8), INTENT(OUT) :: yd INTRINSIC SIN yd = x1d*SIN(x2)**2 + x1**2*SIN(x2)*x2d*COS(x2) y = x1*SIN(x2)**2 END SUBROUTINE MAIN_D </pre>

Figure 1.3 – Example of the tangent mode of automatic differentiation in TAPENADE environment.

in the notations of Section 1.3.1. In principle, the only result the adjoint differentiation is expected to deliver is the gradient. So, the value of the differentiated function $f(x_1, x_2)$ has disappeared from the differentiated program **MAIN_B**. When this value is needed, as it is the case for the problem of minimization of the cost function, the derived code should be changed by hand.

The screenshot shows the TAPENADE Differentiation result interface. At the top, there are two tabs: "Fortran 90 Tutorial" and "TAPENADE Differentiation result". The "TAPENADE Differentiation result" tab is active. Below it, there are two main sections: "Original call graph" and "Differentiated call graph".

Original call graph:

- subroutine EXAMPLE
- Calls subroutine MAIN

```

! Generated by TAPENADE      (INRIA, Ecuador team)
! Tapenade 3.11 (r6148) - 16 Aug 2016 14:18
!
SUBROUTINE MAIN(x1, x2, y)
  IMPLICIT NONE
  REAL(kind=8), INTENT(IN) :: x1, x2
  REAL(kind=8), INTENT(OUT) :: y
  INTRINSIC SIN
  y = x1*SIN(x2)**2
END SUBROUTINE MAIN

```

Differentiated call graph:

- subroutine MAIN_B

```

! Generated by TAPENADE      (INRIA, Ecuador team)
! Tapenade 3.11 (r6148) - 16 Aug 2016 14:18
!
! Differentiation of main in reverse (adjoint) mode:
! gradient of useful results: y
! with respect to varying inputs: y x1 x2
! RW status of diff variables: y:in-zero x1:out x2:out
SUBROUTINE MAIN_B(x1, x1b, x2, x2b, y, yb)
  IMPLICIT NONE
  REAL(kind=8), INTENT(IN) :: x1, x2
  REAL(kind=8) :: x1b, x2b
  REAL(kind=8) :: y
  REAL(kind=8) :: yb
  INTRINSIC SIN
  REAL*8 :: temp
  temp = SIN(x2)
  x1b = temp**2*yb
  x2b = 2*temp*x1*COS(x2)*yb
  yb = 0.0_8
END SUBROUTINE MAIN_B

```

Figure 1.4 – Example of the adjoint mode of automatic differentiation in TAPENADE environment.

Chapter 2

Abrasive Waterjet Machining

Abrasive waterjet machining (AWJM) is a versatile technology that can be applied to machining of various types of materials [Momber and Kovacevic, 2012]. During this process, the waterjet is created by converting high pressure water into high velocity jet. The abrasive particles are added to the high velocity waterjet (Figure 2.1). Then, in the mixing tube, the momentum of the waterjet is transferred to the abrasive particles. As a result, they are accelerated to high speeds (200-800 m/s). Created mixture of water and abrasive particles is pushed through a small orifice (0.1-0.3 mm), creating an abrasive waterjet plume. This plume hits a target surface resulting in erosion of this surface. The advantages of the AWJM include ([Momber and Kovacevic, 2012]):

- It can be applied to machining of very broad range of materials (from Ti/Ni alloys and ceramics to biological tissues)
- It is a comparably fast technology.
- It involves low cutting forces, thus allowing to avoid the damage of the workpiece.
- It results in low cutting temperatures, and thus can be used for treatment of heat sensitive materials.
- In contrast with conventional chip removal processes, AWJM does not make use of toxic cutting fluids, which makes it environment friendly.

The abrasive waterjet creates a footprint on the target material. The shape of this footprint depends on the target material properties and the physical parameters of the process: the water pump pressure, the abrasive mass flow, the jet feed speed (speed of the AWJ head), the stand-off distance (from the orifice to the target surface). The main challenge of the AWJ technology is the control of the shape that

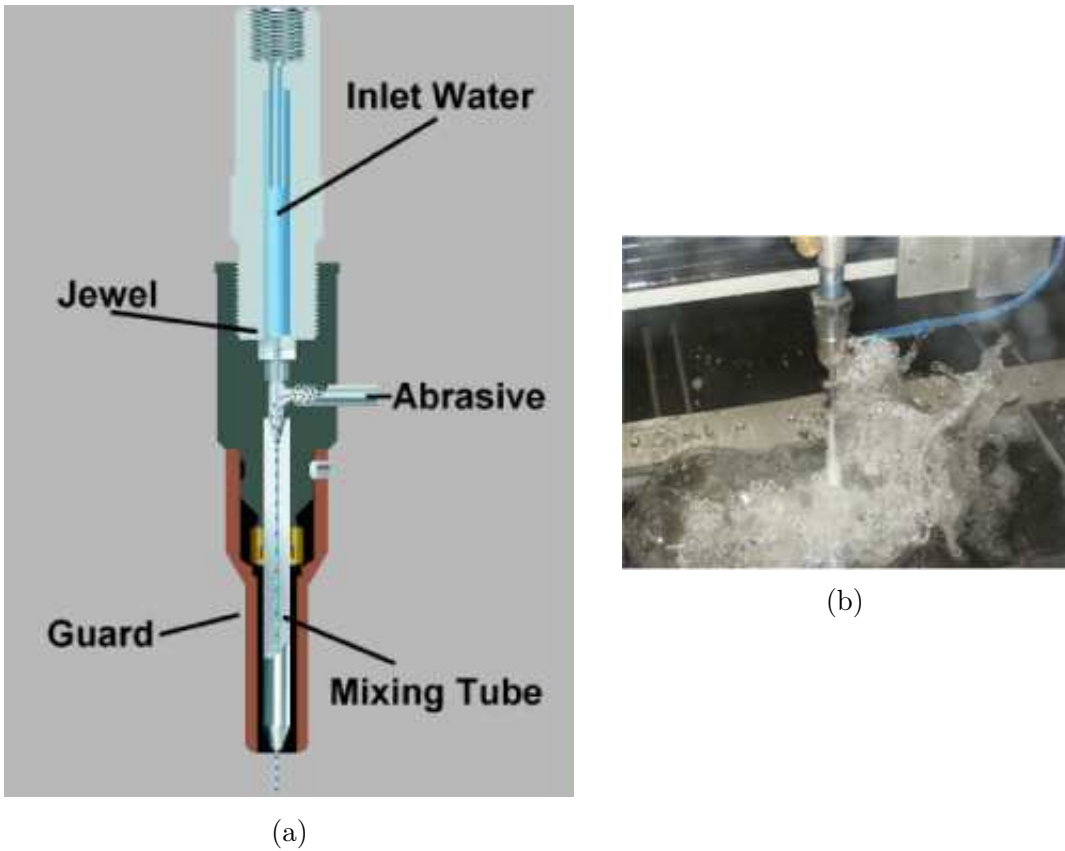


Figure 2.1 – (a) A schematic representation of the abrasive waterjet head. (From <http://waterjets.org/>)
 (b) A photo of the abrasive waterjet in action.

is created. The finite element models ([ElTobgy et al., 2005],[Torrubia et al., 2015]) lead to the high cost in time of computations, making them difficult to integrate into the machining software. The main advantage of the relatively simple analytical PDE models ([Axinte et al., 2010],[Oka et al., 2005],[Kong et al., 2012a], [Billingham et al., 2013]) consists in their low computational cost. This enables integration of such models into the machining software.

2.1 Origins of the geometrical model

Following [Slikkerveer et al., 1998], [Slikkerveer et al., 1999], the erosion effect of the impacting particles on a brittle material can be described with one parameter - their kinetic energy in normal to the surface direction. Introducing the erosion efficiency E_{eff} as a ratio of the weight of removed material to the nor-

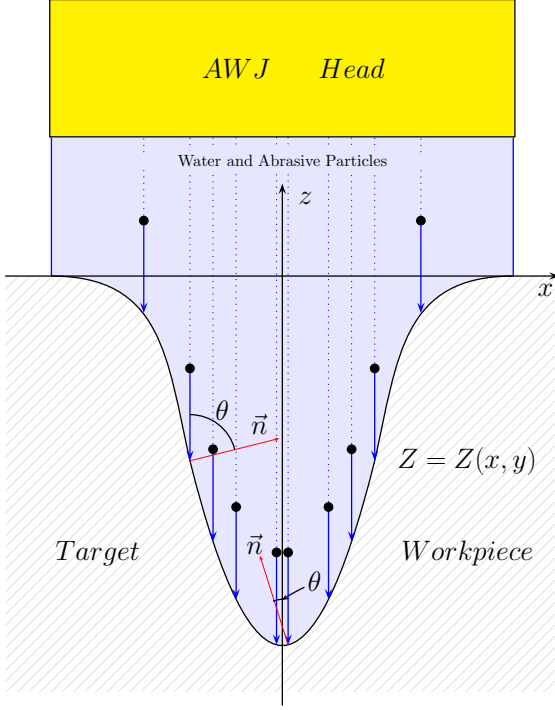


Figure 2.2 – Schematic representation of the cross-section of the waterjet footprint.

mal component of the kinetic energy of the impacting particles, it was shown in [Slirkerveer et al., 1998] that

$$E_{eff} = C_{eff} \left(\frac{1}{2} m (v_n^{abr})^2 \right)^p.$$

Here m is the mass of an individual particle, v_n^{abr} is the normal to the surface component of the speed of the abrasive particles in the jet, and p is a parameter that should be calibrated from the experiment.

When the target surface is described by \vec{r} , the erosion velocity of the surface $\frac{d\vec{r}}{dt}$ is described by (2.1).

$$\frac{\partial \vec{r}}{\partial t} = -\frac{E_{eff} J}{\rho_t} \vec{n} = -C_{eff} \left(\frac{1}{2} m (v_n^{abr})^2 \right)^p \frac{J}{\rho_t} \vec{n}. \quad (2.1)$$

Here J is the flux of kinetic energy, ρ_t is the specific mass of a target material and \vec{n} denotes the normal to the target surface, as Figure 2.2 shows.

Let the eroded surface be uniquely described by the depth, that is by coordinate z in Figure 2.2. From (2.1), the evolution of z with time is described by (2.2).

$$\frac{\partial z}{\partial t} = C_{eff} \left(\frac{1}{2} m (v_{jet}^{abr})^2 \right)^2 \frac{\frac{1}{2} M_{jet} (v_{jet}^{abr})^2}{\rho_t} (\cos \theta)^{2+2p} \quad (2.2)$$

Here θ represents the angle between the jet axis and the normal to the surface \vec{n} , M_{jet} is the mass flux of the erosive particles per jet cross section, v_{jet}^{abr} is the speed of the particles.

For a stationary jet, which hits the surface and stays at the same place, the cosine of local impact angle θ is expressed in term of the slope as $\cos \theta = 1 / \sqrt{1 + \left(\frac{\partial z}{\partial x} \right)^2}$. Introducing a new constant $k = 2 + 2p$, the previous formula (2.2) for $\frac{\partial z}{\partial t}$ becomes:

$$\frac{\partial z}{\partial t} = -C_{eff} \left(\frac{1}{2} m \right)^p \frac{\frac{1}{2} M_{jet} (v_{jet}^{abr})^k}{\rho_t} \left(\frac{1}{\sqrt{1 + \left(\frac{\partial z}{\partial x} \right)^2}} \right)^k. \quad (2.3)$$

In [Slikkerveer et al., 1999], the evolution of the surface governed by (2.3) was studied under the assumption that all parameters of the model are constant in space. That is, without taking into account the spatial velocity and mass distributions within the jet. The experimental measurements of these distributions are very challenging ([Ghobeity et al., 2008],[Balz and Heiniger, 2011],[Balz et al., 2013]). Figure 2.3 shows an example from [Balz and Heiniger, 2011] of the abrasive particles distribution, and thus mass distribution, depending on the distance from the center of the jet. Clearly, a reliable model of the AWJ milling should take into account the variation of the properties within the jet.

Right hand side of (2.2) for normal incident, $\theta = 0^\circ$, defines the etching (material specific erosion) rate, E ([Ghobeity et al., 2008],[Axinte et al., 2010]).

Assuming that the etching rate depends only on the radial position r within the jet, (2.2) becomes ([Ghobeity et al., 2008],[Axinte et al., 2010]):

$$\frac{\partial z}{\partial t} = -E(r) \cos^k \theta. \quad (2.4)$$

Finally, the erosion power of the jet decreases with the stand-off distance of the jet ([Axinte et al., 2010]). When the surface can be described by the depth $z \leq 0$, an exponential fading will be considered in this thesis:

$$\frac{\partial z}{\partial t} = -E(r) \exp(az) \cos^k \theta, \quad (2.5)$$

where $a > 0$ is an unknown parameter.

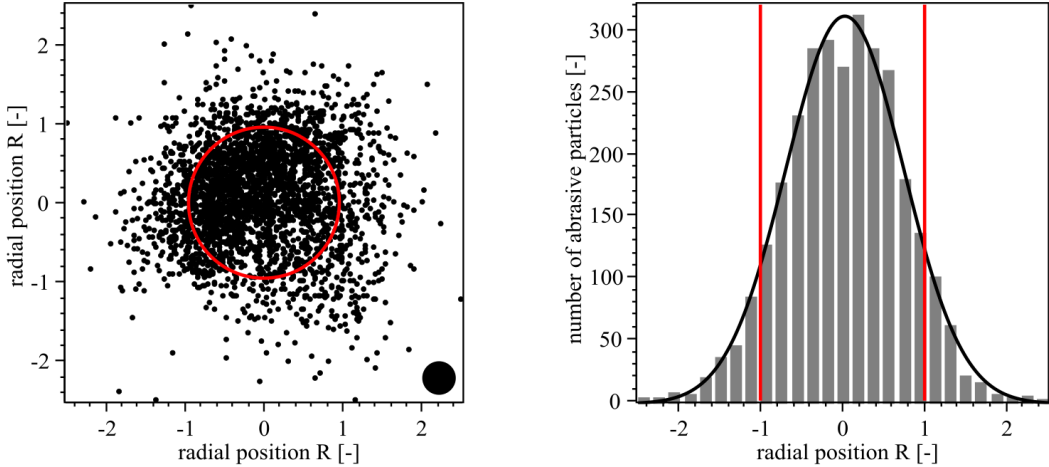


Figure 2.3 – Experimental scatterplot (on the left) and the histogram of the abrasive particles distribution within the jet (from [Balz and Heiniger, 2011])

2.2 General approach to the calibration problem

The impact angle of the jet is given by an angle between jet symmetry axis and a tangent to the surface. We consider a case when the jet impacts an initially flat surface $Z(x, y) = 0$ at 90° impact angle, as figure 2.2 shows schematically. Based on (2.5), the evolution of this surface can be described by the system (2.6).

$$\begin{cases} \frac{\partial Z}{\partial t} = -\frac{E(r) \exp(aZ)}{\left(1 + \left(\frac{\partial Z}{\partial x}\right)^2 + \left(\frac{\partial Z}{\partial y}\right)^2\right)^{\frac{k}{2}}}, \\ Z(x, y, 0) = 0, \end{cases} \quad (2.6)$$

where r is a distance from the point (x, y) to the jet axis.

Model (2.6) contains a set of unknown parameters that should be calibrated from the experiment. A scalar parameter a takes into account a stand-off distance between the jet head and the processed surface. The expression

$1/\sqrt{1 + (\partial Z/\partial x)^2 + (\partial Z/\partial y)^2}$ is equal to the cosine of the local angle θ between the jet and the normal \vec{n} to the machined surface. Therefore, a scalar parameter k comes from the cosine law of the erosion for brittle materials [Slikkerveer et al., 1999]. Finally, an unknown function E is called the etching rate function. It describes specific material erosion rate depending on the distance from the jet axis. The erosion rate function is a positive function that attains its maximal value in the center of the jet and then decreases to zero on the distance equal to the radius of

the jet.

In [Axinte et al., 2010, Kong et al., 2012a, Billingham et al., 2013] the etching rate function has been calibrated by linearization of (2.6) for the case when the slopes $\partial Z / \partial x, \partial Z / \partial y$ remain small during the processing. This assumption allows to simplify the PDE in (2.6) to the form $\frac{\partial Z}{\partial t} = -E(r)$ and then to retrieve the etching rate function in the form of an integral. In case of the milling of the crater, this assumption would imply that the crater replicates the form of the etching rate function. The considered experimental setup corresponded to the milling of a trench, that has complicated the calibration.

The goal of the present work is to develop an approach that allows simultaneous calibration of all parameters of the model without any simplification of the problem (2.6). The cost function J was introduced to describe the discrepancy between the experiment and the result of the numerical solution of the direct problem (2.6):

$$J(k, a, E) = \|Z(x, y, T) - Z_{exp}\|^2.$$

Here $Z(x, y, T)$ is obtained as a solution of the direct problem (2.6) at a final time $t = T$ for a particular experimental setup. Z_{exp} is the experimental data corresponding to this setup. The minimization of the cost function leads to the PDE constrained optimization problem. This problem can be treated by methods described in Sections 1.2 and 1.3.

Chapter 3 considers a stationary jet that impacts a surface and rests on the same spot from initial time $t = 0$ up to the final time $t = T$. The milled surface represents a crater. For this case the adjoint approach was applied to the calibration problem.

Chapter 4 deals with a situation when the jet moves with a constant feed speed v along a line path, as 2.4 shows. Axis Oy is chosen to be aligned with the direction of the jet movement.

PDE constrained optimization for this case was carried out both by means of the adjoint approach and the automatic differentiation approach.

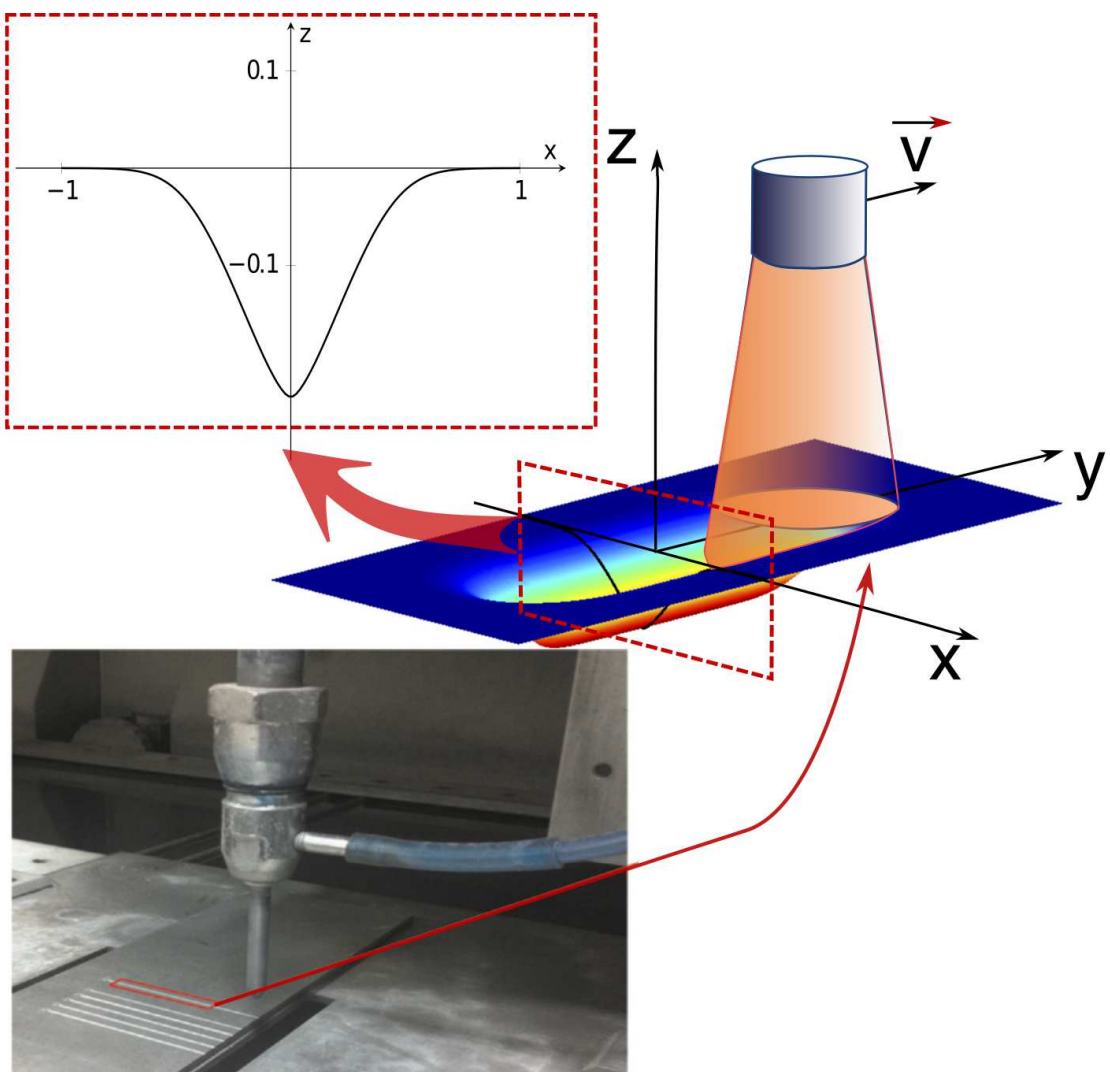


Figure 2.4 – Schematic model of the trench milling by moving waterjet.

Chapter 3

Stationary Abrasive Waterjet

In this chapter we consider the limiting case of a stationary jet, that is, the case with a jet feed speed $v = 0$. The milled surface represents a crater. The waterjet jet of a short duration with stable characteristics is hard to obtain in practice, so the reliable experimental data for the calibration are not available. This happens because when the abrasive waterjet machine starts to work, the physical characteristic of the process, such as the water pump pressure and the abrasives mass flow, do not attain their constant values instant. Nevertheless, further consideration of the case $v = 0$ will clarify the approach to the general calibration problem. In this section we will consider only the etching rate function E as a calibration parameter. The parameters a and k will be treated as known constants. Motivation for that is a mere reduction of the length of formulas.

When the jet does not move the problem has a radial symmetry. Figure 3.1 gives a schematic representation of the milling process, with a jet footprint Z depending only on x .

The evolution of the cross-section of the crater, obtained by such etching process is described by (3.1).

$$\begin{cases} \frac{\partial Z}{\partial t} = -\frac{E(|x|) \exp aZ}{\left(1 + \left(\frac{\partial Z}{\partial x}\right)^2\right)^{\frac{k}{2}}}, \\ Z(x, 0) = 0. \end{cases} \quad (3.1)$$

This problem is dimensionless, and the return to the dimensional space coordinates is given by the following relations: $x^d = Rx$, $z^d = Rz$. Here R is the radius of the jet, and a superscript 'd' stands for a dimensional value. This implies that in (3.1) $x \in [-1, 1]$.

Suppose that an experimental cross section profile Z_{exp} is available after milling

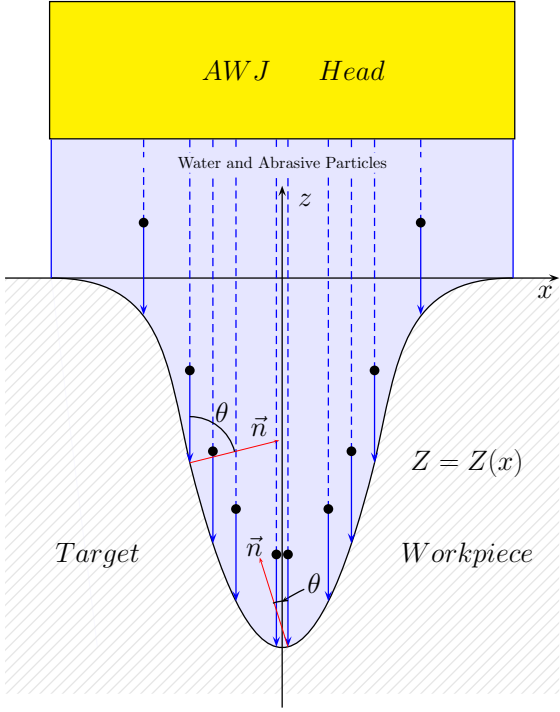


Figure 3.1 – Schematic representation of the cross-section of the waterjet footprint for a stationary jet.

process stopped at time $t = T$. We introduce a cost function:

$$J(E) = \frac{1}{2} \int_{-1}^1 (Z(x, T) - Z_{exp}(x))^2 dx + \frac{\alpha}{2} \int_{-1}^1 |\nabla E(x)|^2 dx, \quad (3.2)$$

where α is a regularization coefficient. The first integral in (3.2) describes the discrepancy between the solution of the direct problem (3.1) $Z(x, T)$ and the experimental data Z_{exp} . The second integral is responsible for the regularization. We use the a priori knowledge about the smoothness of the etching rate function for the construction of the second term in (3.2). This term plays a regularization role, its presence assures that the oscillating solution for $E(x)$ would be cast out during the optimization process. When the parameters a and k are fixed, the identification problem for E can be written as an optimization problem:

Problem 1. Find the positive function E^* such that

$$J(E^*) = \inf_E J(E), \quad (3.3)$$

under the constraint that Z is the output of the model (3.1) with the input E .

3.1 Application of the continuous adjoint approach

Problem 1 is an example of a PDE-constrained optimization problem. Following the discussed in Section 1.2.2 Lagrangian approach [Lions, 1971, Hinze et al., 2009, Rees et al., 2010], the corresponding Lagrangian can be written:

$$L(E, Z, P) = J(E) + \int_0^T \int_{-1}^1 P(x, t) \left(\frac{\partial Z}{\partial t} - G(Z, Z_x, E) \right) dx dt, \quad (3.4)$$

where P is the Lagrange multiplier, associated to the constraint that Z is an output of (3.1). G is a function that describes right hand side of the PDE (3.1), that is $G(Z, Z_x, E) = -E \exp aZ / (1 + (Z_x)^2)^{\frac{k}{2}}$.

All variational partial derivatives [Gelfand and Fomin, 1963, Lions, 1971] of the Lagrangian should be equal to zero at the point of minimum of $J(E)$. The derivative of L with respect to the Lagrange multiplier P gives just the PDE that governs the direct problem (3.1).

Let us consider the derivative of L with respect to Z . Integration by parts gives us:

$$\begin{aligned} L(E, Z, P) = & J(E, Z) - \int_0^T \int_{-1}^1 \frac{\partial P}{\partial t} \cdot Z dt dx - \\ & - \int_0^T \int_{-1}^1 P(x, t) G(Z, Z_x, u) dt dx + \int_{-1}^1 P(x, T) Z(x, T) dx - \\ & - \int_{-1}^1 P(x, 0) Z(x, 0) dx \end{aligned}$$

For the cost function we have:

$$J(E, Z + \epsilon Y) - J(E, Z) = \int_{-1}^1 \epsilon Y(x, T) (Z(x, T) - Z_{exp}(x)) dx$$

The admissible variations $Y(x, t)$ satisfy $Y(x = -1, t) = Y(x = 1, t) = 0$, because there is no etching on the crater edges and $Z(x = -1) = Z(x = 1) = 0$.

We obtain the following result for the variation of the Lagrangian:

$$\begin{aligned}
L(E, Z + \epsilon Y, P) - L(E, Z, P) &= \\
&= J(E, Z + \epsilon Y) - J(E, Z) - \epsilon \int_0^T \int_{-1}^1 \frac{\partial P(x, t)}{\partial t} \cdot Y(x, t) dt dx - \\
&\quad - \int_0^T \int_{-1}^1 P(x, t) [G(Z + \epsilon Y, Z_x + \epsilon Y_x, u) - G(Z, Z_x, u)] dt dx + \\
&\quad + \int_{-1}^1 P(x, T) \epsilon Y(x, T) dx - \underbrace{\int_{-1}^1 P(x, 0) \epsilon Y(x, 0) dx}_{=0, \text{ because } Y(x, 0)=0} = \\
&= \int_{-1}^1 \epsilon Y(x, T) (Z(x, T) - Z_{exp}(x)) dx - \epsilon \int_0^T \int_{-1}^1 \frac{\partial P(x, t)}{\partial t} Y(x, t) dt dx - \\
&\quad - \int_0^T \int_{-1}^1 P(x, t) G_Z(Z, Z_x, E) \epsilon Y(x, t) dt dx - \\
&\quad - \int_0^T \int_{-1}^1 P(x, t) G_{Z_x}(Z, Z_x, E) \epsilon Y_x dt dx + \int_{-1}^1 P(x, T) \epsilon Y(x, T) dx = \\
&= \int_{-1}^1 \epsilon Y(x, T) (Z(x, T) - Z_{exp}(x)) dx - \epsilon \int_0^T \int_{-1}^1 \frac{\partial P(x, t)}{\partial t} Y(x, t) dt dx - \\
&\quad - \int_0^T \int_{-1}^1 P(x, t) G_Z(Z, Z_x, E) \epsilon Y(x, t) dt dx + \\
&\quad + \int_0^T \int_{-1}^1 \epsilon Y(x, t) \frac{\partial}{\partial x} [P(x, t) G_{Z_x}(Z, Z_x, E)] dt dx - \\
&\quad - \underbrace{\int_0^T (P(x, t) G_{Z_x}(Z, Z_x, E) \epsilon Y(x, t))|_{x=1} dt}_{=0, \text{ because } Y(x, t)|_{x=1}=0} + \\
&\quad + \underbrace{\int_0^T (P(x, t) G_{Z_x}(Z, Z_x, E) \epsilon Y(x, t))|_{x=-1} dt}_{=0, \text{ because } Y(x, t)|_{x=-1}=0} + \int_{-1}^1 P(x, T) \epsilon Y(x, T) dx
\end{aligned}$$

Thus, the condition of nulling of the derivative of L with respect to Z leads to

the following adjoint problem:

$$\begin{cases} -\frac{\partial P(x, t)}{\partial t} = \left(\frac{\partial G}{\partial Z}\right) P(x, t) - \left(\frac{\partial G}{\partial Z_x}\right) \frac{\partial P}{\partial x} - \left(\frac{\partial}{\partial x} \frac{\partial G}{\partial Z_x}\right) P(x, t) \\ P(x, T) = Z_{exp}(x) - Z(x, T); \\ P(-1, t) = 0; \\ P(1, t) = 0. \end{cases} \quad (3.5)$$

The key point of the consideration of the derivative of L with respect to E is that this derivative is equal to the gradient of the cost function when Z is a solution of the direct problem (3.1). This leads to the following expression for the variational derivative of the cost function:

$$\frac{\partial J}{\partial E(x)} = \frac{\partial L}{\partial E(x)} = - \int_0^T P(x, t) \frac{\partial G}{\partial E}(x, t) dt - \alpha \nabla^2 E(x). \quad (3.6)$$

3.2 Application of the discrete adjoint approach

As was discussed in Section 1.2, there is a pitfall with a direct application of the obtained results to the optimization problem (Problem 1). The continuous direct problem (3.1) and the continuous adjoint problem (3.5) can be solved only numerically, so they have to be discretized. But the operations of discretization and taking of the adjoint are not commutative. It means that the gradient of the cost function should be computed via the adjoint to the discrete direct problem, and not via the discretization of the continuous adjoint problem.

3.2.1 Derivation of the adjoint problem

For the case of a stationary jet the discrete adjoint problem was derived explicitly from the discretized direct problem and the discrete version of the cost function (3.2).

Following the standard approach [LeVeque, 2002], the interval $\{x \in \mathbb{R} \mid -1 \leq x \leq 1\}$ was discretized into a collection of M equally spaced grid points $\{x_m = -1 + (m - 1)h, m = \overline{1, M}\}$ with a step $h = 2/(M - 1)$. Time coordinate was discretized with a step Δt from the starting time $t = 0$ up to the final time $t = T$ into a set $\{t_n = (n - 1)\Delta t, n = \overline{1, N + 1}\}$. With the introduction of the following notations

$D^{-x}Z_{m,n} = \frac{Z_{m,n} - Z_{m-1,n}}{h}$, $D^{+x}Z_{m,n} = \frac{Z_{m+1,n} - Z_{m,n}}{h}$, the upwind numerical scheme for the direct problem (3.1) is given by (3.7).

$$\begin{aligned} \frac{Z_{m,n+1} - Z_{m,n}}{\Delta t} - \frac{E_m e^{aZ_{m,n}}}{(1 + D^{-x}Z_{m,n})^{\frac{k}{2}}} &= 0, \quad \text{for } x_m < 0 \\ \frac{Z_{m,n+1} - Z_{m,n}}{\Delta t} - \frac{E_m e^{aZ_{m,n}}}{(1 + D^{+x}Z_{m,n})^{\frac{k}{2}}} &= 0, \quad \text{for } x_m > 0, \end{aligned} \quad (3.7)$$

where $\{E_m = E(|x_m|), m = \overline{1, M}\}$ is a set of values of the etching rate function on the space grid. The problem of calibration of the etching rate function becomes that of finding $\{E_m\}$. The system (3.7) is completed by the initial condition $Z_{m,1} = 0$, for $m = \overline{1, M}$ and boundary conditions $Z_{1,n} = Z_{M,n} = 0$, for $n = \overline{1, N + 1}$.

In these notations the discrete analogy of the cost function is given by (3.8):

$$J(\{E_m\}) = \frac{1}{2} \sum_{m=1}^M (Z_{m,N+1} - Z_m^{exp})^2 + \frac{\alpha}{2} \sum_{m=2}^{M-1} \left(\frac{E_{m+1} - E_{m-1}}{2h} \right)^2 \quad (3.8)$$

where $\{Z_{m,N+1}\}$ is the solution of the direct problem (3.7) at the final time. We used the central difference scheme for the approximation of the derivative of the etching rate function in the Tikhonov regularization term in (3.8).

Discrete analogy of the Lagrangian (3.4) is obtained by passing from the integration to the summation and by taking a discrete numerical scheme in place of the equation governing direct problem.

$$\begin{aligned}
 L(\{E_m\}, \{Z_{m,n}\}, \{P_{m,n}\}) = & \\
 = & \frac{1}{2} \sum_{m=1}^M (Z_{m,N+1} - Z_m^{exp})^2 + \frac{\alpha}{2} \sum_{m=2}^{M-1} \left(\frac{E_{m+1} - E_{m-1}}{2h} \right)^2 + \\
 & + \sum_{m=1}^{M/2} \sum_{n=1}^{N+1} P_{m,n} \left(\frac{Z_{m,n+1} - Z_{m,n}}{\Delta t} - \frac{E(|x_m|) e^{aZ_{m,n}}}{(1 + D^{-x} Z_{m,n})^{\frac{k}{2}}} \right) + \\
 & + \sum_{m=1}^{M/2} \sum_{n=1}^{N+1} P_{m,n} \left(\frac{Z_{m,n+1} - Z_{m,n}}{\Delta t} - \frac{E(|x_m|) e^{aZ_{m,n}}}{(1 + D^{+x} Z_{m,n})^{\frac{k}{2}}} \right)
 \end{aligned} \tag{3.9}$$

As before, the variation of this discrete Lagrangian with respect to the adjoint $P_{m,n}$ leads to the discretized version of the direct problem (3.7).

The variation ϵY of the crater profile Z leads to the following variation of the cost function:

$$J(E, Z + \epsilon Y) - J(E, Z) = \sum_{m=1}^M h (Z_{m,N} - Z_{exp}^m) \epsilon Y_{m,N}$$

The corresponding variation to ϵY of the last two terms of discrete Lagrangian

gives:

$$\begin{aligned}
& h\Delta t \left\{ \sum_{n=1}^N \sum_{m=2}^{M/2} \epsilon P_{m,n} \left(\frac{Y_{m,n+1} - Y_{m,n}}{\Delta t} + \frac{aE(x_m)e^{aZ_{m,n}} Y_{m,n}}{\left(1 + \left(\frac{Z_{m,n} - Z_{m-1,n}}{h}\right)^2\right)^{k/2}} - \right. \right. \\
& \quad - \frac{kE(x_m)e^{aZ_{m,n}}}{\left(1 + \left(\frac{Z_{m,n} - Z_{m-1,n}}{h}\right)^2\right)^{k/2+1}} \frac{Z_{m,n} - Z_{m-1,n}}{h} \frac{Y_{m,n} - Y_{m-1,n}}{h} + \left. \right) \\
& \quad + \sum_{n=1}^N \sum_{m=2}^{M/2} \epsilon P_{m,n} \left(\frac{Y_{m,n+1} - Y_{m,n}}{\Delta t} + \frac{aE(x_m)e^{aZ_{m,n}} Y_{m,n}}{\left(1 + \left(\frac{Z_{m+1,n} - Z_{m,n}}{h}\right)^2\right)^{k/2}} - \right. \\
& \quad \left. \left. - \frac{kE(x_m)e^{aZ_{m,n}}}{\left(1 + \left(\frac{Z_{m+1,n} - Z_{m,n}}{h}\right)^2\right)^{k/2+1}} \frac{Z_{m+1,n} - Z_{m,n}}{h} \frac{Y_{m+1,n} - Y_{m,n}}{h} + \right) \right\}
\end{aligned}$$

Change of summation in previous expression (discrete analogy of the integration by parts in the continuous case, the goal is to have common multiplier $Y_{m,n}$

in the sum) results in:

$$\begin{aligned}
& h\Delta t \left\{ \sum_{n=2}^{N+1} \sum_{m=2}^{M-1} \epsilon P_{m,n-1} \frac{Y_{m,n}}{\Delta t} - \sum_{n=1}^N \sum_{m=2}^{M-1} \epsilon P_{m,n} \frac{Y_{m,n}}{\Delta t} + \right. \\
& + \sum_{n=1}^N \sum_{m=2}^{M/2} \epsilon P_{m,n} \frac{aE_m e^{aZ_{m,n}}}{\left(1 + \left(\frac{Z_{m,n} - Z_{m-1,n}}{h}\right)^2\right)^{k/2}} Y_{m,n} - \\
& - \sum_{n=1}^N \sum_{m=2}^{M/2} \epsilon P_{m,n} \frac{kE_m e^{aZ_{m,n}}}{\left(1 + \left(\frac{Z_{m,n} - Z_{m-1,n}}{h}\right)^2\right)^{k/2+1}} \frac{Z_{m,n} - Z_{m-1,n}}{h} \frac{Y_{m,n}}{h} + \\
& + \sum_{n=1}^N \sum_{m=1}^{M/2-1} \epsilon P_{m+1,n} \frac{kE_{m+1} e^{aZ_{m+1,n}}}{\left(1 + \left(\frac{Z_{m+1,n} - Z_{m,n}}{h}\right)^2\right)^{k/2+1}} \frac{Z_{m+1,n} - Z_{m,n}}{h} \frac{Y_{m,n}}{h} + \\
& + \sum_{n=1}^N \sum_{m=M/2+1}^{M-1} \epsilon P_{m,n} \frac{aE_m e^{aZ_{m,n}}}{\left(1 + \left(\frac{Z_{m+1,n} - Z_{m,n}}{h}\right)^2\right)^{k/2}} Y_{m,n} - \\
& - \sum_{n=1}^N \sum_{m=M/2+1}^{M-1} \epsilon P_{m-1,n} \frac{kE_{m-1} e^{aZ_{m-1,n}}}{\left(1 + \left(\frac{Z_{m,n} - Z_{m-1,n}}{h}\right)^2\right)^{k/2+1}} \frac{Z_{m,n} - Z_{m-1,n}}{h} \frac{Y_{m,n}}{h} + \\
& \left. + \sum_{n=1}^N \sum_{m=1}^{M/2-1} \epsilon P_{m,n} \frac{kE_m e^{aZ_{m,n}}}{\left(1 + \left(\frac{Z_{m+1,n} - Z_{m,n}}{h}\right)^2\right)^{k/2+1}} \frac{Z_{m+1,n} - Z_{m,n}}{h} \frac{Y_{m,n}}{h} \right\}
\end{aligned}$$

Combining, the variation with respect to the crater profile $Z_{m,n}$ gives a discrete adjoint problem (3.10),(3.11).

For $n = 2 \dots N$, $m = 2 \dots M/2 - 1$

$$\begin{aligned} \frac{P_{m,n-1} - P_{m,n}}{\Delta t} + \frac{aE(x_m) \exp(aZ_{m,n})}{(1 + (D^{-x}Z_{m,n})^2)^{\frac{k}{2}}} P_{m,n} - \\ - \frac{kE(x_m) \exp(aZ_{m,n})}{(1 + (D^{-x}Z_{m,n})^2)^{\frac{k}{2}-1}} D^{-x} Z_{m,n} \frac{P_{m,n}}{h} + \\ + \frac{kE(x_{m+1}) \exp(aZ_{m+1,n})}{(1 + (D^{+x}Z_{m,n})^2)^{\frac{k}{2}-1}} D^{+x} Z_{m,n} \frac{P_{m+1,n}}{h} + \\ + \delta_{n,N} \sum_{j=1}^M (Z_{j,N} - Z_{exp}(x_j)) = 0 \end{aligned} \quad (3.10)$$

where $\delta_{n,N}$ is the Kronecker's delta.

For $n = 2 \dots N$, $m = M/2$

$$\begin{aligned} \frac{P_{M/2,n-1} - P_{M/2,n}}{\Delta t} + \frac{aE(x_{M/2}) \exp(aZ_{M/2,n})}{(1 + (D^{-x}Z_{n,M/2})^2)^{\frac{k}{2}}} P_{n,M/2} - \\ - \frac{kE(x_{M/2}) \exp(aZ_{M/2,n})}{(1 + (D^{-x}Z_{M/2,n})^2)^{\frac{k}{2}-1}} D^{-x} Z_{M/2,n} \frac{P_{n,M/2}}{h} + \\ + \delta_{n,N} \sum_{j=1}^M (Z_{N,j} - Z_{exp}(x_j)) = 0 \end{aligned} \quad (3.11)$$

The adjoint to the discrete direct problem on the right half of the mesh, i.e. $m = M/2 + 1 \dots M$, is described by the equations analogous to (3.10),(3.11).

This numerical scheme for P is completed with a condition on the final time T and the boundary conditions in $x = x_1 = -1$ and $x = x_M = 1$:

$$\begin{aligned} P(x_m, t_N) = 0 & \text{ for } m = \overline{1, M/2} \\ P(x_1, t_n) = 0 & \text{ for } n = \overline{1, N} \end{aligned}$$

When the discrete direct and adjoint problems are solved numerically, the gradient of the cost function with respect to M unknown parameters

$\{E_m, m = \overline{1, M}\}$ is obtained from the following discrete analogue of (3.6):

$$\begin{aligned} \frac{\partial J}{\partial E_m} &= h \sum_{n=1}^N \Delta t P_{n,m} \frac{\exp(aZ_{n,m})}{(1 + (D^{-x} Z_{n,m})^2)^{\frac{k}{2}}} + \alpha (D^{-x} E_m - D^{+x} E_m), \\ &\quad m = \overline{2, M/2}; \\ \frac{\partial J}{\partial E_m} &= h \sum_{n=1}^N \Delta t P_{n,m} \frac{\exp(aZ_{n,m})}{(1 + (D^{+x} Z_{n,m})^2)^{\frac{k}{2}}} + \alpha (D^{-x} E_m - D^{+x} E_m), \\ &\quad m = \overline{M/2 + 1, M - 1}. \end{aligned} \quad (3.12)$$

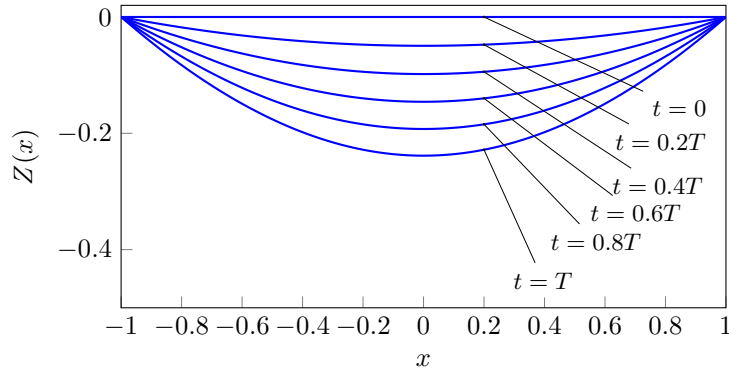


Figure 3.2 – Calculated cross-sections that correspond to the first guess of the etching rate function E_0 .

3.2.2 Calibration of the etching rate function

Once the calculation procedure of the gradient of the cost function is available, a descent type algorithm (Section 1.1) can be applied to the minimization problem (Problem 1). In addition, the number of calibration parameters was reduced to $\{E_m, m = \overline{1, M/2}\}$ when the experimental data Z_{exp} is symmetrized, and only left half of the grid was used in the calibration procedure.

Figure 3.2 presents the evolution of the cross-section of the crater, calculated from (3.1) with an initial guess of the etching rate function E_0 (figure 3.5). All values $Z_{m,n}, m = \overline{1, M}, n = \overline{1, N}$ are saved and then used to solve the discrete adjoint problem. $Z_{m,N}, m = \overline{1, M}$ are used for computing the value of the cost function J .

The result of simulation of the direct problem (3.1) was used as the experimental data $Z_{exp}(x)$. In this simulation a function \tilde{E} (figure 3.5) was chosen as etching rate function. Evolution of the cross-section that corresponds to \tilde{E} is represented in figure 3.3 by dashed lines. The profile that corresponds to $t = T$ was chosen as the experimental data Z_{exp} for the calibration procedure.

Figure 3.4 shows the behaviour of the adjoint state $P_{m,n}, m = \overline{1, M}, n = \overline{1, N}$ that corresponds to $Z_{m,n}$ end Z_{exp} described above.

Substitution of $Z_{m,n}, P_{m,n}, m = \overline{1, M}, n = \overline{1, N}$ and Z_{exp} in (3.12) gives the gradient of the cost function.

Computing the values of the cost function (3.8) and of its gradient enables minimization in **Problem 1**. The developed procedure was implemented in MATLAB. The build-in *fminunc* solver with *quasi-newton* algorithm was used for the minimization. At each minimization step the gradient was calculated for the corresponding updated value of E in the same way as for E_0 . The minimization stopped when the size of the cost function or the norm of its gradient was less

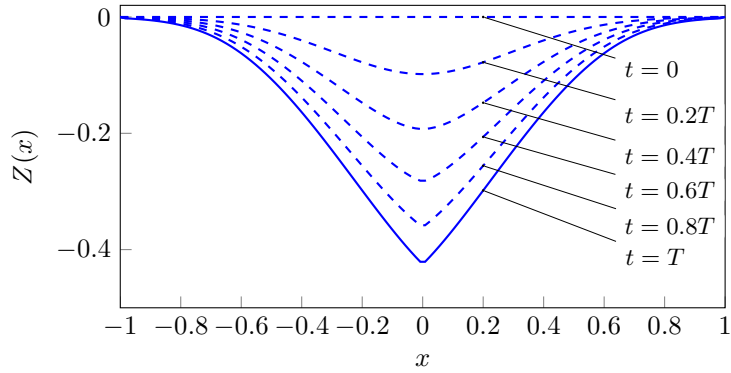


Figure 3.3 – Calculated cross-sections that correspond to the \tilde{E} . Profile at $t = T$ gives the experimental data Z_{exp} in the calibration procedure.

than the value 10^{-12} . The calibration took approximately 10sec (840 iterations of the *fminunc* solver) on a 2.8GHz Intel Core i7 with 16GB of RAM for the choice $M = 126$ and a dwell time $T = 0.5$ with $dt = 0.01$. The numerical value of the regularization parameter α was chosen by the numerical experimentation based on *L*-curve regularization parameter selection method ([Hansen and O’Leary, 1993], [Hansen, 1999]). The optimal value $\alpha = 10^{-9}$ allowed to avoid the oscillations in the solution without over-smoothing it.

Figure 3.5 shows that the etching rate function \tilde{E} was retrieved from the generated experimental data with high accuracy. This accuracy was estimated by ε (3.13).

$$\varepsilon = \frac{\sqrt{\frac{1}{2} \int_{-1}^1 (E^*(x) - \tilde{E}(x))^2 dx}}{\sqrt{\frac{1}{2} \int_{-1}^1 \tilde{E}^2(x) dx}} \quad (3.13)$$

For the given in figure 3.5 example of the calibration $\varepsilon = 0.2\%$.

To summarize, we developed a procedure for the calibration of the etching rate function. We considered the experimental setup of the crater milling. Calibration is based on the minimization of the difference between the numerically simulated profile of the crater and the experimental data. This minimization problem is an example of the PDE constrained optimization, and it was solved by the adjoint approach. The developed calibration procedure allows to calibrate the simulated experimental data with high accuracy.

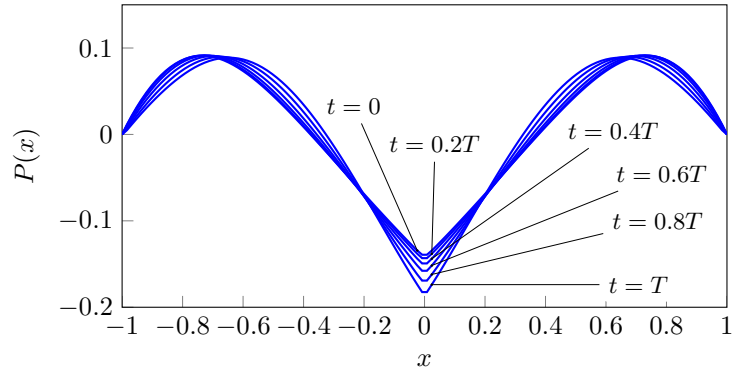


Figure 3.4 – Evolution of the adjoint state that corresponds to Z_{exp} and the initial guess of the etching rate function E_0 .

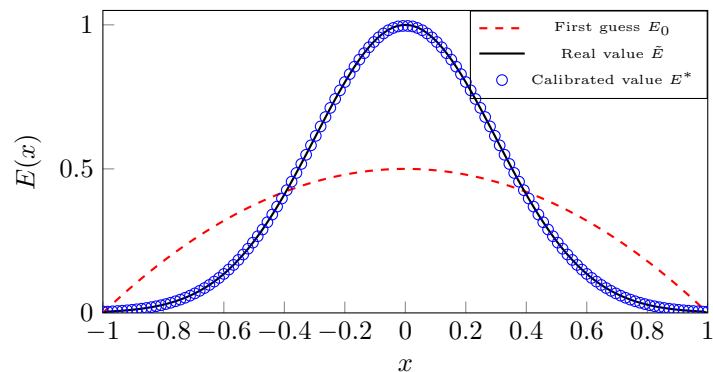


Figure 3.5 – The etching rate functions: \tilde{E} , used for simulation of the experimental data; E_0 , a first guess in minimization procedure; E^* , a result of the calibration.

Chapter 4

Moving Abrasive Waterjet

In this chapter we consider an abrasive waterjet that impacts a target surface perpendicularly and moves along a straight pass with a feed speed v . Figure 4.1 illustrates such experimental setup and shows the choice of the coordinate system.

When the waterjet moves along a straight line, the geometry of a milled surface represents a trench. Far enough from start and end points of the jet path, this trench is described by its cross section $Z(x, t)$ for times t after the jet passage. The available experimental data describe the average trench profile $Z_{exp}(x)$. Such experimental data are reliable in comparison with the crater shape in the case of the stationary jet, $v = 0$. This fact is due to the possibility to neglect the shape of the milled surface in the beginning of the process, that is near the starting point of the trench.

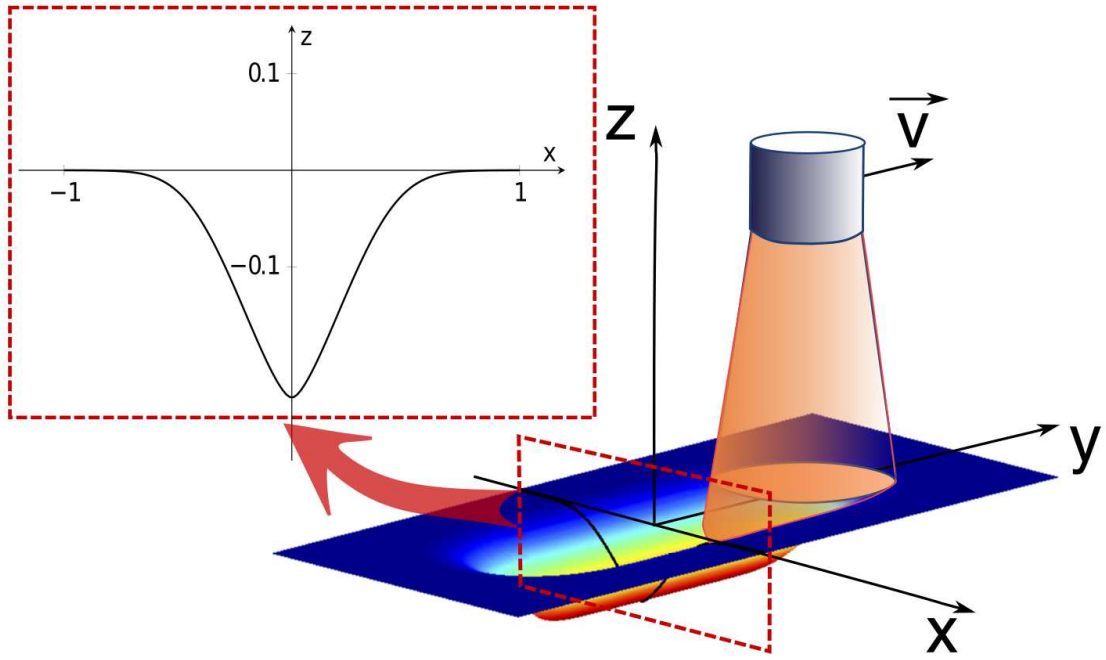


Figure 4.1 – Schematic model of the trench milling by moving waterjet.

4.1 Geometrical model for moving abrasive water-jet

In Section 2.1 the variable in the PDE equation that describes the evolution of the milled surface are dimensional variables. Let us remind this PDE (2.5) with a slight alternation - a superscript 'd' that signals that corresponding variable is dimensional:

$$\frac{\partial z^d}{\partial t^d} = -E^d(r^d) \exp(a^d z^d) \cos^k \theta, \quad (4.1)$$

In the local geometry $\cos \theta = 1 / \sqrt{\left(1 + \left(\frac{\partial z^d}{\partial x^d}\right)^2 + \left(\frac{\partial z^d}{\partial y^d}\right)^2\right)}$. But dependence on y can be removed, by taking into account $y^d = v^d t^d$ for the cross-section under consideration. Following [Axinte et al., 2010], the evolution of the cross-

section of the trench is described by the dimensionless system (4.2):

$$\begin{cases} \frac{\partial Z}{\partial t} = \begin{cases} -\frac{E(\sqrt{x^2 + t^2}) \exp(aZ)}{\left(1 + \left(\frac{\partial Z}{\partial x}\right)^2 + \left(\frac{\partial Z}{\partial t}\right)^2\right)^{\frac{k}{2}}}, & \text{for } -\sqrt{1-x^2} \leq t \leq \sqrt{1-x^2}; \\ 0, & \text{for } -1 \leq t \leq -\sqrt{1-x^2} \text{ and } \sqrt{1-x^2} \leq t \leq 1; \end{cases} \\ Z(x, 0) = 0. \end{cases} \quad (4.2)$$

Return to the dimensional physical quantities is given by the following relations: $x^d = Rx$, $z^d = RZ$, $t^d = (R/v)t$, $E^d = vE$, $y^d = vt^d = Rt$. Here R is the radius of the jet, v is the jet speed in y -direction, and a superscript 'd' stands for a dimensional value as before. While moving, the abrasive waterjet influences the profile of the cross-section $Z(x, t)$ for the first time at $t = -1$ and for the last time at $t = 1$.

In [Axinte et al., 2010],[Kong et al., 2012a] the etching rate function was calibrated for the linearized direct problem (4.2), that is under the assumption of a shallow trench.

In (4.2) $u = \{E, k, a\}$ is the set of unknown parameters of the model. The goal of this chapter is to calibrate these parameters from a real experiment at the same time and without any additional assumptions on the model. The available experimental data Z_{exp} correspond to the averaged trench profile along jet feed speed \vec{v} direction. In analogy with the previous section, we introduce a cost function (4.3).

$$J(u) = \frac{1}{2} \int_{-1}^1 (Z(x, t=1) - Z_{exp}(x))^2 dx + \frac{\alpha}{2} \int_{-1}^1 |\nabla E(x)|^2 dx \quad (4.3)$$

Minimization of the difference between the experiment and the results of modelling leads to the **Problem 6.3**.

Problem 2. Find a set of parameters $u^* = \{E^*, k^*, a^*\}$ such that

$$J(u^*) = \inf_u J(u), \quad (4.4)$$

under the constraint that Z is the output of the model (4.2) with the input u and E^* is a positive function.

4.2 Moving abrasive waterjet. Adjoint approach

In the slightly changed notations, the evolution of the trench cross-section is described by (4.5).

$$\begin{cases} \frac{\partial Z}{\partial t} = F(Z, Z_x, Z_t, u); \\ Z(x, 0) = 0. \end{cases} \quad (4.5)$$

with $F(Z, Z_x, Z_t, u) = -\frac{E(\sqrt{x^2 + t^2}) \exp(aZ)}{\left(1 + \left(\frac{\partial Z}{\partial x}\right)^2 + \left(\frac{\partial Z}{\partial t}\right)^2\right)^{\frac{k}{2}}}\chi(x, t)$, where
 $\chi = \begin{cases} 1, & \text{for } -\sqrt{1-x^2} \leq t \leq \sqrt{1-x^2}; \\ 0, & \text{for } -1 \leq t \leq -\sqrt{1-x^2} \text{ and } \sqrt{1-x^2} \leq t \leq 1. \end{cases}$

Following the adjoint approach (Section 1.2), (4.6) defines the Lagrangian associated to problem of cost function minimization, Problem 6.3.

$$L(u, Z, P) = J(u, Z) + \int_{-1}^1 \int_{\Omega} P(x, t) \left(\frac{\partial Z}{\partial t} - G(Z, Z_x, E) \right) dx dt, \quad (4.6)$$

where P is the Lagrange multiplier, associated to the constraint that Z is a solution of the direct problem (4.5) and $\Omega = [-1, 1]$ - the domain of definition of x .

The condition of nulling of the derivative of L with respect to Z leads to the following continuous adjoint problem:

$$\begin{cases} -\frac{\partial P(x, t)}{\partial t} = \left(\frac{\partial F}{\partial Z}\right) P(x, t) - \frac{\partial}{\partial x} \left(P \frac{\partial G}{\partial Z_x}\right) - \frac{\partial}{\partial t} \left(P \frac{\partial G}{\partial Z_t}\right) \\ P(x, t = 1) = Z_{exp}(x) - Z(x, t = 1); \\ P(-1, t) = 0; \\ P(1, t) = 0. \end{cases} \quad (4.7)$$

Let $Z(x, t)$ be a solution of direct problem that correspond to a particular choice of parameters k, a, E . Then the gradient of the cost function J (4.3) at k, a, E is given by (4.8), (4.9), (4.10).

$$\frac{\partial J}{\partial k} = \frac{\partial L}{\partial k} = - \int_{-1}^1 P(x, t) \frac{\partial G}{\partial k} dt, \quad (4.8)$$

$$\frac{\partial J}{\partial a} = \frac{\partial L}{\partial a} = - \int_{-1}^1 P(x, t) \frac{\partial G}{\partial a} dt, \quad (4.9)$$

$$\frac{\partial J}{\partial E(x)} = \frac{\partial L}{\partial E(x)} = - \int_{-1}^1 P(x, t) \frac{\partial G}{\partial E}(x, t) dt - \alpha \Delta E(x). \quad (4.10)$$

The direct problem (4.5) can be solved only numerically. So, just in the same way as before for the stationary AWJ (Section 3.2), the adjoint problem should be derived from the discrete direct problem. Discretized version of the cost function (4.3) is:

$$J(k, a, \{E_m\}) = \frac{1}{2} \sum_{m=1}^M h (Z_{m,N+1} - Z_m^{exp})^2 + \frac{\alpha}{2} \sum_{m=2}^{M-1} h \left(\frac{E_{m+1} - E_{m-1}}{2h} \right)^2 \quad (4.11)$$

Then the discretized version of the Lagrangian is:

$$\begin{aligned} L(k, a, \{E_m\}, \{Z_{m,n}\}, \{P_{m,n}\}) &= \\ &= \frac{1}{2} \sum_{m=1}^M h (Z_{m,N} - Z_m^{exp})^2 + \frac{\alpha}{2} \sum_{m=2}^{M-1} h \left(\frac{E_{m+1} - E_{m-1}}{2h} \right)^2 + \\ &+ \sum_{m=1}^M \sum_{n=1}^{N+1} h \Delta t P_{m,n} \left(\frac{Z_{m,n+1} - Z_{m,n}}{\Delta t} + \frac{E(\sqrt{x_m^2 + t_n^2}) e^{a Z_{m,n}}}{\left(1 + \left(\frac{Z_{m,n} - Z_{m-1,n}}{h} \right)^2 + \left(\frac{Z_{m,n} - Z_{m,n-1}}{\Delta t} \right)^2 \right)^{\frac{k}{2}}} \right) \mathbb{1}_{m,n} \end{aligned} \quad (4.12)$$

with

$$\mathbb{1}_{m,n} = \begin{cases} 1, & \text{for } -\sqrt{1-x_m^2} \leq t_n \leq \sqrt{1-x_m^2}; \\ 0, & \text{for } -1 \leq t_n \leq -\sqrt{1-x_m^2} \text{ and } \sqrt{1-x_m^2} \leq t_n \leq 1. \end{cases} \quad (4.14)$$

The variation with respect to the trench profile $Z_{m,n}$ gives a discrete adjoint

problem (4.15). For $n = 2 \dots N$, $m = 2 \dots M/2 - 1$

$$\begin{aligned}
& \frac{P_{m,n-1} - P_{m,n}}{\Delta t} + \frac{aE(\sqrt{x_m^2 + t_n^2}) \exp(aZ_{m,n})}{\left(1 + \left(\frac{Z_{m,n} - Z_{m-1,n}}{h}\right)^2 + \left(\frac{Z_{m,n} - Z_{m,n-1}}{\Delta t}\right)^2\right)^{\frac{k}{2}}} P_{m,n} \mathbb{1}_{m,n} - \\
& - \frac{kE(\sqrt{x_m^2 + t_n^2}) \exp(aZ_{m,n})}{\left(1 + \left(\frac{Z_{m,n} - Z_{m-1,n}}{h} + \left(\frac{Z_{m,n} - Z_{m,n-1}}{\Delta t}\right)\right)^2\right)^{\frac{k}{2}+1}} \frac{Z_{m,n} - Z_{m-1,n}}{h} \frac{P_{m,n}}{h} \mathbb{1}_{m,n} + \\
& + \frac{kE(\sqrt{x_{m+1}^2 + t_n^2}) \exp(aZ_{m+1,n})}{\left(1 + \left(\frac{Z_{m+1,n} - Z_{m,n}}{h}\right)^2 + \left(\frac{Z_{m+1,n} - Z_{m+1,n-1}}{\Delta t}\right)^2\right)^{\frac{k}{2}+1}} \frac{Z_{m+1,n} - Z_{m,n}}{h} \frac{P_{m+1,n}}{h} \mathbb{1}_{m+1,n} - \\
& - \frac{kE(\sqrt{x_m^2 + t_n^2}) \exp(aZ_{m,n})}{\left(1 + \left(\frac{Z_{m,n} - Z_{m-1,n}}{h} + \left(\frac{Z_{m,n} - Z_{m,n-1}}{\Delta t}\right)\right)^2\right)^{\frac{k}{2}+1}} \frac{Z_{m,n} - Z_{m,n-1}}{\Delta t} P_{m,n} \mathbb{1}_{m,n} + \\
& + \frac{kE(\sqrt{x_m^2 + t_{n+1}^2}) \exp(aZ_{m,n+1})}{\left(1 + \left(\frac{Z_{m,n+1} - Z_{m-1,n+1}}{h}\right)^2 + \left(\frac{Z_{m,n+1} - Z_{m,n}}{\Delta t}\right)^2\right)^{\frac{k}{2}+1}} \frac{Z_{m,n+1} - Z_{m,n}}{\Delta t} P_{m,n+1} \mathbb{1}_{m,n-1} + \\
& + \delta_{n,N} \sum_{j=1}^M (Z_{j,N} - Z_{exp}(x_j)) = 0
\end{aligned} \tag{4.15}$$

where $\mathbb{1}_{m,n}$ is defined by (4.14).

Derivation of the discrete version of (4.10) is complicated in comparison with case of the stationary abrasive waterjet (Section 3.2). We consider $M = 4$ values $\{E_m\}$ of the discretized etching rate function as the calibration parameters of the model. However, the discrete version of the Lagrangian (4.13) does not depend on these values explicitly. Instead it depends on the values of the etching rate function at the points $\sqrt{x_m^2 + t_n^2}$. There is no reason for $\sqrt{x_m^2 + t_n^2}$ to coincide with some of the points of space discretization x_i . Figure 4.2 illustrates this situation. The depths in the points x_i , $i = \overline{1, 4}$ parameterize the cross-section of the trench $Z(x, t)$. Suppose at time t the center of the jet passes the chosen cross-section. So, the computation of the direct problem requires only the model parameters E_i at this step. On the next step, $t \leftarrow t + \Delta t$, the value of the etching rate function acting in the x_3 is situated between the model parameters E_2 and E_3 .

This implies that the value $E(\sqrt{x_m^2 + t_n^2})$ has to be obtained as an interpolation between M parameters $\{E_m\}$. Afterwards this interpolation should be

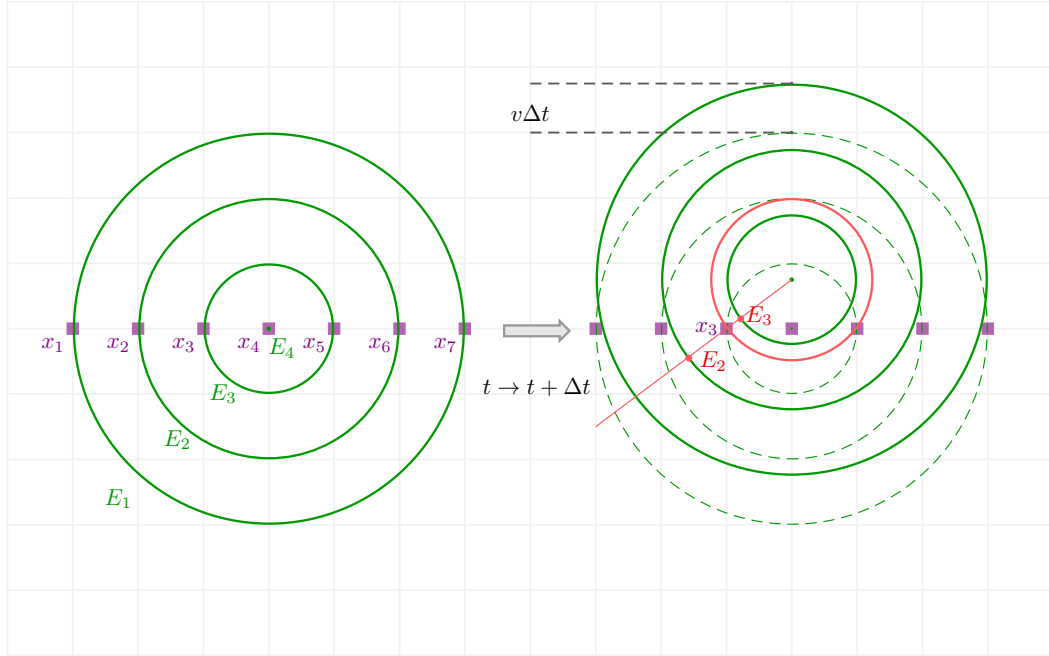


Figure 4.2 – Intermediate values of the etching rate function.

differentiated with respect to E_i to calculate $\frac{\partial L}{\partial E_i}$ from (4.13).

For example, Figure 4.3 illustrates the simplest case of a linear interpolation ([Antia, 2002]). For linear interpolation the described procedure implies:

- Check $r_{m,n} = \sqrt{x_m^2 + t_n^2} < 1$
- Find the index l that corresponds to $x_l < -1 + r_{m,n} < x_{l+1}$:

$$l = \text{floor} \left(\frac{1 - \sqrt{x_m^2 + t_n^2}}{h} \right) + 1.$$
- Interpolation:

$$E(r) = \text{interpolation}(E_l, E_{l+1}) = \frac{E_{l+1} - E_l}{h} (-r - x_l) + E_l$$
- Update the component of the gradient of the cost function with indexes l and $l + 1$

For the cubic natural spline ([Knott, 2012]) the procedure is as follows:

- Check $r_{m,n} = \sqrt{x_m^2 + t_n^2} < 1$

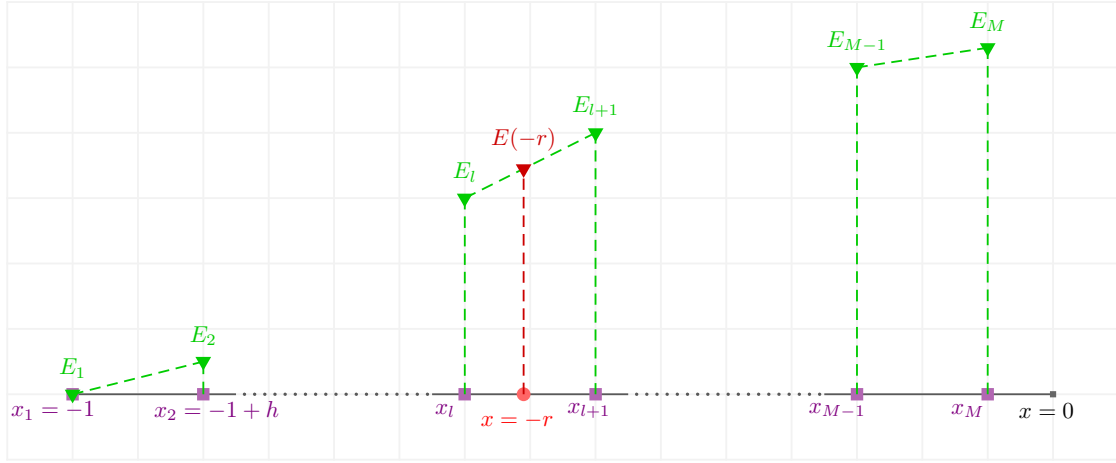


Figure 4.3 – Linear interpolation of the etching rate function.

- Find the index l that corresponds to $x_l < -1 + r_{m,n} < x_{l+1}$:

$$l = \text{floor} \left(\frac{1 - \sqrt{x_m^2 + t_n^2}}{h} \right) + 1.$$

- Build the cubic spline $\alpha_1^l + \alpha_2^l x + \alpha_3^l x^2 + \alpha_4^l x^3$ for each interval $[x_l, x_{l+1}]$. This step implies the solution of the $4(M-1) \times 4(M-1)$ linear system $A\vec{\alpha} = \vec{E}_p$ for $4(M-1)$ unknown coefficients of the splines. Matrix A depends only on the space discretization points $\{x_i, i = \overline{1, M}\}$

$$\vec{\alpha} = (\alpha_1^1 \ \alpha_2^1 \ \alpha_3^1 \ \alpha_4^1 \ \dots \ \alpha_1^{M-1} \ \alpha_2^{M-1} \ \alpha_3^{M-1} \ \alpha_4^{M-1})^T$$

$$\vec{E}_p = (E_1 \ E_2 \ E_2 \ E_3 \ E_3 \ \dots \ E_{M-1} \ E_M \ 0 \ \dots \ 0)^T$$

- Interpolation:

$$E(r) = \text{interpolation}(E_1, \dots, E_M) = \alpha_1^l + \alpha_2^l r + \alpha_3^l r^2 + \alpha_4^l r^3,$$

here $\alpha_1^l, \alpha_2^l, \alpha_3^l, \alpha_4^l$ are the coefficients of the l^{th} cubic spline.

- Update the components of the gradient of the cost function by differentiation of the $\vec{\alpha}$:

$$\frac{\partial \vec{\alpha}}{\partial E_l} = A^{-1} \frac{\partial \vec{E}_p}{\partial E_l}$$

4.3 Moving abrasive waterjet: parameters calibration

It is possible to obtain the gradient of the cost function by application of the automatic differentiation (Section 1.3) to the program that computes the cost function. The etching rate function was discretized into a set of $M = 636$ calibration parameters on the interval $[-1, 1]$. As before, this number eventually was reduced to a half for the symmetrical experimental data.

As it was discussed in the previous section, an interpolation was used to obtain the intermediate values of E for the numerical solution of the direct problem (4.2). Substitution of the numerical solution of (4.2) into the discrete version of the cost function (3.2) and further numerical integration allows us to obtain the cost function $J(u)$ in a form of a computer program. Then the gradient of the cost function $\nabla J(u)$ was obtained using an adjoint mode of the automatic differentiation software Tapenade [Hascoet and Pascual, 2013], developed in INRIA Sophia Antipolis. Once the numerical value of the cost function and its gradient were calculated, parameters of the model u^* were obtained using l-BFGS minimizer [Byrd et al., 1995, Morales and Nocedal, 2011]. This solver is based on the gradient projection method and uses a limited memory BFGS matrices to approximate the Hessian of the objective function (Section 1.1).

This approach was tested on the calibration of the simulated experimental data. When one of the parameters is assumed to be the only parameter of the model, the calibration procedure is able to retrieve its value with a high accuracy. A problem of uniqueness of the numerical solution arises when E, k, a are calibrated simultaneously. The result of the calibration procedure describes the simulated experiment with a desired high accuracy, but gives the values of parameters that differ from the ones used for the generation of Z_{exp} .

For example, the trench represented by the red line on Figure 4.5 was used as an experimental data for model calibration. This trench was obtained by solving the direct problem (4.2) with the values of the calibration parameters chosen to be $\{\tilde{k}, \tilde{a}, \tilde{E}\}$. The etching rate function \tilde{E} is presented in Figure 4.4, the values of scalar parameters are $\tilde{k} = 0.36$ and $\tilde{a} = 0.2$. Obtained set of calibration parameters $\{k^*, a^*, E^*\}$ describes this trench with high accuracy (red stars in Figure 4.5). The corresponding to $\{k^*, a^*, E^*\}$ value of the cost function is of order of 10^{-9} . In the same time the values $\{k^*, a^*, E^*\}$ are different from the real parameters of the model $\{\tilde{k}, \tilde{a}, \tilde{E}\}$. The behaviour of the etching rate function \tilde{E} is shown in Figure 4.4, the obtained values of parameters k and a are $\tilde{k} = 0.03 \neq k^*$ and $\tilde{a} = 0.1 \neq a^*$. When this set of calibrated parameters is used to generate a trench that corresponds to a different speed of the jet $w \neq v$, the discrepancy between

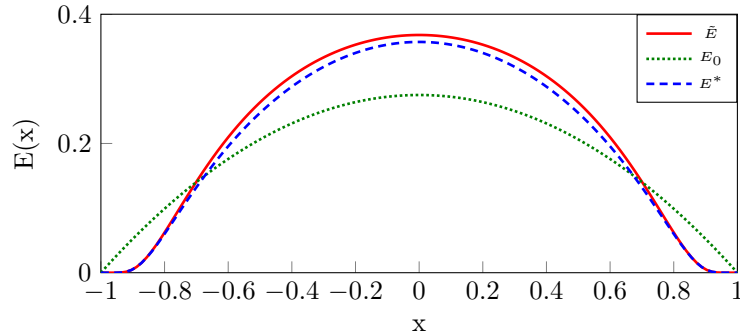


Figure 4.4 – Calibration of the etching rate function.
 \tilde{E} was used for the simulation of the experimental data.
 E_0 corresponds to the first guess in the minimization procedure.
 E^* represents the result of calibration.

two trenches becomes too big. The comparison between simulated experiments and trenches modelled with $\{k^*, a^*, E^*\}$ are presented in Figure 4.5.

Such a non-uniqueness of the solution does not come as a total surprise. The simultaneous change of the parameters of the model k, a and E can lead to the same profile of the trench. When trench becomes deeper the local incident angles of the waterjet impact increases. Because of the cosine dependence in the direct problem, the erosion power of the jet decreases. Moreover, the bigger is parameter k , the bigger is the loss of erosion power. The same considerations are valid for parameter a . It is introduced in the direct model to take into account the influence of the stand-off distance of the jet. When the trench gets deeper, the local distance from the surface to the jet increases, and this results in the loss of erosion power. The bigger is parameter a the less erosive is the impact of the jet. In the example considered above the calibrated value of k , k^* is smaller than the real values \tilde{k} , and the calibrated value of a , a^* is smaller than \tilde{a} . The two changes correspond to more aggressive jet. To obtain the desired profile of the experimental trench, this difference should be compensated by smaller values of the etching rate function. Which is the case in the Figure 4.4.

When the jet moves faster, it has less time to erode the material in a given point, so corresponding trench is shallower. In this situation, the decrease in etching rate function does not have enough time to compensate for more erosive jet due to change in k and a . As a result trench that corresponds to the calibrated values of parameters is deeper than one corresponding to the real values. For the slower jet the situation is reversed, and decrease in the etching rate function overcompensate the changes in k and a , resulting in shallower trench in compare with real one.

However, the main interest of the calibration of the model is a further use of

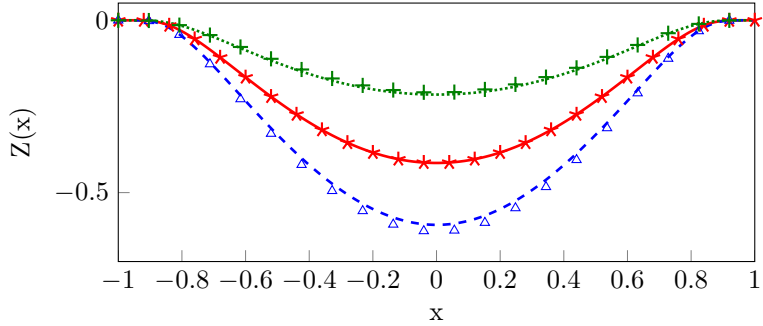


Figure 4.5 – Profiles of the trenches.

Lines correspond to modelling with calibrated values of parameters $\{k^*, a^*, E^*\}$. Markers correspond to the experimental data simulated with $\{\tilde{k}, \tilde{a}, \tilde{E}\}$, in particular red stars correspond to the experimental data used for calibration. Red color describes the simulations corresponding to the speed of the jet $v = 1$; green - the simulated experimental data corresponding to $v = 1.5$; blue - to $v = 0.5$.

the obtained parameters for the freeform generation. To overcome this problem of non-uniqueness we proposed the calibration based on two experiments instead of one. These experiments describe the cross-sections of the trenches, Z_{exp}^v and Z_{exp}^w , that correspond to different speeds of the waterjet, v and w . In terms of cost function this means that (4.3) is modified in the following way:

$$J(E, k, a) = \frac{1}{2} \int_{-1}^1 (Z^v(x, t=1) - Z_{exp}^v(x))^2 dx + \\ + \frac{1}{2} \int_{-1}^1 (Z^w(x, t=1) - Z_{exp}^w(x))^2 dx + \frac{\alpha}{2} \int_{-1}^1 |\nabla E(x)|^2 dx, \quad (4.16)$$

where Z^v corresponds to the trench, simulated from (4.2) with the etching rate function E , while Z^w corresponds to the trench, simulated from (4.2) with the etching rate function $\frac{v}{w}E$. This difference in the etching rate functions for two experiments is due to the dimensionless character of (4.2).

Running the developed calibration procedure with the modified cost function allowed to retrieve the parameters of the model for the numerically generated experimental data. Figure 4.6 gives an example of the calibration of the etching rate function by minimization of the modified cost function (4.16). The values of the parameters k and a that were used for the simulation of the experimental data are: $\tilde{k} = 1.4$, $\tilde{a} = 0.2$. The corresponding calibrated values are: $k^* = 1.4039$, $a^* = 0.1942$. The minimum was achieved in 106 iterations of the l-BFGS solver.

Figure 4.7 gives the dependence of the accuracy of the calibration $\|Z_v^* - Z_{exp}^v\|$ as a function of the regularization parameter α . Here Z_v^* is a solution of the direct

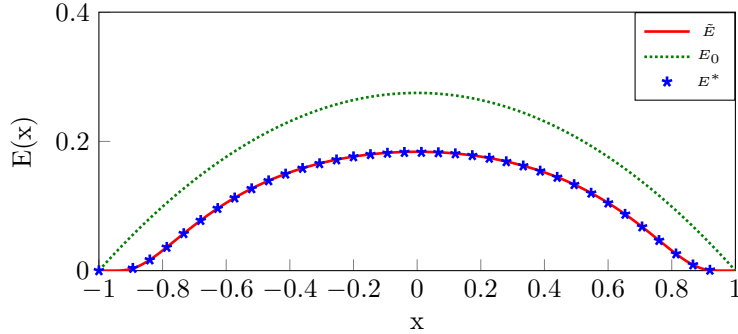


Figure 4.6 – Calibration of the etching rate function from the two generated numerically experimental data

problem (4.2) corresponding to the solution of the calibration procedure $k = k^*$, $a = a^*$ and $E = E^*$ and to the speed of the jet v . The graph on 4.7 has a form of a letter "L". The L-curve criterion of choice of regularization parameter ([Hansen and O'Leary, 1993], [Hansen, 1999]) consists in taking α from the corner of L . The regularization parameter $\alpha = 10^{-5}$ was chosen for simulations leading to the described calibrated values.

Calibrated parameters $\{k^*, a^*, E^*\}$ allow to predict the outcome of the experiments with an arbitrary feed speed of the jet. Figure 4.8 illustrates such prediction. Black and red trenches were used in the cost function (4.16) as the experimental data Z_{exp}^v and Z_{exp}^w . For this case $v = 2w$, thus ratio $\frac{v}{w} = 2$. Obtained values $\{k^*, a^*, E^*\}$ were used to generate the trenches that correspond to different jet feed speeds: $v_1 = 2v$, $v_2 = \frac{2}{3}v$, $v_3 = \frac{1}{4}v$, that is with ratios 0.5, 1.5 and 4.

Figure 4.9 gives an example of the local distribution of the error:

$$\epsilon_{loc} = \frac{(Z^*(x) - Z_{exp}(x))}{\sqrt{\frac{1}{2} \int_{-1}^1 (Z_{exp}(x))^2 dx}}.$$

This distribution does not have any particular behaviour in comparison with the case of calibration of the real experimental data that we will consider later in this section (Figure 4.14, Figure 4.15).

On this step the real experimental data can be passed to the calibration procedure. We used the experimental trenches from the work of Lozano et al.

[Torrubia et al., 2015] As figure 4.10 shows, the considered experimental trenches have the regions of the pilled up material on the edges, where $Z_{exp}(x) > 0$.

This phenomenon cannot be explained in the framework of the geometrical model (4.2) that only describes the erosion mechanism, and do not take into account plasticity of the material. However, the calibration procedure tries to find

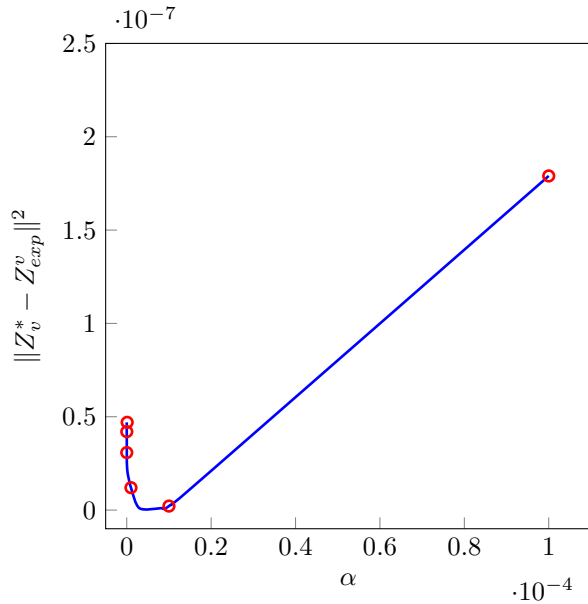


Figure 4.7 – Accuracy of the calibration of the trench corresponding to the feed speed of the jet v as a function of the regularization parameter α .

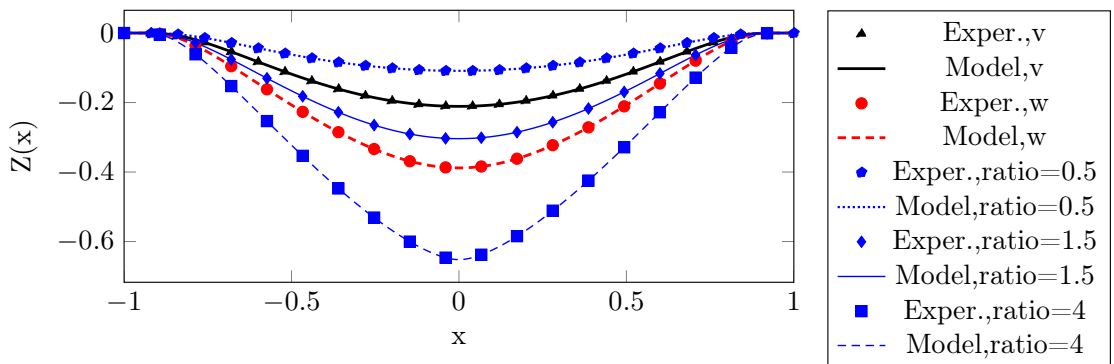


Figure 4.8 – Calibrated trenches and predicted trenches for the calibration of the numerically simulated experimental data

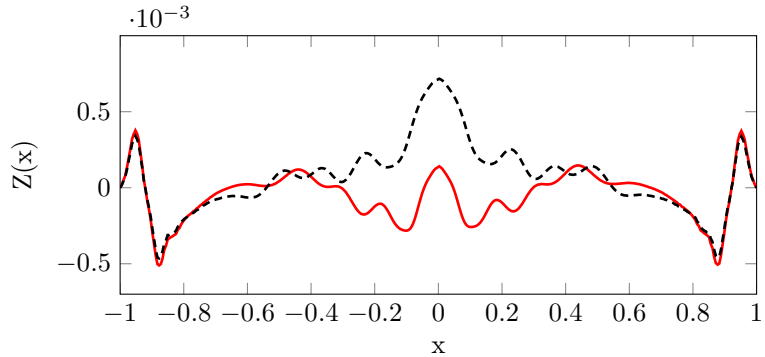


Figure 4.9 – Errors of calibration of two numerical experiments: $v = 2$, $w = 1$

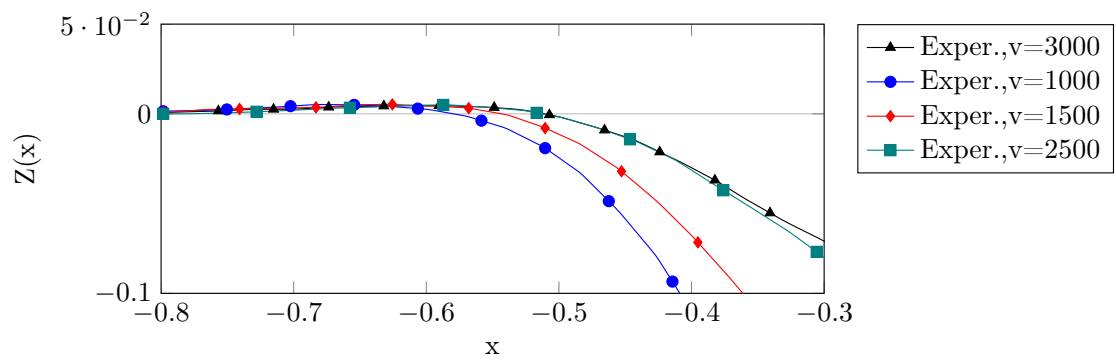


Figure 4.10 – Zoom on the edges of the experimental trenches.

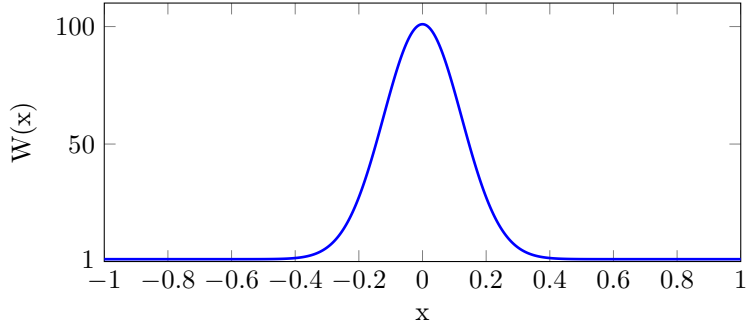


Figure 4.11 – Weight function used for the calibration of the experimental data.

the parameters that would explain this effect. We introduce the second modification of the cost function:

$$\begin{aligned} J(E, k, a) = & \frac{1}{2} \int_{-1}^1 W(x) (Z^v(x, t=1) - Z_{exp}^v(x))^2 dx + \\ & + \frac{1}{2} \int_{-1}^1 W(x) (Z^w(x, t=1) - Z_{exp}^w(x))^2 dx + \frac{\alpha}{2} \int_{-1}^1 |\nabla E(x)|^2 dx, \end{aligned} \quad (4.17)$$

where function W in the integrals is a weight function. Making the weight function W smaller near the edges than in the center of the trenches allowed to shield the calibration procedure from the secondary effects non-included in the model. Figure 4.11 represents the weight function used for the experimental data calibration.

The minimization solver [Byrd et al., 1995, Morales and Nocedal, 2011] was initialized with its internal parameter $p = 15$. This parameter describes the maximum number of variable metric corrections in l-BFGS algorithm. The stopping criterion was based on the size of the projected gradient, the minimization stopped when the maximal component of the projected gradient became less than $pgtol = 10^{-4}$. The numerical value of the regularization parameter α was chosen by the numerical experimentation based on L -curve regularization parameter selection method ([Hansen and O’Leary, 1993], [Hansen, 1999]). The optimal value $\alpha = 10^{-5}$ allowed to avoid the oscillations in the solution without over-smoothing it.

Trenches that correspond to the speed of the jet $v = 3000\text{mm/min}$ and $w = 1000\text{mm/min}$ were used as the experimental data $Z_{exp}^v(x)$ and $Z_{exp}^w(x)$ in the cost function (4.17). The minimum was achieved in 97 iterations of the l-BFGS solver in approximately 1 hour of computational time on a 2.8GHz Intel Core i7 with 16GB of RAM. Obtained values of the scalar parameters were $k_{exp}^* = -0.426$, $a_{exp}^* = 0.81$, and the calibrated etching rate function E_{exp}^* is shown in figure 4.12. Negative value of the calibrated parameter k_{exp}^* is explained by

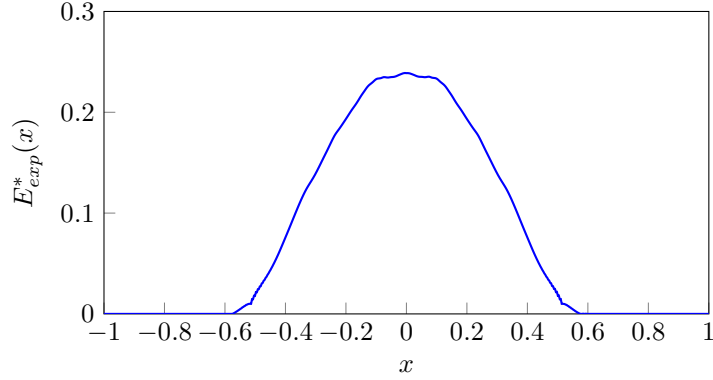


Figure 4.12 – Calibrated from the experiments etching rate function

the fact that the experimental data used for the calibration corresponded to the milling of Ti-6Al-4V. This material exhibits a ductile behaviour. According to the literature [Torrubia et al., 2015, Oka et al., 2005], the erosion increases when the particles angle of impingement varies from 0° up to 50° . In this work higher values of angles were not attained, so the inverse cosine dependency of the erosion was able to trace correctly the increasing character of the erosion. Extension of the developed calibration procedure to the different erosion models is a subject of future work.

Calibrated set of the model parameters $\{E_{exp}^*, k_{exp}^*, a_{exp}^*\}$ was further validated by comparison of the experimental data for the speed 1500mm/min and 2500mm/min with the numerical solution of the direct problem (4.2). The reliability of the obtained results were estimated by a global error ϵ (4.18).

$$\epsilon = \frac{\sqrt{\frac{1}{2} \int_{-1}^1 (Z^*(x) - Z_{exp}(x))^2 dx}}{\sqrt{\frac{1}{2} \int_{-1}^1 (Z_{exp}(x))^2 dx}}, \quad (4.18)$$

where Z^* is the trench profile calculated with the set of calibrated parameters $\{E_{exp}^*, k_{exp}^*, a_{exp}^*\}$.

Figure 4.13 represents the experimental trenches and the cross-sections obtained by solving the direct problem (4.2) with the calibrated parameters $E_{exp}^*, k_{exp}^*, a_{exp}^*$.

The results in figure 4.13 show that the developed calibration procedure allows to predict the profile of the trench cross-section with a high accuracy for various speeds of the jet: 1.46% for $v = 1000\text{mm/min}$, 1.48% for $v = 1500\text{mm/min}$, 7.33% for $v = 2500\text{mm/min}$ and 4.15% for $v = 3000\text{mm/min}$. Figure 4.14 gives

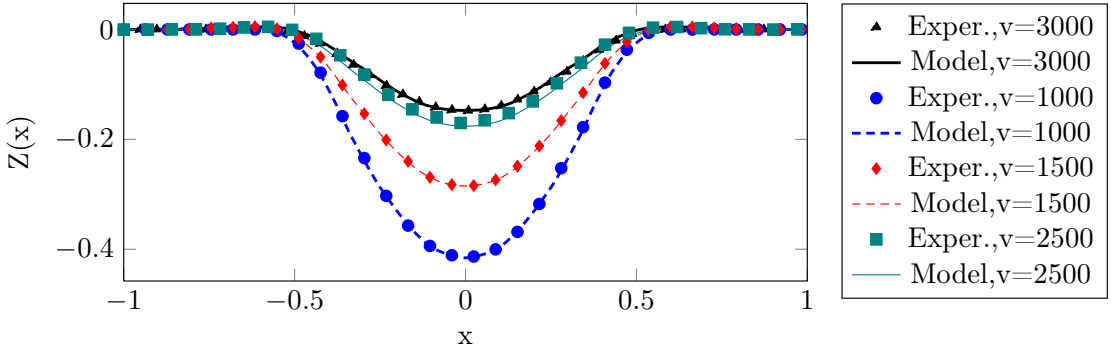


Figure 4.13 – Experimental trenches and results of numerical modelling for different speeds of the jet. Trenches for $v = 3000\text{mm/min}$ and $w = 1000\text{mm/min}$ were used for calibration of the parameters of the model.

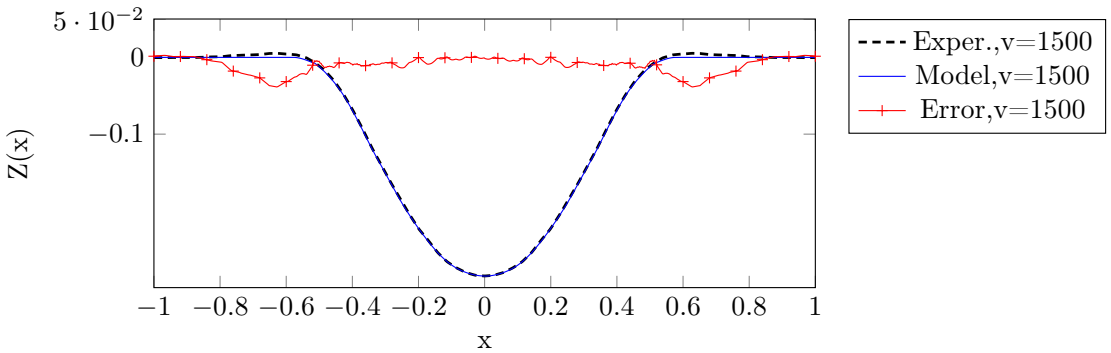


Figure 4.14 – Local error of the calibration for the jet feed speed 1500mm/min

an example of the local distribution of the error:

$$\epsilon_{loc} = \frac{(Z^*(x) - Z_{exp}(x))}{\sqrt{\frac{1}{2} \int_{-1}^1 (Z_{exp}(x))^2 dx}}.$$

Figure 4.14 and Figure 4.15 show that a level of accuracy of the developed calibration procedure is higher than stated above for the regions away from the trenches edges. Such a behaviour has not appeared during the calibration of the numerically simulated experimental data (Figure 4.9). As was discussed above, the effects on the trenches edges cannot be described in the framework of the considered geometrical model. This fact imposes limitations on the accuracy of the calibration procedure in these regions. For more accurate prediction of the trench profile the model (2.6) and its particular case (4.2) should be further developed to take into account the pilled-up material.

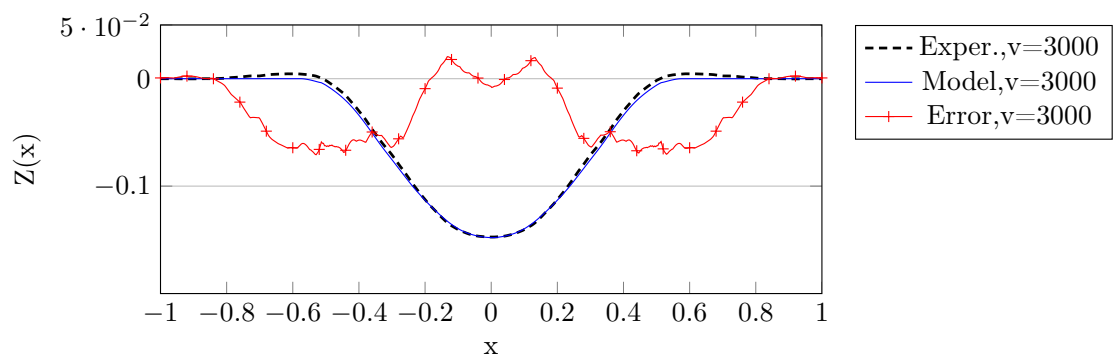


Figure 4.15 – Local error of the calibration for the jet feed speed 3000mm/min

Chapter 5

Focus Ion Beam milling

5.1 Introduction to the FIB milling technique

Focused ion beam (FIB) milling has been widely used in different applications ([Giannuzzi et al., 2006],[Volkert and Minor, 2007],[Yao, 2007]). It allows the fabrication of elements of size down to $\sim 30\text{nm}$, for example, the tips of the atomic force microscope probe.

The ions are created by heating the metal source by electrical current. When heated, metals tend to loose electrons, thus becoming positively charged ions. These ions are accelerated by the electric potential difference applied between the ions source and a target surface. Moreover, they are focused by the system of electrostatic and magnetic fields. When the accelerating voltage is high, the ions obtain enough energy to induce the sputtering effect on the target material ([Sigmund, 1987]). The sputtering yield, Y , is defined as a number of sputtered atoms of target material per incident ion. Y depends on the incident angle of the ion, that is the angle between the ion velocity and the normal to the target surface in the point of impact. Sputtering yield can be measured experimentally ([Andersen and Bay, 1981]) or calculated by Monte Carlo simulations ([Timilsina and Rack, 2013]). Figure 5.1 shows the sputtering yield of silicon bombarded by gallium ions.

The simplest empirical equation describing the evolution of the target surface during FIB milling can be obtained from the mass conservation ([Katardjiev et al., 1988]). We consider the FIB that hits the surface $Z(x, y)$. Axis Oz is aligned with the beam axis, but it points in the opposite direction. The evolution of the depth Z of the target surface with time t during the FIB milling can be described by the following empirical PDE:

$$\frac{\partial Z}{\partial t} = -F(r)Y(\theta) \cos \theta. \quad (5.1)$$

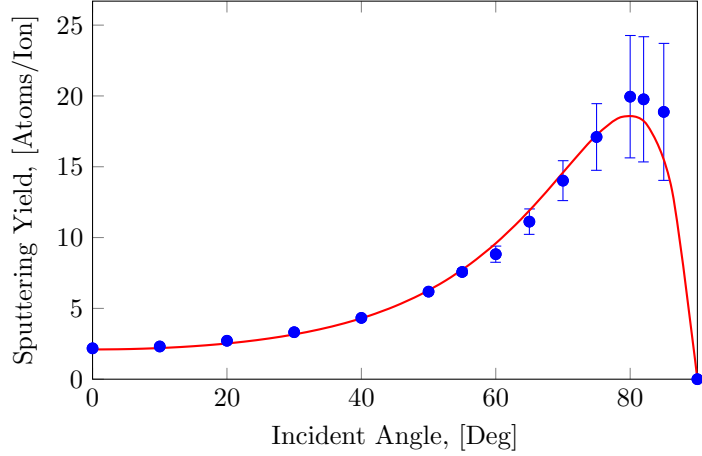


Figure 5.1 – Sputtering yield Y for Si, as a function of the incident angle.

Here Y is the sputtering yield, θ is an incident angle of ions at the point $(x, y, Z(x, y))$. F is the ion intensity distribution or beam profile within the beam cross section perpendicular to the beam axis. It is function of r , the distance to the beam axis. Model (13) does not take into account the secondary effects: re-deposition, sputtering by scattered ions ([Kim et al., 2007]), material swelling ([Lugstein et al., 2003]).

Usually the ion intensity distribution is considered as a Gaussian distribution ([Ali et al., 2010]). Experimental determination of F is often based on the assumption that the beam replicates its profile on the target surface ([Ali and Hung, 2001], [Wang and Wang, 1996]). This assumption is analogous to the linearization of (13). The goal of the following sections is to develop procedure of calibration of F by PDE constrained optimization approach. The experimental setup is modeled by the direct problem (13) with some choice of the beam profile F . Then the task is to minimize the discrepancy between the experimental data and the result of numerical simulation.

In Section 5.2 we will consider the experimental setup that corresponds to a crater sputtering and in Section 5.3 - to trench sputtering.

5.2 Crater sputtering

We consider a FIB that hits a material surface perpendicularly and stays at the same spot for period of time T (dwell time). The target surface is initially flat: $Z = 0$. Created in such way geometry represents a crater. By symmetry this crater can be described by its central cross section, that is by the depth $Z(x)$. Figure 5.2 describes schematically this situation and shows the choice of the coordinate system.

The evolution of the crater depth is governed by PDE (5.2).

$$\frac{\partial Z}{\partial t} = -F(x)Y(\theta) \cos \theta, \quad (5.2)$$

where $\theta = \arccos \left(\frac{1}{\sqrt{1 + (\frac{\partial Z}{\partial x})^2}} \right)$ is an angle between the FIB and the unit normal

to the target surface. Equation (5.2) completed by the initial condition $Z(x, t = 0)$ form the direct problem for FIB. We suppose that sputtering yield is a known from the experiment function. To be specific, Figure 5.1 describes the behavior of the sputtering yield for silicon. In contrast, we treat the beam profile F as a calibration parameter of the model.

Suppose that an experimental cross section profile Z_{exp} is available after sputtering stopped at dwell time $t = T$. We introduce a cost function:

$$J(F) = \frac{1}{2} \int_{-1}^0 (Z(x, T) - Z_{exp}(x))^2 dx + \frac{\alpha}{2} \int_{-1}^0 |\nabla F(x)|^2 dx, \quad (5.3)$$

where α is a regularization coefficient. The first integral in (5.3) describes the discrepancy between the solution of the direct problem (5.2) $Z(x, T)$ and the experimental data Z_{exp} . The integration is performed on interval $[-1, 0]$, because of the symmetry of the crater. The second integral is responsible for the Tikhonov regularization ([Tikhonov and Arsenin, 1977]). We use the a priori knowledge about the smoothness of the beam profile for the construction of the second term in (5.3). This term plays a regularization role, its presence ensures that the oscillating solution for $F(x)$ would be cast out during the optimization process. We will come back to a question of choice of α later in this section. Finally, the calibration problem for F can be written as an optimization problem:

Problem 3. Find the positive function F^* such that

$$J(F^*) = \inf_F J(F),$$

under the constraint that Z is the output of the model (5.2) with the input F .

We solved this PDE constrained optimization problem (Problem 3) using Automatic Differentiation approach (Section 1.3). The direct problem (5.2) was dis-

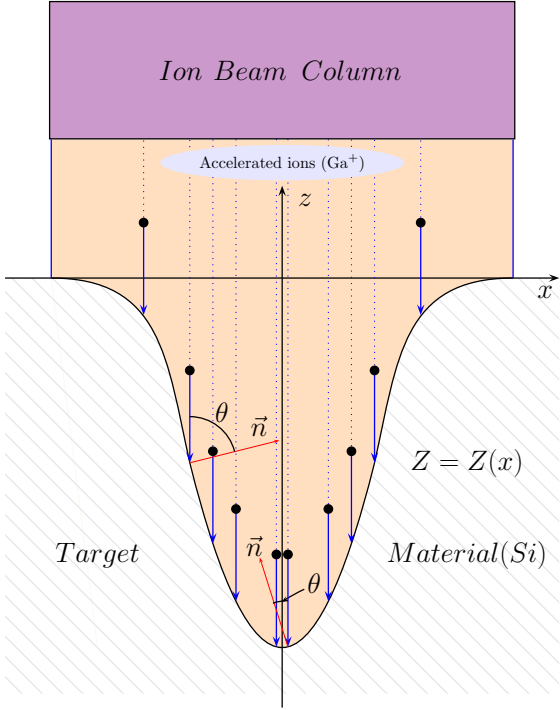


Figure 5.2 – Schematic representation of the cross-section of the sputtered crater.

cretized in space and in time. The space interval $[-1, 0]$ was divided in M equal sub-intervals. The values F_i of F in $M + 1$ space discretization points $\{x_i, i = \overline{1, M + 1}\}$ were considered as the calibration parameters of the model. Then the gradient of the cost function $J(F_1, \dots, F_M)$ was obtained by passing the program evaluating J to TAPENADE (Section 1.3). When the value of the cost function and its gradient are available, the minimum in the Problem 3 can be found by application of l-BFGS minimizer (Section 1.1).

Figure 5.3 gives an example of the successful calibration of F from the experimental data simulated by direct problem with an arbitrary chosen $F = \tilde{F}$. Minimization solver is initialized with F_0 , and it gives the calibrated value F^* as an output. F^* was found in 50 iterations of l-BFGS minimizer. The developed calibration procedure is able to retrieve the true value \tilde{F} of the beam profile with high accuracy: the relative error $\varepsilon_F = \frac{\|F^* - \tilde{F}\|}{\|F^*\|}$ is of order of fraction of percent.

Figure 5.4 shows the simulated experimental cross section \tilde{Z} that corresponds to the choice \tilde{F} as well as the cross section that corresponds to the initial guess F_0 and the calibrated value F^* .

Let us come back to the choice of the regularization parameter α . When the cost function only describes the discrepancy $\|Z - Z_{exp}\|^2$, that is when $\alpha = 0$, the

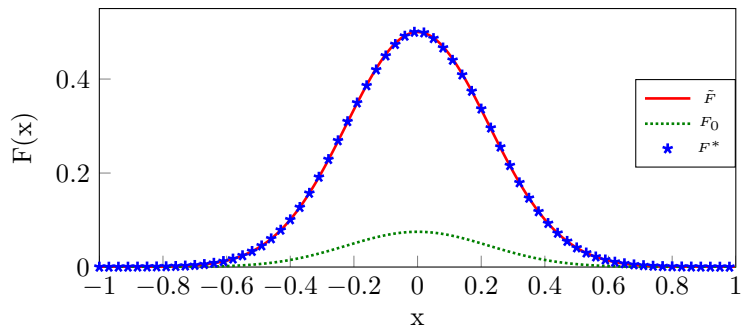


Figure 5.3 – Calibration of the beam profile from the geometry of the sputtered crater.

\tilde{F} was used for the simulation of the experimental data.

F_0 corresponds to the first guess in the minimization procedure.

F^* represents the result of calibration.

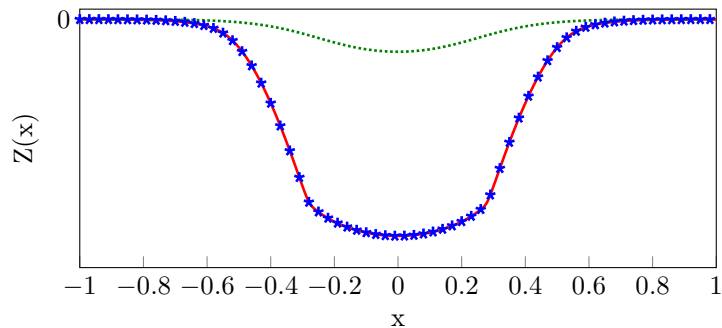


Figure 5.4 – Profiles of the crater cross sections.

Green dashed line represents the profile that corresponds to the first guess of the beam profile F_0 .

Red line corresponds to the simulated with $F = \tilde{F}$ experimental data.

Blue stars correspond to the crater simulated with the calibrated value F^* .

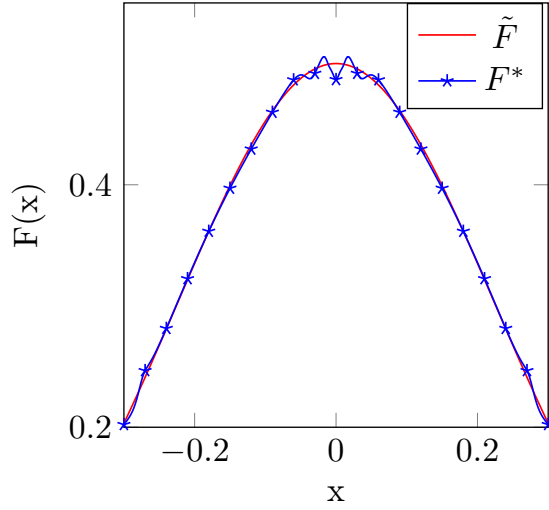


Figure 5.5 – Effect of the low values of α on the result of calibration: $\alpha = 0$.

\tilde{F} was used for the simulation of the experimental data.

F^* represents the result of calibration.

calibration procedure gets the oscillating solution F^* . Figure 5.5 presents a zoom on the result of the calibration with $\alpha = 0$.

The increase of α leads to eventual oversmoothing of the calibrated function. This situation is illustrated in the Figure 5.6. For the value $\alpha = 10^{-4}$ the calibrated function F^* visibly drives away from the real value \tilde{F} (on the left in Figure 5.6). In the limit, for the unreasonably high values of α , the minimization procedure pushes F towards constant function (on the right in Figure 5.6 for $\alpha = 1.0$).

The regularization parameter α was chosen by L -curve regularization parameter selection method ([Hansen and O’Leary, 1993], [Hansen, 1999]). Figure 5.7 gives the dependence of the accuracy of the calibration $\|Z^* - Z_{exp}\|$ on the regularization parameter α . Here Z^* is a solution of the direct problem (5.2) corresponding to $F = F^*$ solution of the calibration procedure. The graph on 5.7 has a form of a letter "L", in a somewhat abstract manner. The L -curve criterion of choice of regularization parameter consists in taking α from the corner of L . Results on the Figures 5.3 and 5.4 correspond to a choice $\alpha = 0.75 * 10^{-5}$.

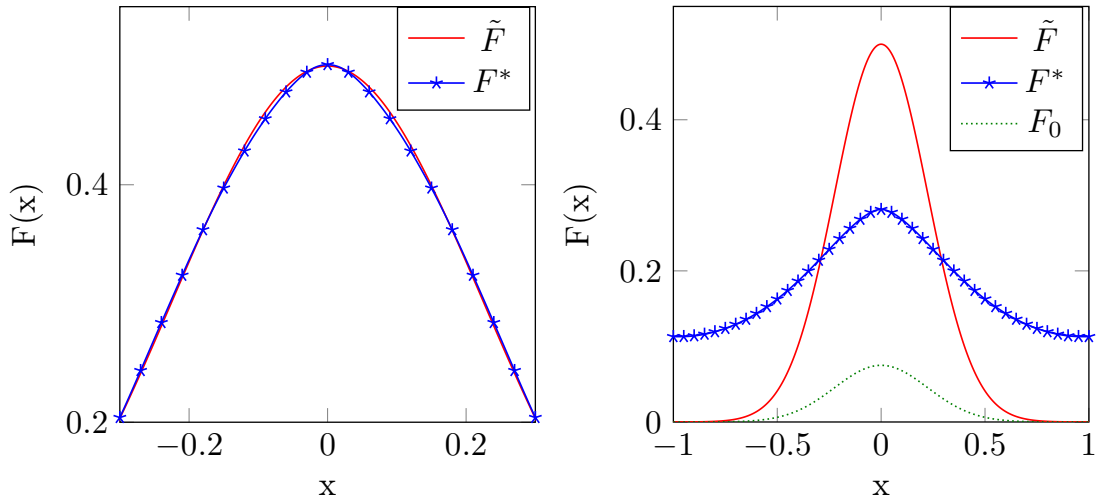


Figure 5.6 – Effect of the high values of α on the result of calibration.
 Result of the calibration with $\alpha = 10^{-4}$ on the left and $\alpha = 1.0$ on the right.
 \tilde{F} was used for the simulation of the experimental data.
 F^* represents the result of calibration.

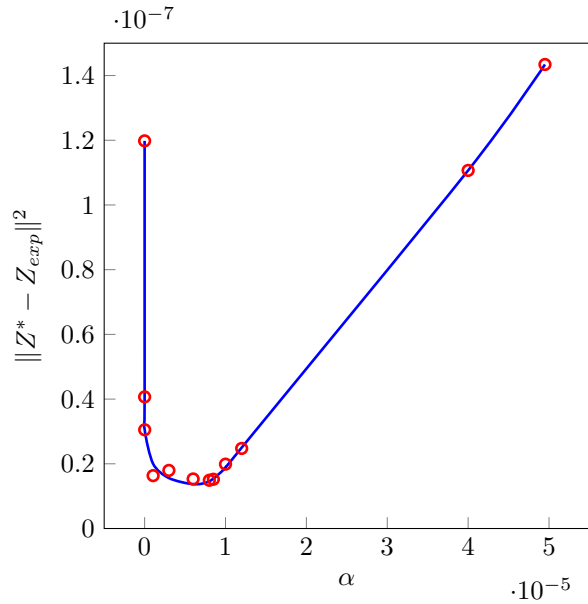


Figure 5.7 – Accuracy of the calibration as a function of the regularization parameter α for crater sputtering.

5.3 Trench sputtering

In this section we will consider sputtering of the trench. The sputtering is performed following line pattern. FIB hits the initially flat surface perpendicularly and stays at the same pixel point for the dwell time T . The first pixel point coincides with the origin of coordinate system. Then FIB moves to the next pixel point situated on distance δ from the previous one, as Figure 5.8 shows. During the change of the location the FIB is turned off. In this way, N_y pixel points are scanned, and FIB concludes its first cycle of milling. All pixel points are situated on the same line, and the coordinate system is chosen so that this line coincides with Oy . After scanning all the pixel points on this line, FIB returns on the starting point (on the origin) and the process starts all over again. The procedure is repeated for N_c cycles of milling.

The evolution of the target surface is described by (5.4).

$$\begin{cases} \frac{\partial Z}{\partial t} = -F(r)Y(\cos(\theta(Z_x, Z_y))) \cos(\theta(Z_x, Z_y)), \\ Z(x, y, 0) = 0. \end{cases} \quad (5.4)$$

Here r is a distance from the center of the beam to the point (x, y) and θ is an angle between the FIB axis and a normal to the target surface at the given point $(x, y, Z(x, y))$, that is $\cos(\theta(Z_x, Z_y)) = \frac{1}{\sqrt{1 + \left(\frac{\partial Z}{\partial x}\right)^2 + \left(\frac{\partial Z}{\partial y}\right)^2}}$.

The sputtering area defines the domain of definition Ω in (5.4):

$\Omega = \{(x, y) : x \in [-R, 0], y \in [-R, R + \delta(N_y - 1)]\}$. Because of the symmetry of the problem we consider only half of the milled trench in Ox direction. R is a radius of the FIB (Figure 5.8), $R = 1$ everywhere in rest of this section.

Figure 5.9 gives an example of the numerical solution of the direct problem (5.4) for the number of pixel points $N_y = 7$, the pixel distance $\delta = 0.5$. In contrast

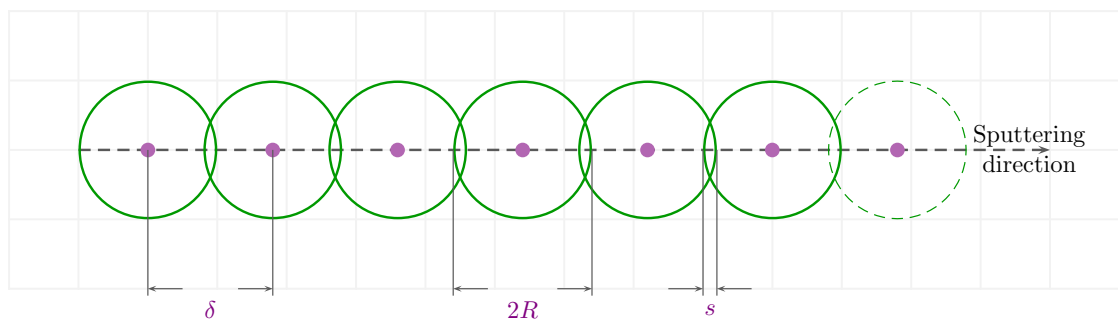


Figure 5.8 – Schematics of scanning mode for the line sputtering.

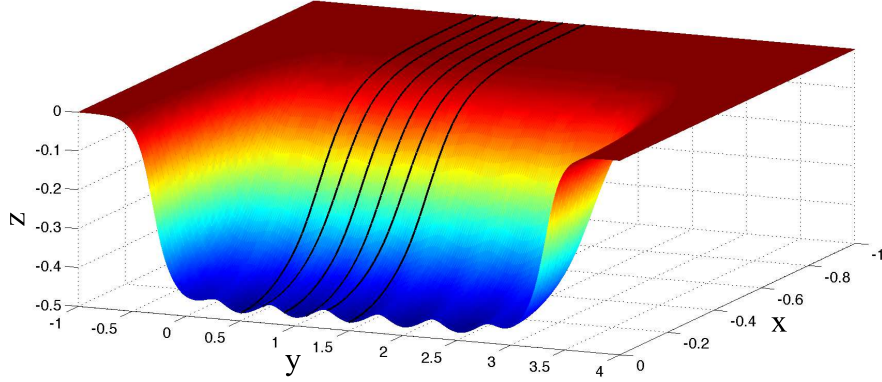


Figure 5.9 – Example of the sputtered trench $Z(x, y)$ with six cross section profiles corresponding to different $y^c = \text{Const}$ (black lines)

with the trench milled by the abrasive waterjet, the FIB trench cannot be described by its single cross section perpendicular to Oy direction. However the shape of the surface $Z(x, y)$ cannot be measured experimentally for the whole range of Ω . In experiment one still measures a profile of the cross section plane $y^c = \text{Const}$. Moreover, it is hard to determine the coordinate y^c precisely in the experiment, because the diameter of the beam is of order of hundred nanometers and the pixel distance δ of ten nanometers. We are interested in the experimental setup that leads to the trenches with constant depth from the experimental point of view. That means that the pits in the trench (see Figure 5.9) should be indistinguishable in experiment.

In the spirit of the developed calibration approach, we would like to build the cost function. This function should estimate the difference between the experimental cross section Z_{exp} and the cross section Z_{num} obtained as the numerical solution of the direct problem (5.4):

$$J(F) = \frac{1}{2} \int_{-1}^0 (Z_{num}(x) - Z_{exp}(x))^2 dx.$$

The cross section of the numerical trench is not the same for every y_c . We built the numerical cross section Z_{num} in the cost function as an average over a set of K cross sections in the middle of the trench:

$$Z_{num}(x) = \frac{1}{K} \sum_{k=1}^K Z(x, y_k^c) \quad (5.5)$$

Figure 5.10 illustrates the choice of the cross section coordinates y_k^c in (5.5). K equally spaced cross section are placed from the edge to the center of the beam

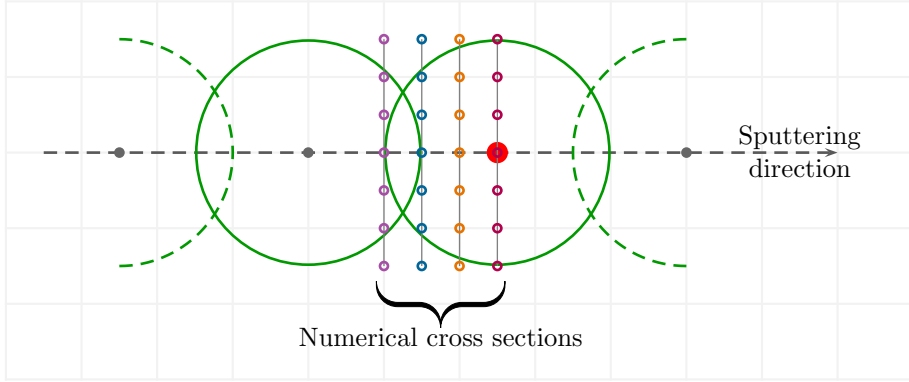


Figure 5.10 – Choise of the numerical cross sections for the calculation of the average numerical cross section in the cost function.

spot, in Figure 5.10 $K = 4$. This beam spot corresponds to the pixel point in the middle of the trench (big red point in Figure 5.10).

Let us consider an application of this approach to the construction of Z_{num} on the example of numerically generated trench from Figure 5.9. From $N_y = 7$ pixel points, the 4th with $y_k^c = 1.5$ was chosen as an anchor for generation of $K = 6$ cross sections with $\{y_k^c, k = 1, 6\} = \{0.5; 0.7; 0.9; 1.1; 1.3; 1, 5\}$. These cross sections are marked by the black lines in Figure 5.9.

Figure 5.11 illustrates the calculation of the average profile Z_{num} .

As before for the crater sputtering (Section 5.2) the cost function is augmented with a regularization term:

$$J(F) = \frac{1}{2} \int_{-1}^0 (Z_{num}(x) - Z_{exp})^2 dx + \alpha \int_{-1}^0 (\nabla F(x))^2 dx. \quad (5.6)$$

The choice of α will be discussed later in this section.

The problem of calibration of the beam profile F becomes the problem of minimization of the cost function 5.6:

Problem 4. *Find the positive function F^* such that*

$$J(F^*) = \inf_F J(F),$$

under the constraint that Z_{num} is computed by (5.5) and Z is the output of the model (5.4) with the input F .

As before, the PDE constrained optimization problem was solved by Automatic Differentiation approach (Section 1.3). The direct problem (5.4) was discretized in space and in time. The space interval $[-1, 0]$ in Ox direction was divided in

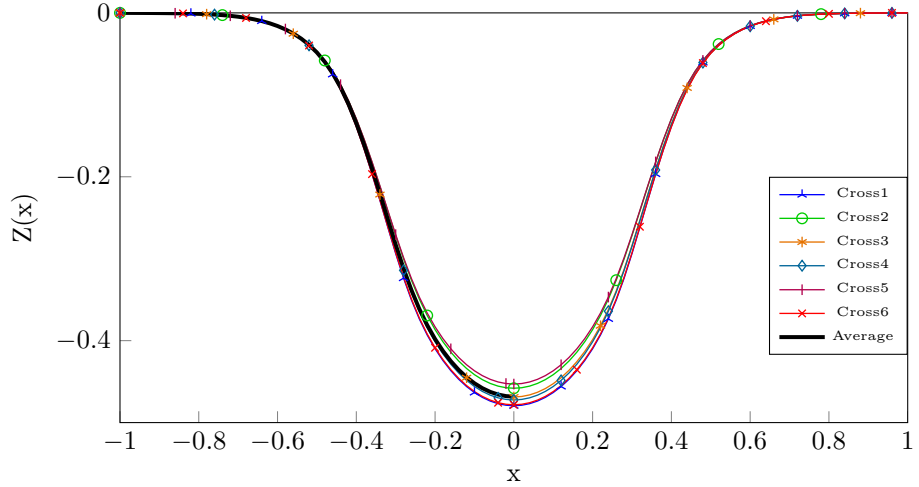


Figure 5.11 – Generation of the Z_{num} . Six cross sections from Figure 5.9 that were used for calculation of the average profile Z_{num} (thick black curve).

M equal sub-intervals of length $dx = \frac{1}{M}$. The space interval $[-1, 4]$ in Ox was discretized with the same step $dy = dx$. The values F_i of F in $M + 1$ space discretization points $\{x_i, i = \overline{1, M+1}\}$ were considered as the calibration parameters of the model. The values of F in other points were obtained as an interpolation of the calibration parameters. The direct problem was solved using Lax-Friedrich scheme ([Osher and Fedkiw, 2006],[Sethian, 1999]). The cost function $J(F)$ was calculated numerically by discrete integration. Then the gradient of the cost function $J(F_1, \dots, F_M)$ was obtained by passing the program evaluating J to TAPE-NADE (Section 1.3). When the value of the cost function and its gradient are available, the minimum in the Problem 4 was found by application of l-BFGS minimizer (Section 1.1).

Figure 5.12 gives an example of the successful calibration of F from the experimental data simulated by direct problem with an arbitrary chosen $F = \tilde{F}$. In this case the experimental data Z_{exp} was calculated following the same procedure (5.5) as calculation of Z_{num} in the cost function (5.6). The achieved accuracy of the calibration $\varepsilon_F = \frac{\|F^* - \tilde{F}\|}{\|F^*\|}$ is of order of fraction of percent: 0.4% for $\alpha = 3 * 10^{-6}$. This brings us back to the question of choice of value of α . It was chosen by L -curve regularization parameter selection method ([Hansen and O’Leary, 1993], [Hansen, 1999]). Figure 5.13 gives the dependence of the accuracy of the calibration $\|Z_{num}^* - Z_{exp}\|$ on the regularization parameter α . Here Z_{num}^* is calculated by (5.5) from the solution of the direct problem (5.4) corresponding to $F = F^*$ solution of the calibration procedure. The graph on 5.13 has a form of a letter

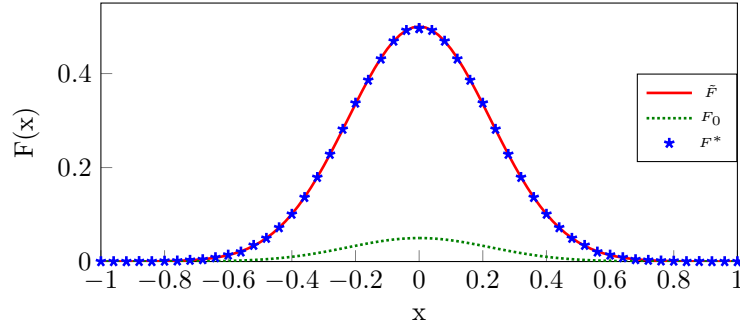


Figure 5.12 – Calibration of the beam profile from the geometry of sputtered trench.

\tilde{F} was used for the simulation of the experimental data.

F_0 corresponds to the first guess in the minimization procedure.

F^* represents the result of calibration.

"L", and α was taken from its corner. Results on the Figures 5.12 correspond to a choice $\alpha = 3 * 10^{-6}$.

Of course the previous result serves mainly for the theoretical validation of the calibration procedure. It is impossible to obtain the experimental data corresponding to the Z_{num} , because the cross section profiles are not available in the strictly predetermined points y^c . A possible solution is to consider the average experimental profile. The drawback of this approach consists in adding the time consuming measurements to the experimental part. Nevertheless we are interested in trenches with the bottom that can be considered constant in Oy direction in practice. This means that there should not be any difference in different cross section profiles Z_{exp} . We run the developed calibration procedure with the experimental data that correspond to the deepest and shallowest cross sections. Figure 5.14 presents the obtained results. As always \tilde{F} corresponds to the real F . F_{sh}^* in Figure 5.14 corresponds to the beam profile calibrated from the shallowest cross section Z_{sh} of the trench (of course, far from the end points). F_d^* corresponds to F calibrated from the deepest cross section Z_d . The curves corresponding to other cross section choices lie between F_{sh}^* and F_d^* , in "Range" on Figure 5.14. In the worst case scenario, the error of calibration $\varepsilon_F = \frac{\|F^* - \tilde{F}\|}{\|F^*\|}$ raises to few percents.

For Figure 5.14, the worst choice of Z_{exp} is Z_{sh} and the corresponding error is $\varepsilon = 2.56\%$. This means that the calibration procedure is able to retrieve the beam profile from the arbitrary chosen cross section with fairly good accuracy.

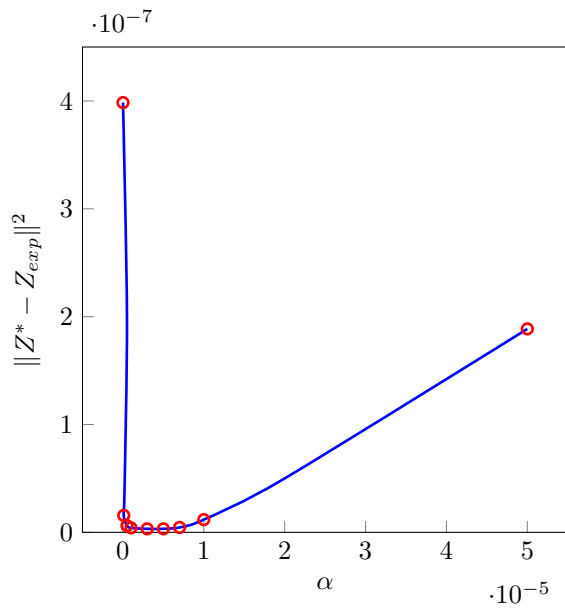


Figure 5.13 – Accuracy of the calibration as a function of the regularization parameter α for trench sputtering.

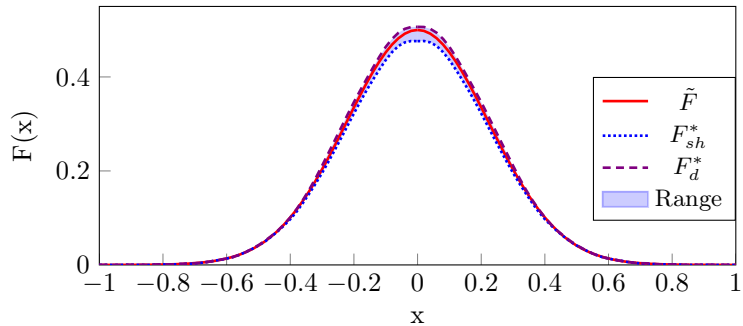


Figure 5.14 – Calibration of F from the single arbitrary chosen cross section.

The considered calibration procedure has to be further modified for the work with real experimental data. As in case of the abrasive waterjet milling of the trench, the calibration of the FIB trench sputtering is highly altered by the secondary effects. This problem is a subject of the prospective study.

Chapter 6

Laser ablation

During the laser ablation material is removed from the solid surface by irradiating it with a laser beam ([Dahotre and Harimkar, 2008]). Depending on the characteristics of experiment, the material can be heated by the absorbed laser and eventually melted or evaporated, and it can also be converted to a plasma. We suggested a fast in terms of experimental application criterion to distinguish between thermal and non-thermal regimes of laser ablation. This chapter presents the results obtained in collaboration with Stefano Buratin and Ming Chu Kong from the Advanced Manufacturing Technology Center of University of Birmingham.

6.1 Introduction

One of the most common uses of laser ablation in the last years is the semiconductor micromachining ([Bärsch et al., 2003], [Zolper et al., 1989]). Using laser machining, several processes such as welding, cutting and scribing can be thus performed in a contactless manner, with minimal damage to the workpiece. To optimize laser machining in terms of accuracy, time consumption, and effectiveness, various physical and analytical models have been developed in an attempt to either predict the ablation results, or explain the laser-work piece interaction ([Bogaerts et al., 2003],[Kong et al., 2012b],[Samant and Dahotre, 2010]). From these models the role of the laser pulse duration results fundamental on the material removal mechanism, and together with the fluence, it leads to either thermal or non-thermal phenomena ([Bonse et al., 2002]).

The experimental evaluation of the presence/absence of thermal effects (e.g molten ring around the crater, debris, splashes, heat affected zone), by analysing the processed samples, cannot be usually obtained by using the optical microscope (OM) because of the size of the defects that it needs to look for. It requires more

accurate techniques such as the scanning electron microscope (SEM), transmission electron microscope (TEM) or atomic force microscope (AFM) ([Rogers et al., 2009], [Singha et al., 2008]). Although these analysis methods are the traditional and the commonly used way to identify thermal or non-thermal effects on the laser processed samples, they are very time-consuming in particular to measure a high number of samples.

In this Chapter we provide a method, based on the analysis of the crater shape measured by a 3D optical method to decrease the time needed to quantify the thermal effects after a laser irradiation. Taking into account the thermal diffusion model for laser ablation, we identified one function that refers to the crater shape based on the isothermal curves. On the other hand, by neglecting thermal diffusion, we applied an equation based on the iso-energetic curves. We compared the two functions with the experimental craters to identify the closest one to the real data measured. We matched the information obtained with the classical SEM analysis and we verified the reliability of our novel technique on the amount estimation of the thermal effects. This technique does not substitute the classical ones as SEM, TEM or AFM, but it represents a powerful method to quantify the thermal effects involved using fast analysis techniques such as 3D confocal microscopy or white light interferometry and therefore to reduce the analysis time. Indeed, it is interesting to notice how the technique proposed is not based on the characteristics take into account from the traditional method such as the presence of splash or debris, but is based on the crater shape. For this reason our proposed method can also be used together with the classical one to give a complete overview of the impact of thermal effects on the laser ablation process.

6.2 Motivation for the introduction of the criterion

We consider a laser that hits a silicon sample at 90° incident angle. Figure 6.1 represents the choice of the coordinate system. The silicon sample and the air are treated as the semi-infinite media.

The resulting temperature profile inside the silicon is described by the following PDE problem (6.1), ([Watanabe and Iguchi, 1999],[Liu et al., 1997]).

$$\begin{cases} u_t - a^2 \Delta u = f(x, y, z, t); \\ u(x, y, z, t = 0) = 0 \\ u_z(x, y, z = 0, t) = 0. \end{cases} \quad (6.1)$$

Here $0 \leq z \leq +\infty$, $-\infty \leq x, y \leq +\infty$, $0 \leq t \leq +\infty$ and a^2 is a thermal diffusivity. The condition of nulling of the normal derivative on the surface comes from the fact that the thermal conductivity of silicon is considerably higher than the heat transfer coefficient from silicon to air.

In the infinite medium the solution of the heat equation with a point source is given by the heat kernel (6.2).

$$K(\vec{r}, t) = \frac{1}{(4\pi a^2 t)^{3/2}} e^{-\frac{r^2}{4a^2 t}}, \quad (6.2)$$

where $\vec{r} = (x, y, z)$.

We build the fundamental solution for the semi-infinite medium (6.3) in a way that the normal derivative is equal to zero on the boundary.

$$\Phi(\vec{r}, \vec{r}', t, \tau) = \frac{1}{(4\pi a^2(t - \tau))^{3/2}} \left(e^{-\frac{(x-x')^2 + (y-y')^2 + (z-z')^2}{4a^2(t-\tau)}} + e^{-\frac{(x-x')^2 + (y-y')^2 + (z+z')^2}{4a^2(t-\tau)}} \right) \quad (6.3)$$

Then (6.4) gives the solution of (6.1) as a convolution of the fundamental solution with the source term f .

$$u(\vec{r}, t) = \int_0^t \int_{\mathbb{R}^3} \Phi(\vec{r}, \vec{r}', t, \tau) f(\vec{r}', \tau) d\vec{r}' d\tau. \quad (6.4)$$

If we consider laser as a point source at $\vec{r} = (0, 0, \varepsilon)$ infinitely close to the boundary $\varepsilon \rightarrow 0$, $f(x', y', z', \tau) = \delta(x', y', z' - \varepsilon, \tau)$, the solution differs from the heat kernel only by multiplier:

$$u(\vec{r}, t) = \frac{2}{(4\pi a^2 t)^{3/2}} e^{-\frac{r^2}{4a^2 t}}.$$

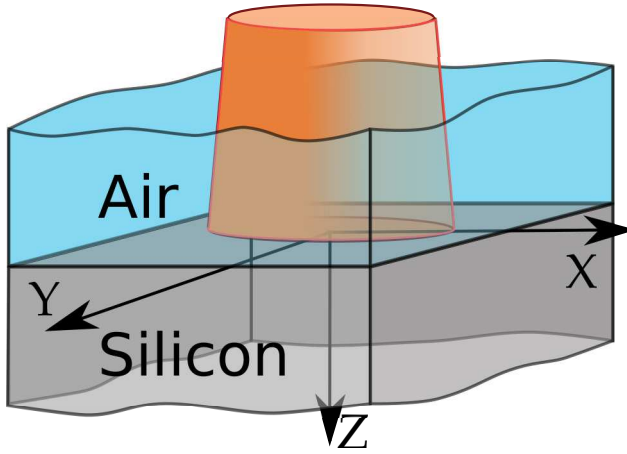


Figure 6.1 – Schematic representation of two semi-infinite media air/silicon.
Laser impacts the sample at normal incidence.

If we take into account the dispersion of the beam, the source term becomes:

$$f(x', y', z', \tau) = \frac{Q}{2\sigma^2} e^{-\frac{x'^2+y'^2}{2\sigma^2}} \delta(z' - \varepsilon) \delta(\tau).$$

Here Q is the beam energy intensity and σ^2 defines the beam waist. After the integration of (6.4) and taking the limit $\varepsilon \rightarrow 0$, the temperature distribution inside the silicon is given by (6.5).

$$u(\vec{r}, t) = \frac{Q}{\sigma^2 + 2a^2t} e^{-\frac{x^2+y^2}{2\sigma^2+4a^2t}} \frac{1}{\sqrt{4\pi a^2 t}} e^{-\frac{z^2}{4a^2t}}. \quad (6.5)$$

It follows from (6.5) that the isothermal surfaces are given by the ellipsoids.

The following modification of the source term (6.6) is motivated by the Lambert-Beer law and takes into account the electromagnetic penetration of the beam.

$$f(\vec{r}', \tau) = \frac{Q}{2\pi\sigma^2} e^{-\frac{x'^2+y'^2}{2\sigma^2}} k e^{-kz'} \delta(\tau). \quad (6.6)$$

In (6.6) k is the inverse of the electromagnetic penetration depth.

The corresponding to (6.6) temperature distribution is given by (6.7).

$$u(\vec{r}, t) = \frac{Q}{2\sigma^2 + 4a^2t} e^{k^2 a^2 t} \frac{k}{2} e^{-\frac{x^2+y^2}{2\sigma^2+4a^2t}} \left(e^{-kz} \operatorname{erfc}\left(ka\sqrt{t} - \frac{z}{2a\sqrt{t}}\right) + e^{kz} \operatorname{erfc}\left(ka\sqrt{t} + \frac{z}{2a\sqrt{t}}\right) \right). \quad (6.7)$$

The shape of the isothermal surfaces cannot be deduced straightforward from (6.7). But the additional simplification can be done for the big values of the argument

Parameter	Value
$a^2 [cm^2/s]$	0.88
$k [\mu m^{-1}]$	1 (for high temperatures)
$z [\mu m]$	< 7 (depth of the crater measured in the experiment)

Table 6.1 – Silicon constants.

of the complementary error function erfc . Namely, the following asymptotic expansion takes place:

$$\text{erfc}(x) \approx \frac{e^{-x^2}}{x\sqrt{\pi}}, \text{ when } x \rightarrow +\infty. \quad (6.8)$$

If the argument of erfc is big in (6.7), this solution can be approximated by (6.9).

$$u(\vec{r}, t) = \frac{Q}{\sigma^2 + 2a^2t} \frac{1}{\sqrt{4\pi a^2t}} e^{-\frac{x^2+y^2}{2\sigma^2+4a^2t}} e^{-\frac{z^2}{4a^2t}} \quad (6.9)$$

We justified the use of the approximation (6.8) for the 220ns pulse impact. Table 6.1 gives the characteristic constants in the experiment.

In (6.7) we consider only times bigger than pulse duration $t > 220\text{ns}$. Approximation (6.8) can be applied to $\text{erfc}\left(ka\sqrt{t} - \frac{z}{2a\sqrt{t}}\right)$, and thus automatically to $\text{erfc}\left(ka\sqrt{t} + \frac{z}{2a\sqrt{t}}\right)$, with the error of approximation less than 4%.

The isothermal surfaces of the distribution (6.9) are ellipsoids:

$$\frac{x^2}{A} + \frac{y^2}{A} + \frac{z^2}{C} = 1, \quad (6.10)$$

where A and C are constants.

We are interested in the critical temperature corresponding to the boiling point of the silicon. In the case when the ablation is driven mainly by the thermal effects, the isothermal surface of this temperature should describe the crater created in the silicon.

In the same time, for the source in form (6.6) the surfaces of the same energy are defined by paraboloids (6.11).

$$\frac{x^2}{A_1} + \frac{y^2}{A_1} + \frac{z}{C_1} = 1, \quad (6.11)$$

where A_1 and C_1 are constants. If the final geometry of the silicon sample depends only on the energy beam distribution transmitted inside the sample, the ablated crater should be described by paraboloid.

Of course, such a consideration of the interaction of the laser with the material is extremely simplified; and (6.7), (6.9) cannot pretend to correspond to the temperature distribution in the real-world experiment. Moreover, the expansion (6.8) is not valid for an arbitrary choice of the beam characteristics. Nevertheless, the comparison between the elliptic and the hyperbolic best fitting can reveal the role of the thermal effects in the crater formation.

6.3 Experimental study of the ablated crater

Based on (6.10) and (6.11), the best ellipsoid and paraboloid fittings were found for the experimental crater. To characterize the precision of each fitting, we calculate the residual sums of squares R_e and R_p between the real crater profile and the ellipsoid and paraboloid fittings correspondingly. Then we introduce a percentage difference D in (6.12) as factor that identifies the impact of the thermal effect on the crater shape.

$$D = \frac{R_e - R_p}{\min(R_e, R_p)} * 100\%. \quad (6.12)$$

When the thermal effects play an important role in the crater formation $R_e < R_p$ and D is negative. When ablation is mainly non-thermal, $R_e > R_p$ and D is positive.

Figure 6.2 shows the percentage difference D for the experimental craters for the pulse duration from the femtoseconds to the microseconds. Based on the experimental SEM images, a threshold of $D^* = 10\%$ was introduced to distinguish between the thermal and non-thermal regimes of ablation. If $D > D^*$, the ablation is non-thermal, and the corresponding craters in the SEM pictures do not have any splashes, debris or surface modification that could indicate a presence of a thermal process. When $D < -D^*$, the thermal effects play a role in the crater formation. The corresponding SEM pictures confirm that for the experiments with such values of D the thermal effects manifest themselves in form of a large amount of splashed material around the crater.

Thereby the introduced criterion indeed allows to distinguish between the different regimes of ablation when $|D| > D^*$. This method does not require to resort to the accurate SEM measurements technique, thus allowing to analyze the processed samples by much faster optical microscope measurements.

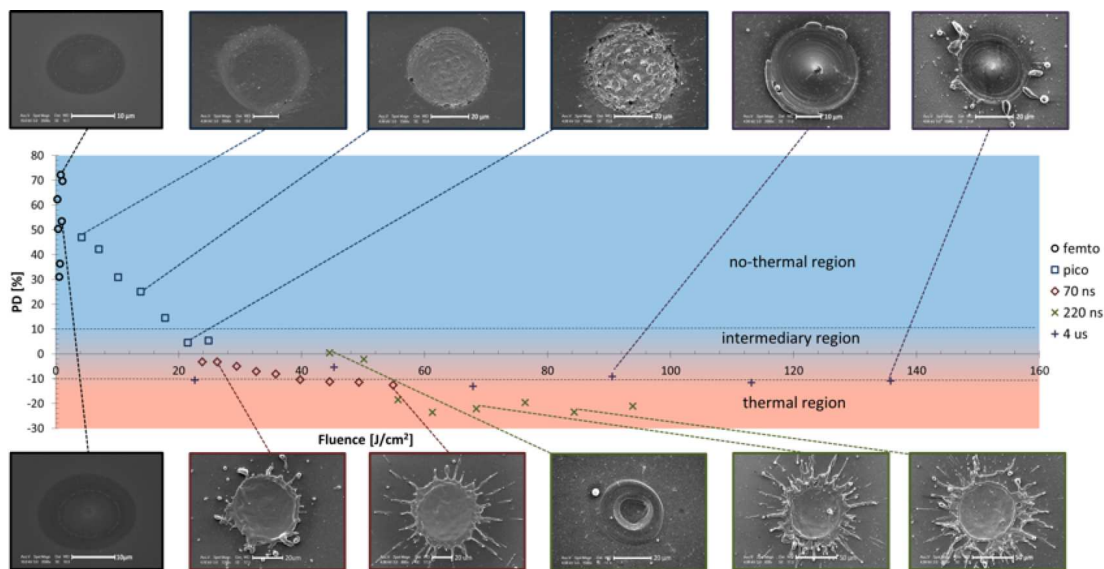


Figure 6.2 – The percentage difference for 5 different pulse duration.
The dotted lines separate 3 regions: non-thermal ($PD > 10\%$), intermediary ($-10\% < PD < 10\%$) and thermal ($PD < -10\%$).
Around the chart the SEM images have been added and connected to the related values of PD.

Conclusions and Perspectives (English)

In this thesis we developed a general approach to the calibration of the empirical models of material treatment by the energy beam. The evolution of the material surface under the energy beam impact is modeled by PDE equation. This equation contains a set of the unknown coefficients - the calibration parameters of the model. Unknown parameters can be calibrated by minimization of the cost function, i.e., function, which describes difference between experiment and the result of the modeling. As the modeled surface is a solution of the PDE, this leads to the PDE-constrained optimization problem. We used the adjoint approach and the automatic differentiation approach to the minimization of the cost function.

We developed a calibration procedure for the geometrical model of the abrasive waterjet footprint (Chapters 2-4). The general framework of this procedure is presented in Figure 6.3. Chapter 3 illustrated the application of the adjoint approach to PDE constrained optimization for a crater milling problem. The developed approach allowed to calibrate the numerically generated experimental data with high precision. The waterjet of a short duration and with stable characteristics is hard to obtain in practice, so the reliable experimental data for the calibration are not available. A more interesting from the experimental point of view case of a trench milling was considered in Chapter 4. The developed calibration routine enabled a simultaneous calibration of all model parameters without any simplifications of the model. The proposed cost function allowed to avoid a non-uniqueness of the numerical solution by taking into account results of two experiments corresponding to different feed-speed of the jet. The reliability of the calibration was at first validated on the numerically simulated footprints. Further, an example of the calibration of the real experimental data was presented for trenches milled on Ti-6Al-4V material. Additional modification of the cost function shielded the calibration procedure from the influence of the secondary effects of piling up of the material on the trench edges, which are not included in the geometrical model. Used for calibration experimental trenches corresponded to the speed of the jet $v = 3000\text{mm/min}$ and $w = 1000\text{mm/min}$. The obtained calibrated values of the

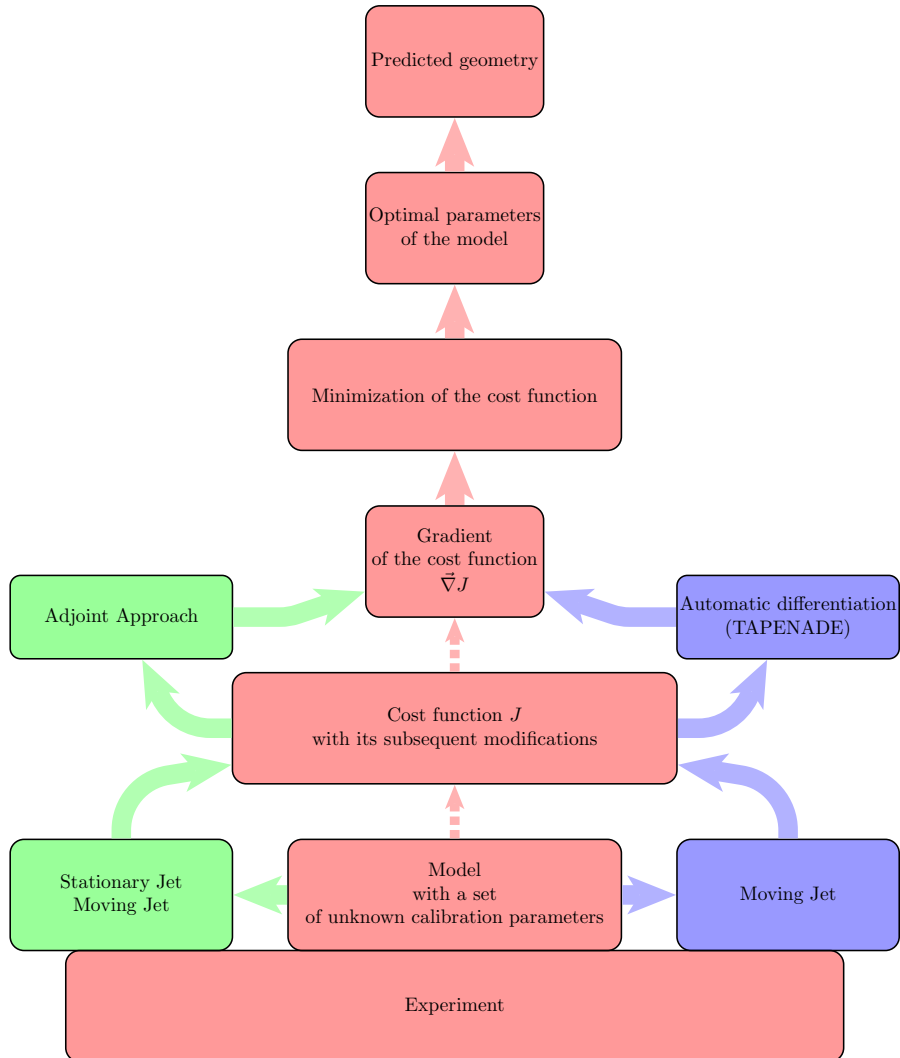


Figure 6.3 – General framework of the calibration procedure of the geometrical model of the abrasive waterjet milling.

parameters describe the calibrated experimental data with high accuracy (1.46% for $v = 1000\text{mm}/\text{min}$ and 4.15% for $v = 3000\text{mm}/\text{min}$). The result of the calibration of these two trenches also allows to predict the shape of the trenches that correspond to different feed speed (with accuracy 1.48% for $v = 1500\text{mm}/\text{min}$, 7.33% for $v = 2500\text{mm}/\text{min}$). For the considered material the further improvement of the accuracy requires the modification of the model of the milling process. This modification is a subject of the prospective research.

In Chapter 5 we developed the procedure for the calibration of the beam profile distribution for the Focused Ion Beam milling. We considered the beam footprint in form of a crater (Section 5.2) and a trench (Section 5.3). The calibration was validated for the numerically generated experimental data. There are two possible developments that start from this point. In the simple case, in order to calibrate the real experimental data, the problem requires the modification in the spirit of trench milling by AWJ (Chapter 4). However, it is possible that FIB model calibration is more complicated and requires the inclusion of the secondary effects into the model even for the beam profile calibration.

At last, in Chapter 6, we presented a simple criterion that allows to distinguish between the thermal and non-thermal laser ablation regimes.

Conclusions et Perspectives (Français)

Dans cette thèse nous développons une approche générale pour la calibration de modèle empirique de traitement de matériaux par les faisceaux de haute énergie. L'évolution de la surface du matériau sous l'action du faisceau de haute énergie est modélisée par une EDP. Cette équation contient un ensemble de coefficients inconnus - les paramètres du modèle. Les paramètres inconnus peuvent être calibrés par minimisation de la fonction coût, c'est-à-dire, la fonction qui décrit la différence entre l'expérience et le résultat de la modélisation. Comme la surface modélisée est une solution d'une EDP, cela rentre dans le cadre de l'optimisation sous contrainte d'EDP. Nous avons utilisé l'approche adjointe et l'approche par différenciation automatique pour minimiser la fonction coût.

Nous avons développé un procédé de calibration de modèle géométrique de traitement de matériaux par le jet d'eau abrasif (Chapitre 2-4). Le cadre général de ce procédé est illustré par la figure 6.4.

Le chapitre 3 est dédié à l'application de l'approche adjointe pour le problème relié à la fabrication d'un cratère. Le procédé que nous avons développé a permis de calibrer les données synthétiques avec une grande précision. Le jet d'eau abrasif de courte durée avec des caractéristiques stables est difficile à obtenir en pratique. C'est pourquoi les données expérimentales fiables ne sont pas disponibles. Dans le chapitre 4 nous avons étudié la fabrication d'une rainure. Ce cas est plus intéressant d'un point de vue expérimental. Nous avons développé un procédé de calibration permettant d'identifier tous les paramètres de modèle sans aucune simplification additionnelle du modèle. Nous avons modifié la fonction coût afin de contourner le problème de non-unicité de la solution du problème de calibration. La fonction coût modifiée se base sur les résultats de deux expériences avec les vitesses transversales du jet différentes. La fiabilité de la calibration a été validée pour les données synthétiques. Ensuite, nous avons donné un exemple de calibration des données expérimentales correspondant aux rainures fabriquées sur la surface de matériau Ti-6Al-4V. Une modification additionnelle de la fonction coût a protégé le procédé de calibration des effets secondaires. Ces effets entraînent l'accumula-

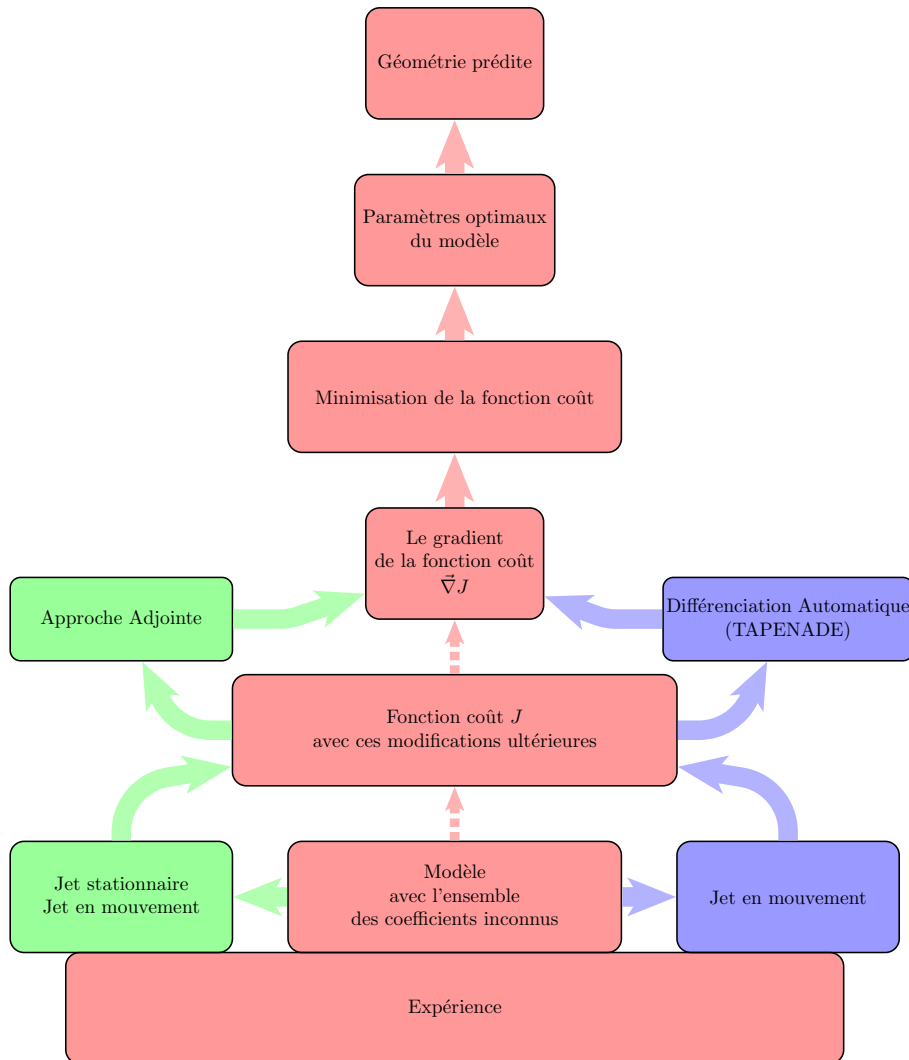


FIGURE 6.4 – Le cadre général du procédé de calibration du modèle géométrique de traitement de matériaux par le jet d'eau abrasif.

tion de matériau sur les bords de la rainure et ils ne sont pas inclus dans le modèle géométrique. Nous avons calibré les données expérimentales correspondant à la vitesse transversale du jet $v = 3000\text{mm/min}$ et $w = 1000\text{mm/min}$. Nous avons obtenu les valeurs des paramètres qui décrivent les données expérimentales avec haute précision (1.46% pour $v = 1000\text{mm/min}$ et 4.15% pour $v = 3000\text{mm/min}$). Le résultat de calibration permet de prédire la forme des rainures correspondant aux vitesses du jet différentes (avec précision 1.48% pour $v = 1500\text{mm/min}$, 7.33% pour $v = 2500\text{mm/min}$). Pour le matériau considéré l'amélioration ultérieure de la précision nécessite des modifications du modèle. Ces modifications sont le sujet de recherche future.

Dans le chapitre 5 nous avons développé le procédé de calibration de modèle d'usinage de matériaux par une sonde ionique focalisée. Nous avons pris les empreintes du faisceau en forme de cratère (Section 5.2) et de rainure (Section 5.3). Le résultat de calibration a été validé pour les données synthétiques. Deux possibilités de développement sont possibles. Dans le cas simple, la calibration avec les données expérimentales nécessite des modifications dans l'esprit du chapitre 4. Il est toutefois possible que la calibration de modèle soit plus compliquée et nécessite l'inclusion des effets secondaires dans le modèle même pour l'identification du profil du faisceau.

Dans le chapitre 6 nous avons proposé un critère pour distinguer facilement entre le régime thermique et non-thermique d'ablation par laser.

Développement (Français)

Nous considérons une surface traitée par le faisceau de haute énergie. Cette surface est décrite par une fonction $Z(\vec{r}, t)$. Nous supposons que l'évolution de la surface du matériau sous l'action du faisceau de haute énergie est modélisée par une EDP :

$$F(u, Z) = 0. \quad (1)$$

Cette équation (1) contient l'ensemble des coefficients inconnus $\{u\}$ - les paramètres de calibration de modèle. Ils peuvent être des scalaires ou des fonctions. Il n'est pas possible de mesurer ces paramètres directement de l'expérience ou ils sont très difficiles et coûteux à mesurer. Quand les paramètres $\{u\}$ sont connus, on peut prédire le résultat de l'expérience donnée en résolvant (1). (1) s'appelle le problème direct. Le problème inverse consiste à trouver $\{u\}$ à partir de la géométrie de la surface cible $Z(\vec{r}, T)$ au moment final du traitement $t = T$. Les valeurs de paramètres $\{u\}$ déterminent la solution du problème direct. L'idée consiste à comparer ce résultat $Z(\vec{r}, T)$ avec la surface Z_{exp} mesurée expérimentalement - une empreinte de faisceau. Nous introduisons la fonction coût J de la manière suivante :

$$J(u) = \|Z(\vec{r}, T) - Z_{exp}\|^2. \quad (2)$$

Cette fonction décrit la différence entre les données expérimentales et la solution du problème direct avec le choix donné de paramètres $\{u\}$. Le problème inverse consiste à trouver $\{u^*\}$ minimisant la fonction coût, c'est-à-dire résoudre le problème d'optimisation sous contrainte d'EDP suivant :

Problème. Trouver l'ensemble des paramètres $\{u^*\}$ tel que

$$J(u^*) = \inf_u J(u),$$

sous la contrainte que Z soit la solution du modèle direct (1) avec le choix de paramètres $\{u\}$.

Il est nécessaire d'ajouter un terme de régularisation de Tikhonov ([Tikhonov and Arsenin, 1977]) dans la fonction coût (2), quand ce problème d'optimisation est mal posé. De plus, (2) donne la forme la plus simple de la fonction

coût, et cette expression doit être modifiée dans certains cas (voir Chapitre 4, Section 5.3). Le défi principal de ce problème d'optimisation vient du fait que certains paramètres sont des fonctions. Cela conduit à l'optimisation dans un espace de dimension infinie.

Jet d'eau abrasif.

Pour créer un jet d'eau abrasif l'eau est poussée par une pompe à haute pression sous un petit orifice. Des particules abrasives sont ajoutées à l'eau avant la sortie. L'impact du jet créé de cette façon sur la surface du matériau entraîne l'érosion du matériau. Nous étudions l'évolution de la surface initialement plane sous l'action du jet incident sous un angle 90°. La figure 1 représente schématiquement une coupe verticale de la surface traitée.

Selon le modèle géométrique, l'évolution de la profondeur $Z(x, y)$ est décrite par le système suivant :

$$\begin{cases} \frac{\partial Z}{\partial t} = -E(r) \exp(aZ) \cos^{\frac{k}{2}} \theta, \\ Z(x, y, 0) = 0, \end{cases} \quad (3)$$

où r est la distance au centre du jet, θ est l'angle local d'impact (Figure 1). Ce modèle contient l'ensemble des paramètres inconnus : E - la fonction de la vitesse de gravure (le terme anglais *etching rate*) ; a - le paramètre scalaire qui prend en considération que l'érosion dépend de la distance entre le jet et la surface cible ; k - le paramètre scalaire qui vient de la loi du cosinus pour l'érosion de matériaux fragiles.

Le cas de jet d'eau abrasif stationnaire.

Quand le jet est stationnaire, la géométrie étudiée représente un cratère. L'évolution du profil de ce cratère est décrite par (4).

$$\begin{cases} \frac{\partial Z}{\partial t} = -\frac{E(|x|) \exp aZ}{\left(1 + \left(\frac{\partial Z}{\partial x}\right)^2\right)^{\frac{k}{2}}}, \\ Z(x, 0) = 0. \end{cases} \quad (4)$$

Nous nous sommes intéressés à la calibration de la fonction E . Dans les termes d'approche développée cela mène à la résolution du problème suivant :

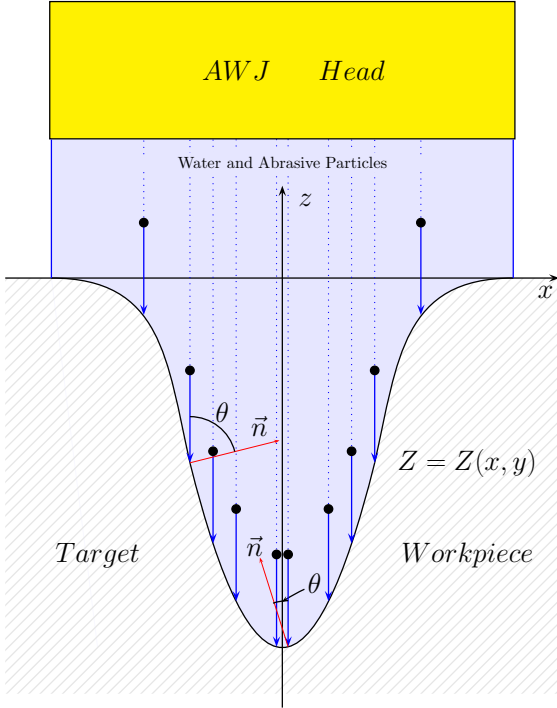


FIGURE 1 – Représentation schématique d'une coupe verticale de l'empreinte du jet d'eau abrasif.

Problème. Trouver la fonction positive E^* telle que

$$J(E^*) = \inf_E J(E), \quad (5)$$

sous la contrainte que Z soit la solution du modèle direct (4) avec le choix de paramètre E .

Nous avons résolu ce problème d'optimisation en appliquant l'approche variationnelle. Nous avons introduit le Lagrangien du problème :

$$L(E, Z, P) = J(E) + \int_0^T \int_{-1}^1 P(x, t) \left(\frac{\partial Z}{\partial t} - G(Z, Z_x, E) \right) dx dt, \quad (6)$$

où P est le multiplicateur de Lagrange associé à la contrainte que Z soit la solution de (4). G est une fonction qui décrit le côté droit de l'EDP (4), c'est-à-dire $G(Z, Z_x, E) = -E(x) \exp(aZ) / (1 + (Z_x)^2)^{\frac{k}{2}}$. Le minimum de la fonction coût J correspond au point-selle du Lagrangien L . La variation du Lagrangien par rapport à Z permet d'obtenir le problème adjoint pour trouver l'état adjoint P . Nous avons obtenu le problème adjoint en formulation continue et discrétisée. Quand P est connu le gradient de J est calculé en utilisant (7).

$$\frac{\partial J}{\partial E(x)} = \frac{\partial L}{\partial E(x)} = - \int_0^T P(x, t) \frac{\partial G}{\partial E}(x, t) dt - \alpha \nabla^2 E(x), \quad (7)$$

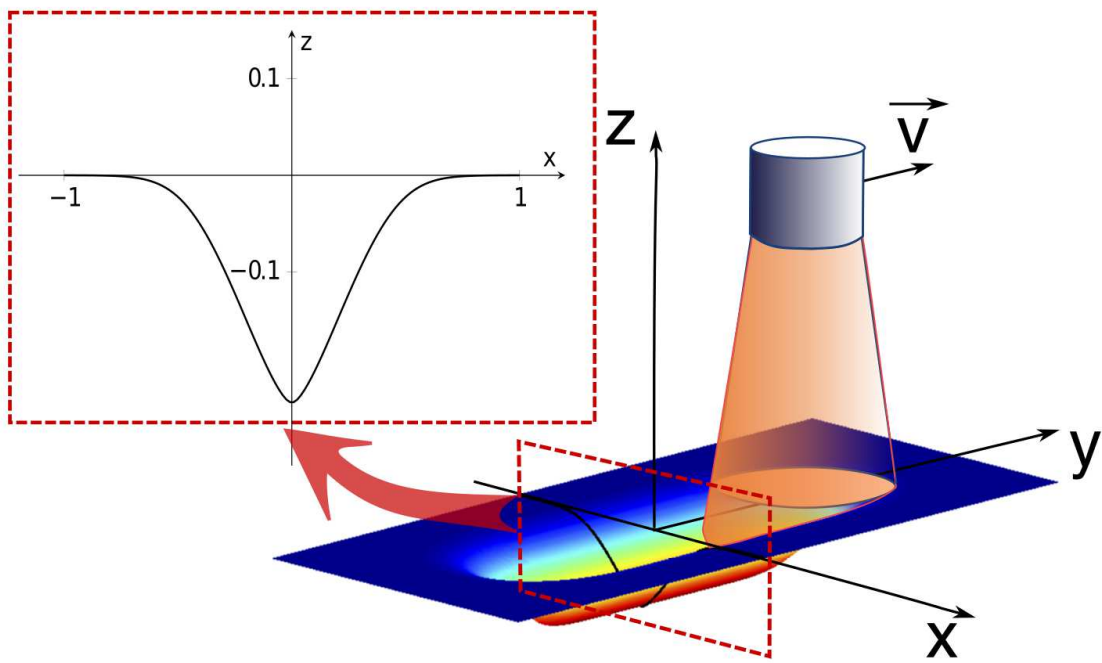


FIGURE 2 – Représentation schématique de fabrication d'une rainure par le jet d'eau abrasif.

où α est le paramètre de régularisation. Puis nous avons utilisé un minimiseur de type quasi-Newton L-BFGS pour réaliser la minimisation et obtenir une estimation de la fonction E optimale. Ce procédé de calibration a été validé pour les données synthétiques.

Le cas de jet d'eau abrasif en mouvement rectiligne uniforme.

Le jet d'eau abrasif de courte durée avec des caractéristiques stables est difficile à obtenir en pratique. C'est pourquoi les données expérimentales fiables ne sont pas disponibles. Nous avons étudié la fabrication d'une rainure. En pratique, la manipulation consiste à faire bouger le jet allumé le long d'une ligne droite. Cela permet d'éviter les régimes instables lors de la mise en marche et de l'arrêt du jet. La figure 2 représente schématiquement une telle installation expérimentale et précise le choix d'un système de coordonnées. Les données expérimentales représentent le profil de la coupe de rainure par le plan parallèle à ZX après le passage du jet. Le problème direct qui décrit l'évolution de ce profil $Z(x, t)$ est donné par

(8).

$$\begin{cases} \frac{\partial Z}{\partial t} = \begin{cases} -\frac{E(\sqrt{x^2 + t^2}) \exp(aZ)}{\left(1 + \left(\frac{\partial Z}{\partial x}\right)^2 + \left(\frac{\partial Z}{\partial t}\right)^2\right)^{\frac{k}{2}}}, & \text{quand } -\sqrt{1-x^2} \leq t \leq \sqrt{1-x^2}; \\ 0, & \text{quand } -1 \leq t \leq -\sqrt{1-x^2} \text{ et } \sqrt{1-x^2} \leq t \leq 1; \end{cases} \\ Z(x, 0) = 0. \end{cases} \quad (8)$$

La fonction coût devient (9) pour ce cas.

$$J(u) = \frac{1}{2} \int_{-1}^1 (Z(x, t=1) - Z_{exp}(x))^2 dx + \frac{\alpha}{2} \int_{-1}^1 |\nabla E(x)|^2 dx \quad (9)$$

Ici, la deuxième intégrale correspond à la régularisation.

La minimisation de la différence entre les données expérimentales et le résultat de modélisation mène au problème suivant :

Problème. Trouver l'ensemble des paramètres $u^* = \{E^*, k^*, a^*\}$ tel que

$$J(u^*) = \inf_u J(u), \quad (10)$$

sous la contrainte que Z soit la solution du modèle direct (8) avec le choix de paramètres u et que E^* soit une fonction positive.

Nous avons résolu ce problème d'optimisation en utilisant les deux méthodes : l'approche adjointe et la différenciation automatique. La fonction coût a été modifiée (11) afin de contourner le problème de non-unicité de la solution du problème de calibration.

$$\begin{aligned} J(E, k, a) = & \frac{1}{2} \int_{-1}^1 (Z^v(x, t=1) - Z_{exp}^v(x))^2 dx + \\ & + \frac{1}{2} \int_{-1}^1 (Z^w(x, t=1) - Z_{exp}^w(x))^2 dx + \frac{\alpha}{2} \int_{-1}^1 |\nabla E(x)|^2 dx, \end{aligned} \quad (11)$$

La fonction coût modifiée (11) se base sur les résultats de deux expériences avec les vitesses transversales du jet différentes, v et w . La fiabilité de la calibration a été validée pour les données synthétiques.

Ensuite, nous avons donné un exemple de calibration des données expérimentales correspondant aux rainures fabriquées sur la surface de matériau Ti-6Al-4V. À cause de la plasticité du matériau les rainures expérimentales présentent l'accumulation de matériau sur les bords. Ces effets ne sont pas inclus dans le modèle

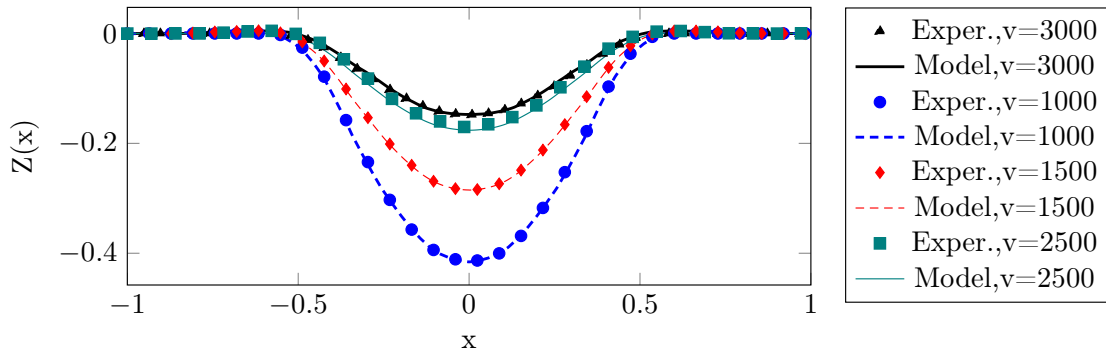


FIGURE 3 – Rainures expérimentales et le résultat de la modélisation pour les vitesses différentes du jet. Les données correspondantes aux vitesses $v = 3000 \text{mm}/\text{min}$ et $w = 1000 \text{mm}/\text{min}$ ont été utilisées pour la calibration du modèle.

géométrique. Une modification additionnelle de la fonction coût a protégé le procédé de calibration des effets secondaires, (12).

$$\begin{aligned} J(E, k, a) = & \frac{1}{2} \int_{-1}^1 W(x) (Z^v(x, t=1) - Z_{exp}^v(x))^2 dx + \\ & + \frac{1}{2} \int_{-1}^1 W(x) (Z^w(x, t=1) - Z_{exp}^w(x))^2 dx + \frac{\alpha}{2} \int_{-1}^1 |\nabla E(x)|^2 dx, \end{aligned} \quad (12)$$

où la fonction W dans les intégrales est une fonction poids.

Nous avons calibré les données expérimentales correspondant à la vitesse transversale du jet $v = 3000 \text{mm}/\text{min}$ et $w = 1000 \text{mm}/\text{min}$. Nous avons obtenu les valeurs des paramètres qui décrivent les données expérimentales avec haute précision (1.46% pour $v = 1000 \text{mm}/\text{min}$ et 4.15% pour $v = 3000 \text{mm}/\text{min}$). Le résultat de calibration permet de prédire la forme des rainures correspondant aux vitesses du jet différentes (avec précision 1.48% pour $v = 1500 \text{mm}/\text{min}$, 7.33% pour $v = 2500 \text{mm}/\text{min}$), comme le montre la figure 3.

Sonde ionique focalisée

Les ions accélérés à une haute énergie sont focalisés sur un point de taille de l'ordre du micromètre. L'énergie ionique est suffisante pour arracher des atomes du matériau cible. Nous étudions l'évolution de la surface initialement plane sous l'action de la sonde ionique focalisée incidente sous un angle 90°. La figure 4 représente schématiquement une coupe verticale de la surface traitée.

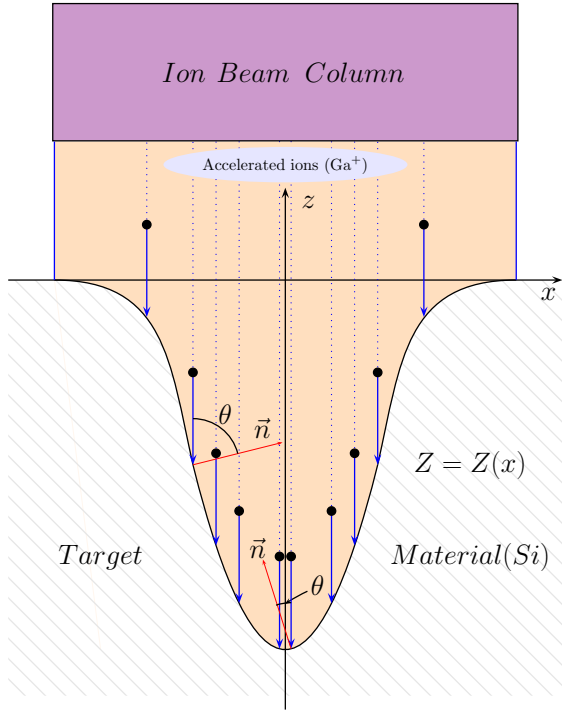


FIGURE 4 – Représentation schématique d'une coupe verticale de l'empreinte de la sonde ionique focalisée.

L'évolution de la profondeur $Z(x, y)$ est décrite par l'équation suivante :

$$\frac{\partial Z}{\partial t} = -F(r)Y(\theta) \cos \theta. \quad (13)$$

Ici Y est une fonction connue d'expérience, θ est l'angle local d'impact dans le point $(x, y, Z(x, y))$ (Figure 4), r est la distance au centre du faisceau. F est le profil du faisceau, le paramètre de calibration du modèle.

De façon similaire à l'étude de jet d'eau abrasif, nous avons développé le procédé d'identification du profil du faisceau en utilisant la différentiation automatique. Les empreintes du faisceau en forme de cratère (Section 5.2) et de rainure (Section 5.3) ont été étudiées. Le résultat de calibration a été validé pour les données synthétiques.

Bibliography

- [Ali and Hung, 2001] Ali, M. Y. and Hung, N. (2001). Surface roughness of sputtered silicon. ii. model verification. *Materials and Manufacturing Processes*, 16(3):315–329.
- [Ali et al., 2010] Ali, M. Y., Hung, W., and Yongqi, F. (2010). A review of focused ion beam sputtering. *International journal of precision engineering and manufacturing*, 11(1):157–170.
- [Andersen and Bay, 1981] Andersen, H. H. and Bay, H. L. (1981). Sputtering yield measurements. In *Sputtering by particle bombardment I*, pages 145–218. Springer.
- [Andrew and Gao, 2007] Andrew, G. and Gao, J. (2007). Scalable training of l 1-regularized log-linear models. In *Proceedings of the 24th international conference on Machine learning*, pages 33–40. ACM.
- [Antia, 2002] Antia, H. (2002). *Numerical methods for scientists and engineers*, volume 1. Springer Science & Business Media.
- [Auroux, 2003] Auroux, D. (2003). *Étude de quelques méthodes d'assimilation de données pour l'environnement*. PhD thesis, Université de Nice Sophia-Antipolis.
- [Auroux and Blum, 2002] Auroux, D. and Blum, J. (2002). A dual data assimilation method for a layered quasi-geostrophic ocean model. *Rev. R. Acad. Cien. Serie A Mat.*, 96(3):316–320.
- [Axinte et al., 2010] Axinte, D., Srinivasu, D., Billingham, J., and Cooper, M. (2010). Geometrical modelling of abrasive waterjet footprints: A study for 90° jet impact angle. *CIRP Annals-Manufacturing Technology*, 59(1):341–346.
- [Balz and Heiniger, 2011] Balz, R. and Heiniger, K. (2011). Determination of spatial velocity distributions of abrasive particles in abrasive water jets using laser-induced fluorescence under real conditions. In *Proceedings of 16th WJTA-IMCA Conference and Expo*.

- [Balz et al., 2013] Balz, R., Mokso, R., Narayanan, C., Weiss, D., and Heiniger, K. (2013). Ultra-fast x-ray particle velocimetry measurements within an abrasive water jet. *Experiments in fluids*, 54(3):1–13.
- [Bärsch et al., 2003] Bärsch, N., Körber, K., Ostendorf, A., and Tönshoff, K. (2003). Ablation and cutting of planar silicon devices using femtosecond laser pulses. *Applied Physics A*, 77(2):237–242.
- [Billingham et al., 2013] Billingham, J., Miron, C., Axinte, D., and Kong, M. (2013). Mathematical modelling of abrasive waterjet footprints for arbitrarily moving jets: part ii?overlapped single and multiple straight paths. *International Journal of Machine Tools and Manufacture*, 68:30–39.
- [Bogaerts et al., 2003] Bogaerts, A., Chen, Z., Gijbels, R., and Vertes, A. (2003). Laser ablation for analytical sampling: what can we learn from modeling? *Spectrochimica Acta Part B: Atomic Spectroscopy*, 58(11):1867–1893.
- [Bonse et al., 2002] Bonse, J., Baudach, S., Krüger, J., Kautek, W., and Lenzner, M. (2002). Femtosecond laser ablation of silicon-modification thresholds and morphology. *Applied Physics A*, 74(1):19–25.
- [Brandenburg et al., 2009] Brandenburg, C., Lindemann, F., Ulbrich, M., and Ulbrich, S. (2009). A continuous adjoint approach to shape optimization for navier stokes flow. In *Optimal control of coupled systems of partial differential equations*, pages 35–56. Springer.
- [Broyden, 1969] Broyden, C. (1969). A new double-rank minimisation algorithm. preliminary report. In *Notices of the American Mathematical Society*, volume 16, page 670.
- [Byrd et al., 1995] Byrd, R. H., Lu, P., Nocedal, J., and Zhu, C. (1995). A limited memory algorithm for bound constrained optimization. *SIAM Journal on Scientific Computing*, 16(5):1190–1208.
- [Chavent, 1974] Chavent, G. (1974). Identification of functional parameters in partial differential equations. In Goodson, R. E. and Polis, M., editors, *Identification of Parameters in Distributed Systems*, pages 31–48. ASME, New York.
- [Ciarlet et al., 1989] Ciarlet, P. G., Miara, B., and Thomas, J.-M. (1989). *Introduction to numerical linear algebra and optimisation*. Cambridge University Press.
- [Dahotre and Harimkar, 2008] Dahotre, N. B. and Harimkar, S. (2008). *Laser fabrication and machining of materials*. Springer Science & Business Media.

- [Di Lorenzo et al., 2007] Di Lorenzo, E., Moore, A. M., Arango, H. G., Cornuelle, B. D., Miller, A. J., Powell, B., Chua, B. S., and Bennett, A. F. (2007). Weak and strong constraint data assimilation in the inverse regional ocean modeling system (roms): Development and application for a baroclinic coastal upwelling system. *Ocean Modelling*, 16(3):160–187.
- [Dimet and Talagrand, 1986] Dimet, F.-X. L. and Talagrand, O. (1986). Variational algorithms for analysis and assimilation of meteorological observations: theoretical aspects. *Tellus A*, 38(2):97–110.
- [ElTobgy et al., 2005] ElTobgy, M., Ng, E., and Elbestawi, M. (2005). Finite element modeling of erosive wear. *International Journal of Machine Tools and Manufacture*, 45(11):1337–1346.
- [Fletcher and Powell, 1963] Fletcher, R. and Powell, M. J. (1963). A rapidly convergent descent method for minimization. *The Computer Journal*, 6(2):163–168.
- [Gelfand and Fomin, 1963] Gelfand, I. and Fomin, S. (1963). *Calculus of variations. Revised English edition translated and edited by Richard A. Silverman*. Prentice-Hall Inc., Englewood Cliffs, NJ.
- [Ghobeity et al., 2008] Ghobeity, A., Spelt, J., and Papini, M. (2008). Abrasive jet micro-machining of planar areas and transitional slopes. *Journal of Micromechanics and Microengineering*, 18(5):055014.
- [Giannuzzi et al., 2006] Giannuzzi, L. A. et al. (2006). *Introduction to focused ion beams: instrumentation, theory, techniques and practice*. Springer Science & Business Media.
- [Gilbert and Lemaréchal, 1989] Gilbert, J. C. and Lemaréchal, C. (1989). Some numerical experiments with variable-storage quasi-newton algorithms. *Mathematical programming*, 45(1-3):407–435.
- [Giles et al., 2003] Giles, M. B., Duta, M. C., M-uacute, J.-D., ller, and Pierce, N. A. (2003). Algorithm developments for discrete adjoint methods. *AIAA journal*, 41(2):198–205.
- [Giles and Pierce, 2000] Giles, M. B. and Pierce, N. A. (2000). An introduction to the adjoint approach to design. *Flow, turbulence and combustion*, 65(3-4):393–415.
- [Griewank and Walther, 2008] Griewank, A. and Walther, A. (2008). *Evaluating derivatives: principles and techniques of algorithmic differentiation*. SIAM.

- [Hansen, 1999] Hansen, P. C. (1999). *The L-curve and its use in the numerical treatment of inverse problems*. IMM, Department of Mathematical Modelling, Technical University of Denmark.
- [Hansen and O'Leary, 1993] Hansen, P. C. and O'Leary, D. P. (1993). The use of the l-curve in the regularization of discrete ill-posed problems. *SIAM Journal on Scientific Computing*, 14(6):1487–1503.
- [Hascoet and Pascual, 2013] Hascoet, L. and Pascual, V. (2013). The tapenade automatic differentiation tool: principles, model, and specification. *ACM Transactions on Mathematical Software (TOMS)*, 39(3):20.
- [Hinze et al., 2009] Hinze, M., Pinnau, R., Ulbrich, M., and Ulbrich, S. (2009). *Optimization with PDE constraints, volume 23 of Mathematical Modelling: Theory and Applications*. Springer, New York.
- [Katardjiev et al., 1988] Katardjiev, I., Carter, G., and Nobes, M. (1988). Simulation of erosion induced surface evolution in temporally and spatially dependent systems. *Vacuum*, 38(11):999–1004.
- [Kim et al., 2007] Kim, H.-B., Hobler, G., Steiger, A., Lugstein, A., and Bertagnolli, E. (2007). Full three-dimensional simulation of focused ion beam micro/nanofabrication. *Nanotechnology*, 18(24):245303.
- [Knott, 2012] Knott, G. D. (2012). *Interpolating cubic splines*, volume 18. Springer Science & Business Media.
- [Kong et al., 2012a] Kong, M., Anwar, S., Billingham, J., and Axinte, D. (2012a). Mathematical modelling of abrasive waterjet footprints for arbitrarily moving jets: part i?single straight paths. *International Journal of Machine Tools and Manufacture*, 53(1):58–68.
- [Kong et al., 2012b] Kong, M. C., Miron, C. B., Axinte, D. A., Davies, S., and Kell, J. (2012b). On the relationship between the dynamics of the power density and workpiece surface texture in pulsed laser ablation. *CIRP Annals-Manufacturing Technology*, 61(1):203–206.
- [LeVeque, 2002] LeVeque, R. J. (2002). *Finite volume methods for hyperbolic problems*, volume 31. Cambridge university press.
- [Lions, 1971] Lions, J. L. (1971). *Optimal control of systems governed by partial differential equations*, volume 170. Springer Verlag.

- [Liu et al., 1997] Liu, C., Leboeuf, J., Wood, R., Geobegan, D., Donato, J., Chen, K.-R., and Puretzky, A. (1997). Computational modeling of physical processes during laser ablation. *Materials Science and Engineering: B*, 47(1):70–77.
- [Lugstein et al., 2003] Lugstein, A., Basnar, B., Smoliner, J., and Bertagnolli, E. (2003). Fib processing of silicon in the nanoscale regime. *Applied Physics A*, 76(4):545–548.
- [Luong et al., 1998] Luong, B., Blum, J., and Verron, J. (1998). A variational method for the resolution of a data assimilation problem in oceanography. *Inverse problems*, 14(4):979.
- [Mamber and Kovacevic, 2012] Mamber, A. W. and Kovacevic, R. (2012). *Principles of abrasive water jet machining*. Springer Science & Business Media.
- [Morales and Nocedal, 2011] Morales, J. L. and Nocedal, J. (2011). Remark on "algorithm 778: L-bfgs-b: Fortran subroutines for large-scale bound constrained optimization". *ACM Transactions on Mathematical Software (TOMS)*, 38(1):7.
- [Nadarajah and Jameson, 2001] Nadarajah, S. and Jameson, A. (2001). Studies of the continuous and discrete adjoint approaches to viscous automatic aerodynamic shape optimization. *AIAA paper*, 2530:2001.
- [Nadarajah, 2003] Nadarajah, S. K. (2003). *The discrete adjoint approach to aerodynamic shape optimization*. PhD thesis, stanford university.
- [Nocedal and Wright, 2006] Nocedal, J. and Wright, S. (2006). *Numerical optimization*. Springer Science & Business Media.
- [Oka et al., 2005] Oka, Y. I., Okamura, K., and Yoshida, T. (2005). Practical estimation of erosion damage caused by solid particle impact: Part 1: Effects of impact parameters on a predictive equation. *Wear*, 259(1):95–101.
- [Osher and Fedkiw, 2006] Osher, S. and Fedkiw, R. (2006). *Level set methods and dynamic implicit surfaces*, volume 153. Springer Science & Business Media.
- [Plessix, 2006] Plessix, R.-E. (2006). A review of the adjoint-state method for computing the gradient of a functional with geophysical applications. *Geophysical Journal International*, 167(2):495–503.
- [Rees et al., 2010] Rees, T., Dollar, H. S., and Wathen, A. J. (2010). Optimal solvers for pde-constrained optimization. *SIAM Journal on Scientific Computing*, 32(1):271–298.

- [Reuther et al., 1999] Reuther, J. J., Jameson, A., Alonso, J. J., Rimllnger, M. J., and Saunders, D. (1999). Constrained multipoint aerodynamic shape optimization using an adjoint formulation and parallel computers, part 2. *Journal of aircraft*, 36(1):61–74.
- [Rogers et al., 2009] Rogers, M. S., Grigoropoulos, C. P., Minor, A. M., and Mao, S. S. (2009). Absence of amorphous phase in high power femtosecond laser-ablated silicon. *Applied Physics Letters*, 94(1):011111.
- [Samant and Dahotre, 2010] Samant, A. N. and Dahotre, N. B. (2010). Three-dimensional laser machining of structural ceramics. *Journal of Manufacturing Processes*, 12(1):1–7.
- [Sei et al., 1994] Sei, A., Symes, W. W., et al. (1994). Gradient calculation of the travelttime cost function without ray tracing. In *65th Ann. Internat. Mtg., Soc. Expl. Geophys., Expanded Abstracts*, pages 1351–1354. Citeseer.
- [Sethian, 1999] Sethian, J. A. (1999). *Level set methods and fast marching methods: evolving interfaces in computational geometry, fluid mechanics, computer vision, and materials science*, volume 3. Cambridge university press.
- [Sigmund, 1987] Sigmund, P. (1987). Mechanisms and theory of physical sputtering by particle impact. *Nuclear Instruments and Methods in Physics Research Section B: Beam Interactions with Materials and Atoms*, 27(1):1–20.
- [Singha et al., 2008] Singha, S., Hu, Z., and Gordon, R. J. (2008). Ablation and plasma emission produced by dual femtosecond laser pulses. *Journal of Applied Physics*, 104(11):113520.
- [Slikkerveer et al., 1998] Slikkerveer, P., Bouten, P., In't Veld, F., and Scholten, H. (1998). Erosion and damage by sharp particles. *Wear*, 217(2):237–250.
- [Slikkerveer et al., 1999] Slikkerveer, P. et al. (1999). Model for patterned erosion. *Wear*, 233:377–386.
- [Tikhonov and Arsenin, 1977] Tikhonov, A. N. and Arsenin, V. Y. (1977). Solutions of ill-posed problems.
- [Timilsina and Rack, 2013] Timilsina, R. and Rack, P. D. (2013). Monte carlo simulations of nanoscale focused neon ion beam sputtering. *Nanotechnology*, 24(49):495303.
- [Torrubia et al., 2015] Torrubia, P. L., Axinte, D., and Billingham, J. (2015). Stochastic modelling of abrasive waterjet footprints using finite element analysis. *International Journal of Machine Tools and Manufacture*, 95:39–51.

- [Tromp et al., 2005] Tromp, J., Tape, C., and Liu, Q. (2005). Seismic tomography, adjoint methods, time reversal and banana-doughnut kernels. *Geophysical Journal International*, 160(1):195–216.
- [Volkert and Minor, 2007] Volkert, C. A. and Minor, A. M. (2007). Focused ion beam microscopy and micromachining. *MRS bulletin*, 32(05):389–399.
- [Wang and Wang, 1996] Wang, J. and Wang, Y. (1996). A novel procedure for measuring the absolute current density profile of a focused gallium-ion beam. *Applied physics letters*, 69(18):2764–2766.
- [Watanabe and Iguchi, 1999] Watanabe, K. and Iguchi, T. (1999). Modeling of vaporization processes of resonant laser ablation. *Applied Physics A*, 69(1):S845–S848.
- [Wengert, 1964] Wengert, R. E. (1964). A simple automatic derivative evaluation program. *Communications of the ACM*, 7(8):463–464.
- [Wolfe, 1969] Wolfe, P. (1969). Convergence conditions for ascent methods. *SIAM review*, 11(2):226–235.
- [Yao, 2007] Yao, N. (2007). *Focused ion beam systems: basics and applications*. Cambridge University Press.
- [Zhu et al., 1999] Zhu, M., Nazareth, J. L., and Wolkowicz, H. (1999). The quasi-cauchy relation and diagonal updating. *SIAM Journal on Optimization*, 9(4):1192–1204.
- [Zolper et al., 1989] Zolper, J. C., Narayanan, S., Wenham, S. R., and Green, M. A. (1989). 16.7% efficient, laser textured, buried contact polycrystalline silicon solar cell. *Applied Physics Letters*, 55(22):2363–2365.